TRAPPED HYDROGEN VIBRATIONAL DENSITY OF STATES MEASUREMENT USING IINS $PdH_{0.0011}$ AT 5 K AND 300 K WITH INCIDENT NEUTRON ENERGY OF 250 MEV

BY

TAI-NI YANG

THESIS

Submitted in partial fulfillment of the requirements
for the degree of Master of Science in Nuclear, Plasma, and Radiological Engineering
in the Graduate College of the
University of Illinois at Urbana-Champaign, 2013

Urbana, Illinois

Master's Committee:
Professor Brent J. Heuser, Director of Research
Professor James F. Stubbins

ABSTRACT

Hydrogen trapped at dislocations in Pd was studied with the incoherent inelastic neutron scattering (IINS) at two temperatures over the energy transfer range of 250 meV. The primary objective of this study was to study the vibrational density of states (VDOS) of deformed $PdH_{0.0011}$ at 5 and 300 K over an energy transfer range corresponding to the multi-phonon and second order harmonic regime respectively.

A free recoil neutron subtraction method was developed to identify the proton recoil intensity within the impulse approximation. The mass of recoil particle is 1.10 amu and 1.12 amu while the recoil energy is located at 208 and 206 meV for 5 K and 300 K respectively.

The 5 K VDOS primary peak energy was observed at 61.4 meV, and is attributed to the β phase palladium hydride. The 300 K VDOS first harmonic peak at 68.2 meV corresponds to the α phase palladium hydride.

The comparison of experimental and calculated results indicate the higher energy peak found at 5 K is due to multiphonon events and shows spectral hardening leading to a higher energy; comparing to the 4 K $PdH_{0.63}$ data. The environment of trapped hydrogen in this research is perturbed and results in different peak positions.

The comparison of experimental and calculated results of second harmonic peak at 300 K shows good correlation with the data of $PdH_{0.014}$ at 295 K, in both the

anharmonicity parameters (19 meV) and the peak position. The given value of 137 meV in the published data was not found in the measurement, likely due to a loss of degeneracy and associated broadening.

This free recoil subtraction method was supported by the two dimensional plots of energy transfer versus wave vector transfer (E v.s Q) before and after recoil subtraction. The shift of intensity maps at free recoil region and second peak area confirmed the effectiveness of the recoil subtraction method.

ACKNOWLEDGEMENTS

I would like to express my gratitude to the following people and organizations. This work would not be possible without the help and collaboration of many people.

The first person I would like to thank is my adviser, Dr. Brent Heuser for his guidance, support and assistance along this research. I am always inspired by his cautious attitude approaching science, and his persistence on the right thing when I thought there is nothing could be done. I am always enlightened by his ideas when I get stuck on my research and experiments, and will be always grateful to have an adviser as him who is willing to answer any question he knows the answer of. I am also indebted to Professor James Stubbins for his kindness in providing suggestions to make this work more complete.

Also, I would like to express my gratitude to all my lab mates for helping me worked with the difficulties in my study. Xianchun Han for his wiliness to put aside his task in hand to help me with the problems I have with data processing; Rick Kustra for his generous time in helping me to develop the MATLAB code; Junli Lin for his great support and precious coffee time together; Mohamed ElBakhshwan for his wise suggestions whenever I get stuck and Joe Bernhardt for sharing his experience in thesis writing. I am really grateful to work with you guys.

I would also like to thank Dr. Douglas Abernathy at ORNL, for his great support

and useful suggestions in helping me analyze the experimental data. The staffs at Nuclear Plasma and Radiological Engineering have always been very friendly and helpful to me. Gail Krueger for her witty explanation of American culture, Idell Dollison for the thoughtful meeting arrangements with Prof. Stubbins and Becky Meline for her patience in answering questions regarding registration and curriculum choices.

Last, I would like to express my gratitude to my family. Thank you for supporting me to pursue my dream and stands as the brightest beacon when I feel lost. There is no word could better express my love to you, but to dedicate this work to you.

Table of Contents

CHAPTER 1: INTRODUCTION and BACKGROUND

1.1 Palladium-Hydrogen System

Hydrogen dissociates when entering the palladium lattice, occupying random octahedral interstices in the fcc palladium lattice [7]. Figure 1.1 shows the phase diagram of Pd-H system. The α phase is the low concentration phase of the system, separated from the high concentration phase α' by a mixed phase (α- α') region. At 300 K, the maximum hydrogen solubility of the α phase is 0.017, while the pure α' phase exists at [H]/[Pd] greater than 0.60. The equilibrium hydrogen pressure stays constant over this two solid phase region [8]. In Figure 1.2 presents the pressure-composition isotherm of palladium versus the absorbed hydrogen, the phase diagram was constructed by connecting the inflection points of different isotherms.

Metal hydrides generally depend strongly on temperature and H_2 gas pressure. Figure 1.3 presents the pressure-composition isotherm of the Pd-H, showing the hysteresis characteristic of the metal hydrides. The plateau region shows the coexistence of the two phases. The hysteresis phenomenon is due to the pressure needed for hydride formation is greater than the decomposition pressure. Flanagan and Clewley [19] have further related the hysteresis to that the chemical potentials of the

metal atoms are not equal. Other researches attributed hysteresis to the plastic deformation during both hydride formation and hydride decomposition. It is also shown by Jamieson *et al.* [20] that the dislocations are created during the decomposition progress, and after the α to α' or α' to α phase changes, the dislocation densities could reach 10^{11}-10^{12} cm^{-2}, compared with the sample under heavy cold working. The cycling process between the two phase regions increase the dislocation density has also been proved in the study from Heuser *et al.* [4, 5].

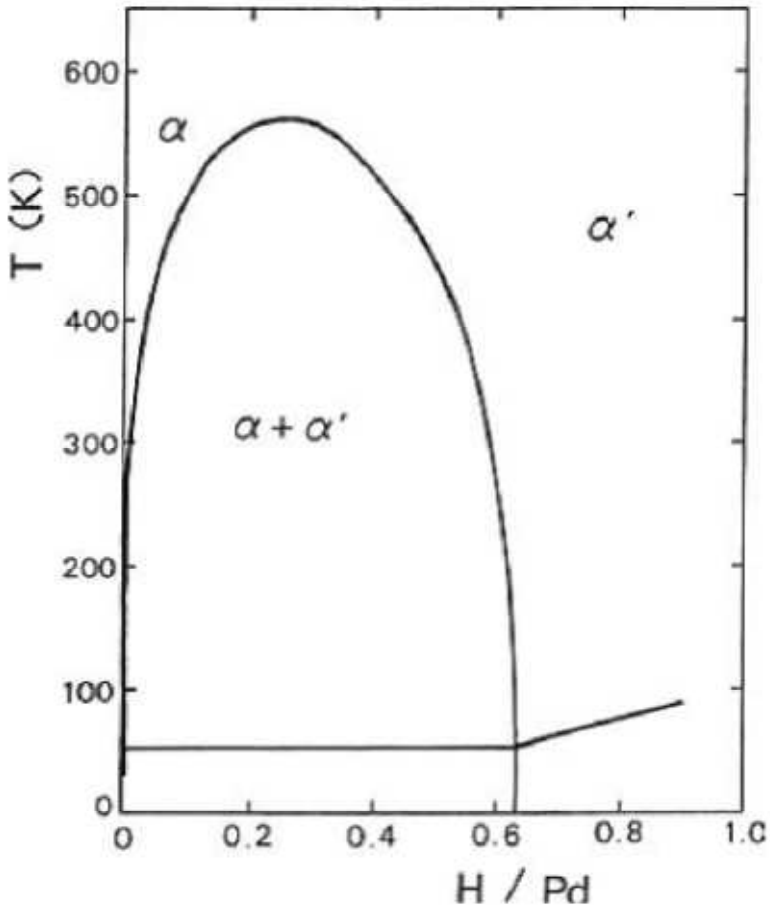

Figure 1.1: Phase diagram of Pd-H system [12].

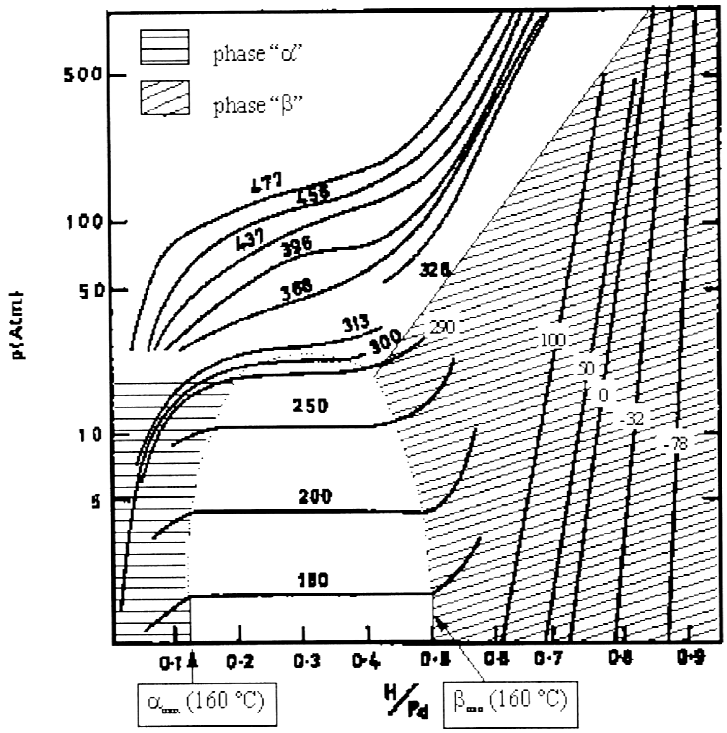

Figure 1.2: Pressure-composition isotherm of palladium versus the absorption molecular hydrogen [38], the temperature scale is based on Celsius.

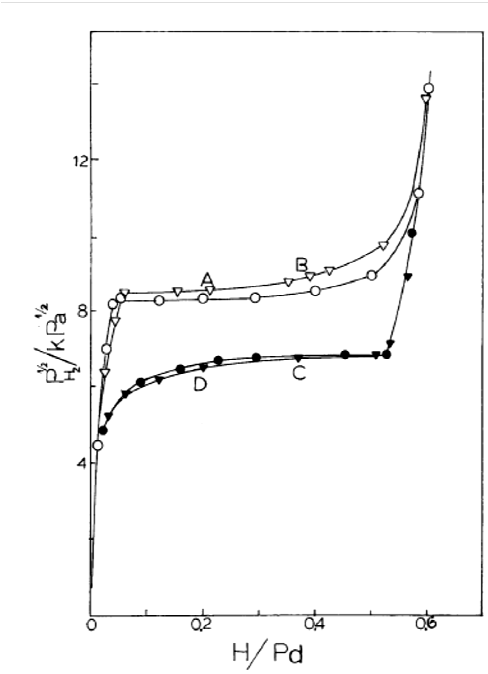

Figure 1.3: Hydrogen isotherm for Pd at 393 K, the ○ mark represents the first scan, and the ∇ represents the second cycle scan for the same sample; the open and filled symbols refer to the adsorption and desorption of H_2, respectively [19].

1.2 Hydrogen Vibration (Harmonic and Anharmonic Effects)

Assuming hydrogen atoms vibrate like a chain of particles with equal space and connected by elastic springs, then the potential energy of the lattice, *V*, can be written as

$$V = \sum_{n} \sum_{m>0} U(x_{n+m} - x_n) \tag{1.2.1}$$

with x_n represents the coordinate of the *n*th particle at any instant time, *U* is the interaction energy between two particles, $x_n = na + u_n$, and u_n denotes the displacement of particle from its equilibrium position. Expanding the potential energy term in Taylor series on the position of $x = ma$, where *a* is the distance between each particle,

$$\begin{aligned} &U(x_{n+m} - x_n) = U(ma + u_{n+m} - u_n) \\ &= U(ma) + (u_{n+m} - u_n)U'(ma) + \frac{1}{2}(u_{n+m} - u_n)^2 U''(ma) + ... \end{aligned} \tag{1.2.2}$$

the first two terms in the Equation 1.2.2 represents a harmonic potential energy, with the higher terms representing an anharmonic potential energy [21]. The former indicates the force and displacement of particles is linear, while the higher terms indicate a non-linear correction to particle displacement.

The vibration of isolated hydrogen atoms in Pd is not purely harmonic; therefore anharmonicity effects should be considered. Isolated hydrogen atoms in potential will deferred by neighboring Pd atoms. For an octahedral site in fcc lattice, which has

cubic symmetry, the potential energy can be rewritten and expanded in the three dimensional form as

$$U(X,Y,Z) = c_2(X^2+Y^2+Z^2) + c_4(X^4+Y^4+Z^4) + c_{22}(X^2Y^2+Y^2Z^2+Z^2X^2) \quad (1.2.3)$$

the energy eigenvalues can be expressed by

$$e_{lmn} = \sum_{j=l,m,n}\left[\hbar\omega_0(j+\frac{1}{2}) + \beta(j^2+j+\frac{1}{2})\right] + \gamma\left[(2l+1)(2m+1)+(2m+1)(2n+1)+(2n+1)(2l+1)\right] \quad (1.2.4)$$

with *l*, *m*, *n* represent the quantum number of vibration in Z, X, Y directions separately, and

$$\omega_0 = \sqrt{\frac{2c_2}{M}}, \quad \beta = \frac{3\hbar^2 c_4}{4Mc_2}, \quad \gamma = \frac{\hbar^2 c_{22}}{8Mc_2} \quad (1.2.5)$$

from equations above, the lowest excitation energies can be derived as

$$\begin{aligned} \varepsilon_{100} &= \varepsilon_{010} = \varepsilon_{001} = \hbar\omega_0 + 2\beta + 4\gamma \\ \varepsilon_{200} &= \varepsilon_{020} = \varepsilon_{002} = 2\hbar\omega_0 + 6\beta + 8\gamma \\ \varepsilon_{110} &= \varepsilon_{011} = \varepsilon_{101} = 2\hbar\omega_0 + 4\beta + 12\gamma \end{aligned} \quad (1.2.6)$$

There is a physical explanation for each parameter. $\gamma \approx 0$ means the three direction of vibrations are independent, positive β represents the potential has the shape of well-like, while the negative β indicates a trumpet-like potential well [12]. See Figure 1.4.

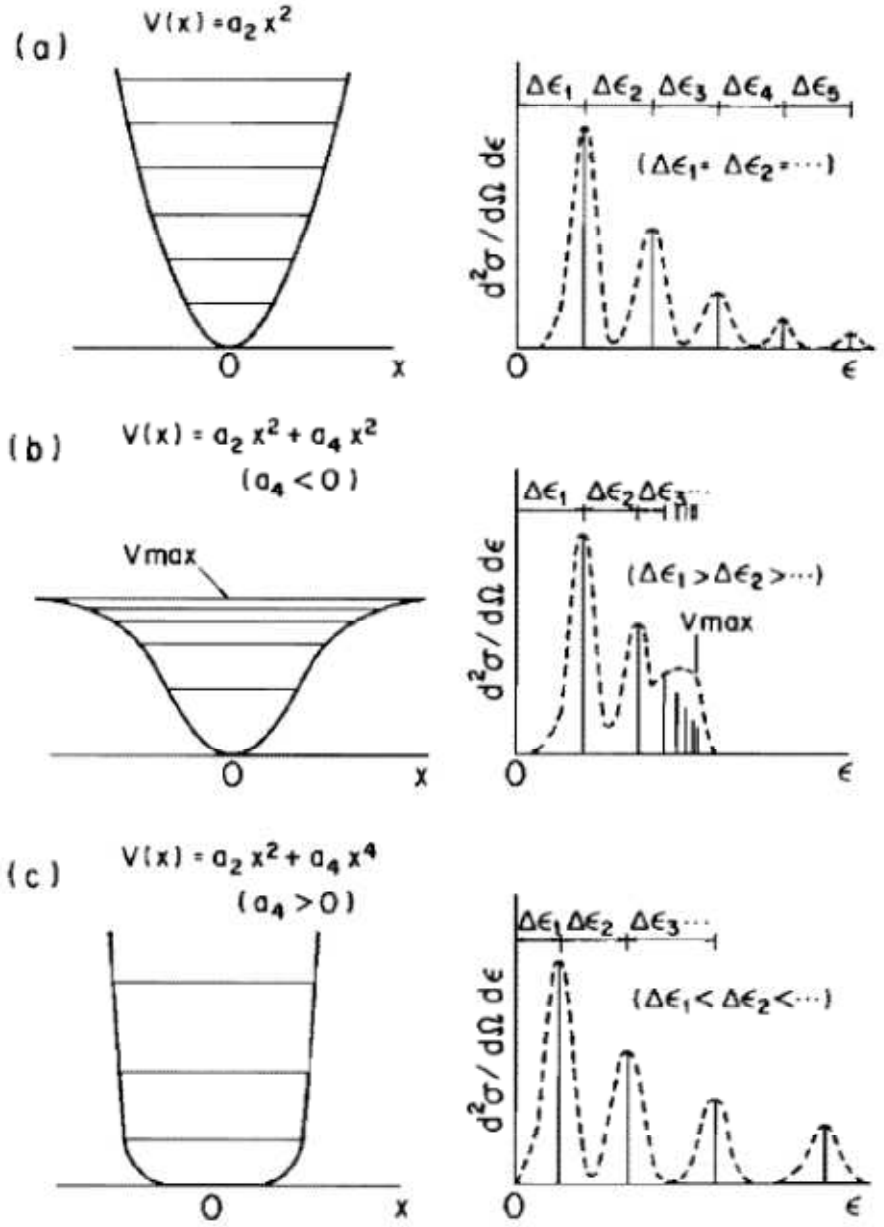

Figure 1.4: Three types of potential well for an interstitial hydrogen atom: (a) harmonic, (b) trumpet-like, and (c) well-like [12].

The degree of anharmonicity can be measured from observed excitation energies using Equation 1.2.7.

$$\Delta E^{H} = \varepsilon_{200} - 2\varepsilon_{100} = 2\beta \qquad (1.2.7)$$

Some of the published anharmoniciry parameters are listed in Table 1.

Table 1: Comparison of the VDOS peak energy, FWHM and the published data.

Published data	Temp. (K)	1st peak	2nd peak	3rd peak	Anharmonicity Parameter 2β [meV]	Reference
$PdH_{0.0008}$	4	59.0				[33]
$PdH_{0.0008}$	295	66				[33]
$PdH_{0.002}$	77	68.5				[29]
$PdH_{0.014}$	295	69.0	137	156	19	[29]
$PdH_{0.015}$	295	68				[33]
$PdH_{0.63}$	80	56			9.7#	[28]
$PdH_{0.63}$	4	58.6	116.3	135.5	19.2	[33]
$PdH_{0.099}$	15	56.0	113*	134*		[42]
PdH	30	57	122			[26]
PdH	80	57	121			[26]

*: The data was not identified in the original paper, but measured through the proportional scale of the experimental figure.

#: The data was derived based on the isotope dependence of the fundamental transition energies by using the equation $(1-1/\sqrt{2})\Delta E^{H} = \hbar\omega_0{}^{H} - \sqrt{2}\hbar\omega_0{}^{D}$ [39].

1.3 Hydrogen-Dislocation Interaction in Deformed Palladium

In this chapter, the fundamental concepts of hydrogen-dislocation interactions and trapping behavior are introduced. The explanation of experimental measurements in this study depends on these concepts. The Fermi-Dirac model, in Equation 1.3.1, was used to describe the absorption of solute atoms in the dislocations [15]. The relationship between the bulk concentration C_0 and the hydrogen concentration near the dislocation field, $C(r,\theta)$ can be expressed in Equation 1.3.1.

$$\frac{C(r,\theta)}{1-C(r,\theta)} = \frac{C_0}{1-C_0}\exp\left(\frac{-\sigma_h \upsilon}{k_B T}\right) \qquad (1.3.1)$$

where σ_h is the hydrostatic stress associated with the dislocation, υ is the internal volume expansion corresponds to the interstitial solute atoms, k_B is the Boltzmann constants, and T is the temperature. $\sigma_h \upsilon$ represents W, the interaction energy between solute atoms and the defect.

The internal volume expansion υ of interstitial hydrogen can be related to the partial molar volume of hydrogen, V_H by

$$\upsilon = V_H \left(\frac{1+\nu}{1-\nu}\right)\frac{1}{3N_A} \qquad (1.3.2)$$

with N_A is Avogadro's number and ν is the Poisson's ratio [15].

The elastic interaction energy associated with hydrogen trapping at edge

dislocation is given by [16]

$$\sigma_h \upsilon = -\frac{1}{3}(\sigma_{rr} + \sigma_{\theta\theta} + \sigma_{zz})\upsilon = \frac{\mu b_e \upsilon}{3\pi}\left(\frac{1+\nu}{1-\nu}\right)\frac{\sin\theta}{r} \qquad (1.3.3)$$

here σ_{ii} are the normal components of the edge dislocation stress field, μ is the shear modulus, b_e is the edge component of the Burgers vector, θ is the angle between the glide plan and the point of interest, r is the distance from the interstitial atoms to the dislocation sites. The geometry is shown schematically in Figure 1.5 [17].

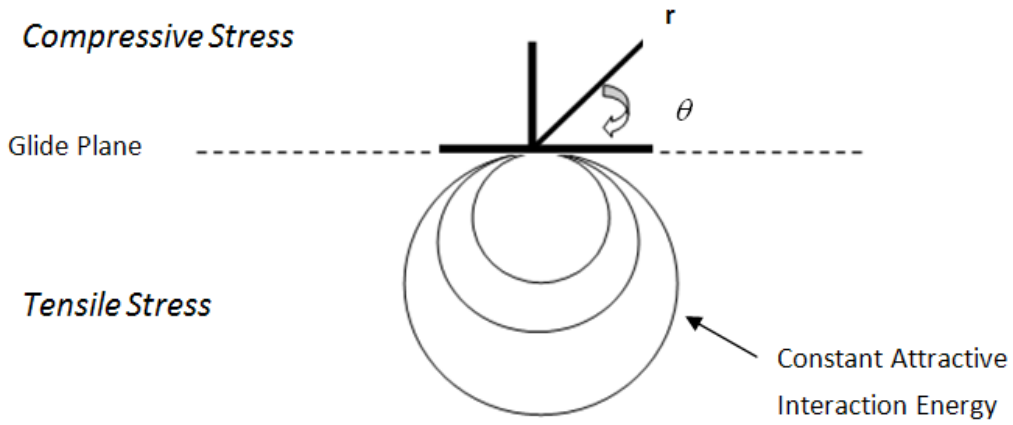

Figure 1.5: Schematic diagram of edge dislocation in polar coordinates, the circles represent the constant interaction energy [17].

The region above the glide plane is under compressive stress, while the region below is under tensile stress. The hydrogen solute will preferentially trap below the glide plane and at the core.

The integral number of solute hydrogen atoms absorbed in the elastic field of the dislocation, N/L, is given as

$$\frac{N}{L} = \int_{R_{\min}}^{R_{\max}} r dr \int_{0}^{2\pi} \mathrm{d}\theta \left[C(r,\theta) - C_0 \right] \qquad (1.3.4)$$

with R_{min} and R_{max} represent the inner and outer radius cutoff respectively, this ignores core trapping. In general, the R_{min} equals to one Burgers vector, the R_{max} is usually chosen to be one half of the average dislocation separation [16].

Insertion of the Fermi-Dirac approximation into Equation 1.3.4 yields

$$\frac{N}{L} = \int_{R_{\min}}^{R_{\max}} r dr \int_{0}^{2\pi} \mathrm{d}\theta \left[\frac{\xi + 1}{\xi + \mathrm{e}^{\sigma_h \upsilon / kT}} - 1 \right] \qquad (1.3.5)$$

where $\xi = \frac{C_0}{1 - C_0}$. The contribution of core trapping hydrogen is not considered in Equation 1.3.5.

The research of Kirchheim *et al* [18] stated that the additional interaction forces between hydrogen atoms need to be considered in the dilated region close to the core of an edge dislocation. The higher stress caused by distortion leads to concentration of hydrogen atoms, the hydrogen binding energy near dislocation core is -0.6 eV based on the study of Kirchheim. The core contribution to the excess hydrogen can be estimated

as

$$\left(\frac{N}{L}\right)_{core} = \alpha\pi R^{2}{}_{\min} N_{site} \qquad (1.3.6)$$

where α is the hydrogen site occupation fraction in the Pd hydride phase and N_{site} is the octahedral site density of Pd. The difference of screw or edge dislocation was not identified in Equation 1.3.6.

1.4 Phonons

Phonon is the term used to describe the quantized lattice vibrations [13]. The phonon density of states can be studied through IINS experiments.

Theory of lattice dynamics

The concept of lattice dynamics will be addressed before discussing more detail of phonons and applications. For a crystal having *r* atoms, there are *3r* normal modes for each wavevector *q*. Each mode is independent and has its own frequency and polarization factor to indicate the displacement direction of each atom. For $q \to 0$, three modes of the angular frequencies tend to be zero, and the remaining *3r* -3 tend to be a finite value. The former are defined as acoustic modes and refer to atoms vibrating in phase in the unit cell, while the latter are known as optic modes and indicate the atoms vibrate out of phase by 180° [12].

Considering a system with equally spaced *a*, alternate different mass atoms, *m* and

M. For the acoustic branch, as q→0, the particles vibrate in phase with the same amplitude; as q→$\pm\pi$/2a, the amplitude of light particles tend to zero and only left with the heavy particles continue to oscillate. For the optical branch, as $q \to 0$, the particles *m* and *M* vibrate out of phase by 180°, which indicates an opposite direction displacement; as q $\to \pm\ \pi/2$a (the first Brillouin zone), contrary to the case in acoustic branch, the light particles oscillate while the vibration of heavy particles tend to zero [21]. The illustration is shown in Figure 1.6. Therefore, in Pd-H system, the optic mode vibration of hydrogen atoms has distinctive higher frequency than the acoustic mode due to a lower mass than Pd atoms.

For acoustic and optical branch, each branch has two vibrational modes, longitudinal and transverse modes. The particle in longitudinal mode vibrates along the direction of wave propagation, while the particle in transverse mode vibrates perpendicular to the direction of wave propagation. Figure 1.6 shows the typical phonon dispersion curves in $PdD_{0.63}$. The transverse optic modes of deuterium show the isolated oscillation movement of each deuterium in the system, while the longitudinal optic modes represent the dispersion relation between the D-D atoms.

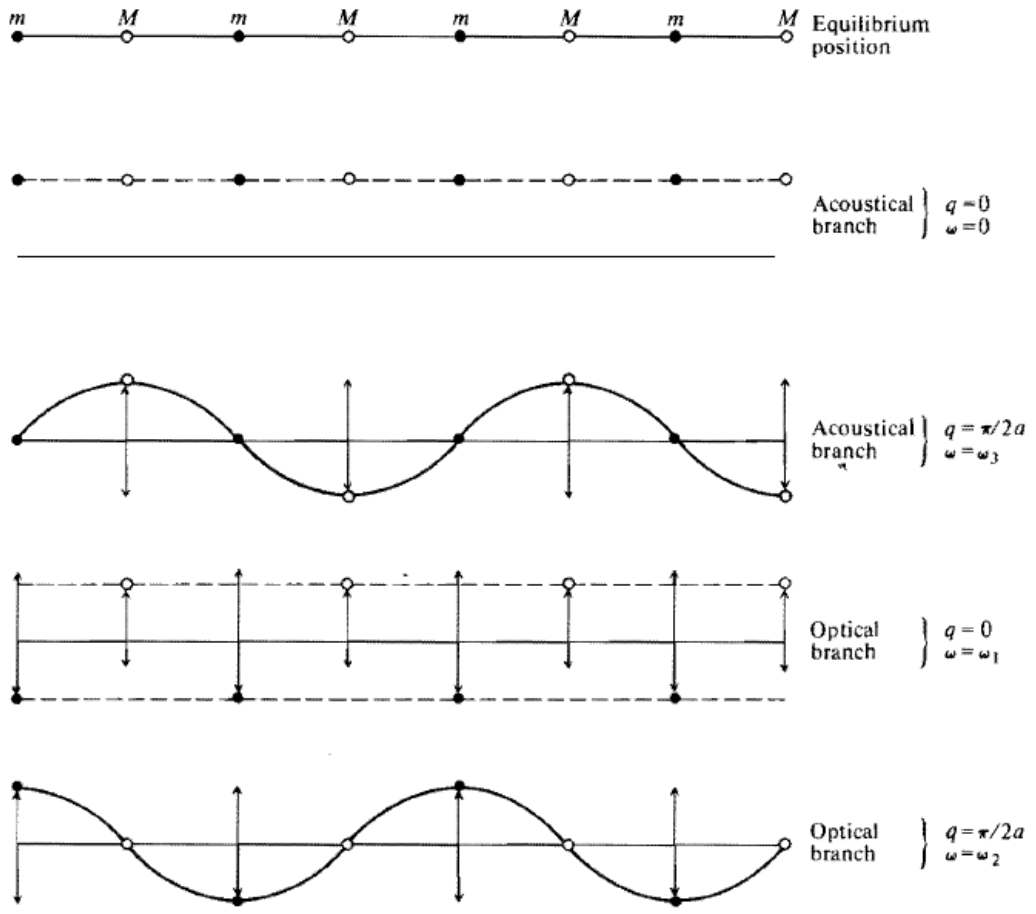

Figure 1.6: Transverse displacements of the chain for the acoustical and optical branches corresponding to q=0 and q= π /2a [21].

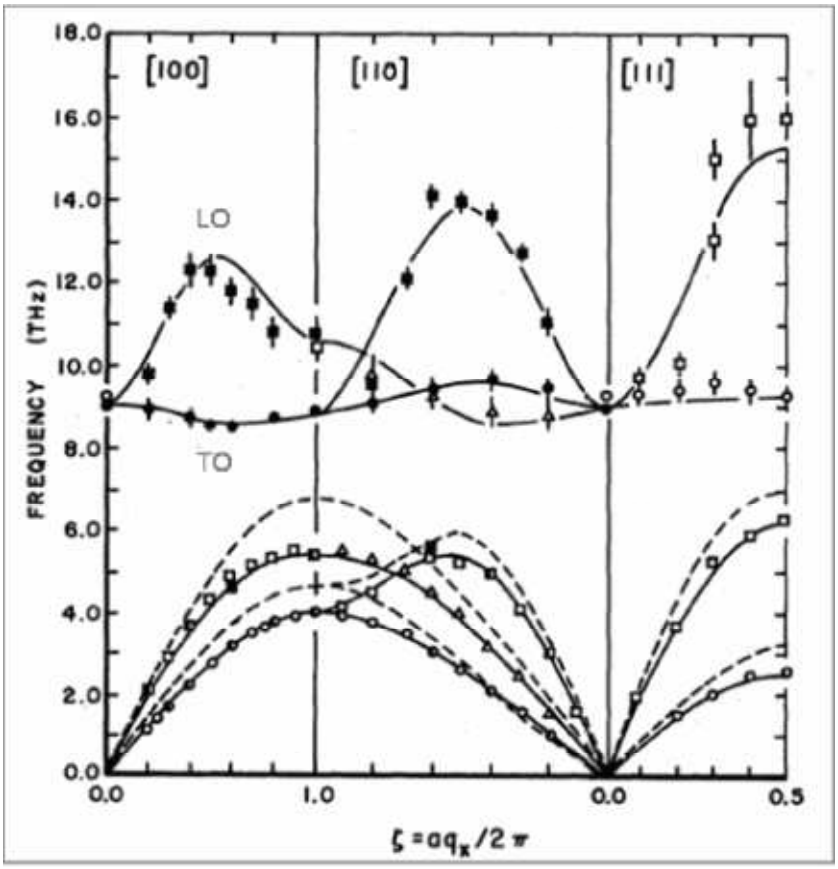

Figure 1.7: Dispersion curves in $PdD_{0.63}$, with filled and open symbols represent the data taken at 150 and 295 K respectively. The dash line is for pure Pd. Taken from Rowe *et al.* (1974) [25].

1.5 Coherent and Incoherent Inelastic Neutron Scattering

The neutron scattering can be separated as elastic and inelastic scattering, depending on the difference of incident and scattered neutron energy. The elastic and inelastic scattering could be further categorized as coherent and incoherent individually. Due to the periodic arrangement of nuclei in a crystal, the scattering waves caused by neutron may interfere with scattering waves from other nucleus in a crystal; this interference is known as coherent scattering. On the contrary, if the nuclei scattered

independently, the scattering is known as incoherent scattering. In general, the information of dispersion relations could be achieved from inelastic coherent scattering, while the inelastic incoherent scattering provides the information for the frequency distribution function [21].

For a set of fixed nuclei, the differential angular cross section could be expressed by [23]

$$\frac{d\sigma}{d\Omega} = \left[\left\langle b^2 \right\rangle - \left\langle b \right\rangle^2\right] + \left(\frac{1}{N}\right)\left\langle b \right\rangle^2 \sum_{ij} \exp\left[i\kappa \cdot (R_i - R_j)\right] \quad (1.5.1)$$

with b as the neutron scattering length, a measure of the strength of the scattering at a particular nucleus for a given total spin state J (J= nuclear spin$\pm$ 1/2); N is the number of the nuclei; $\kappa = k - k'$ is the scattering vector and R is the position of the nuclei. The first term, $[\langle b^2 \rangle - \langle b \rangle^2]$, is the incoherent scattering while the remaining term is the coherent scattering. It is in general to separate these two terms in more through discussions and this could be referred to the discussion presented below.

One of the advantages of using inelastic neutron scattering spectra to study vibrations of hydrogen atom is the uniquely high incoherent scattering cross section of hydrogen atoms compared with other heavier atoms. This advantage makes IINS a suitable technique to study the dynamic information of the scattering system. The incoherent scattering cross sections of some elements are listed in Table 2.

Table 2: Values of σ_{coh} and σ_{inc}.

Element	Z	σ_{coh}	σ_{inc}
^{1}H	1	1.8	80.2
^{2}H	1	5.6	2.0
Pd	46	4.5	0.09

(a) The units of σ_{coh} and σ_{inc} are 10^{-28}m^2.

(b)The ^{1}H and ^{2}H values are taken from Koester (1977)[14], and the Pd data is taken form reference [22].

Coherent Inelastic Neutron Scattering

The coherent scattering cross-section can be expressed as below [23]

$$(\frac{d^2\sigma}{d\Omega dE'})_{coh} = \frac{\sigma_{coh}}{4\pi}\frac{k'}{k}\frac{1}{2\pi\hbar}\sum_{jj'}\int_{-\infty}^{\infty} < \exp\{-i\kappa\cdot R_{j'}(0)\}\exp\{i\kappa\cdot R_j(t)\} > \exp(-i\omega t)dt \quad (1.5.2)$$

with the scattering vector as $\kappa = k - k'$, the cross-section as $\sigma_{coh} = 4\pi(\bar{b})^2$. Equation 1.5.2 represents the number of neutrons scattered into an element of solid angle $d\Omega$ with energy lying between E' and $E' + dE'$ when unit flux of neutron is incident on the scattered sample. The coherent scattering considers the positions of same particle at different times and the positions of different particle at different times, which results to the interference effects [23].

Incoherent Inelastic Neutron Scattering

The incoherent scattering cross-section can be expressed as below.

$$(\frac{d^2\sigma}{d\Omega dE'})_{inc} = \frac{\sigma_{inc}}{4\pi}\frac{k'}{k}\frac{1}{2\pi\hbar}\sum_{j}\int_{-\infty}^{\infty} < \exp\{-i\kappa\cdot R_j(0)\}\exp\{i\kappa\cdot R_j(t)\} > \exp(-i\omega t)dt \quad (1.5.3)$$

with the scattering vector as $\kappa = k - k'$ and the cross-section as $\sigma_{inc} = 4\pi(\overline{b^2} - (\bar{b})^2)$. In incoherent inelastic scattering, the equation only depends on the positions of the same nucleus at different times without the interference effects in coherent scattering.

Phonon Density of States

In quantum physics, the phonon density of states represents the collective number of allowed energy states per unit energy interval of a system. Because the neutron scattering of hydrogen atoms is dominated by incoherent scattering, incoherent scattering will be used as an example to explain the concept of phonon density of states.

In Equation 1.5.3 the self intermediate function can be defined by

$$I_s(\kappa, t) = \frac{1}{N}\sum_j < \exp\{-i\kappa \cdot R_j(0)\} \exp\{i\kappa \cdot R_j(t)\} > \qquad (1.5.4)$$

where *N* is the number of nuclei in the scattering system, and the incoherent scattering function is defined as below

$$S_{inc}(\kappa, \omega) = \frac{1}{2\pi\hbar}\int I_s(\kappa, t) \exp(-i\omega t) dt \qquad (1.5.5)$$

which is the Fourier transform of the intermediate function, then we rewrite the incoherent scattering cross-section with Equation 1.5.4 and Equation 1.5.5, the incoherent scattering cross-section can be rewritten as

$$(\frac{d^2\sigma}{d\Omega dE'})_{inc} = \frac{\sigma_{inc}}{4\pi}\frac{k'}{k} N S_{inc}(\kappa, \omega) \qquad (1.5.6)$$

In Equation 1.5.6 form, the incoherent scattering function not only emphasizes the

dynamics of each individual atom in the sample better than the Equation 1.5.3 form but also directly relates to the intensity by $S_{inc}(\kappa, \omega)$, the dynamic structure factor, when summed over all the atoms in the sample [13].

The incoherent scattering law, also known as dynamic structure factor, for one phonon approximation can be expressed as below

$$S_{inc}(\kappa, \omega) = \frac{\hbar}{4M|\omega|}(\bar{n} + \frac{1}{2}(1 \pm 1))\kappa^2 g(\omega) \exp(-\kappa^2 < u^2 >) \qquad (1.5.7)$$

where $g(\omega)$ is the phonon density of states, also known as frequency distribution function of the scattered nucleus and defines the number of vibrations per wavevector; $\bar{n}$ is the average number of phonons at temperature T, defined as $\bar{n} = [\exp(\hbar\omega / kT) - 1]^{-1}$; and $\kappa = k - k'$; the plus and minus sign in Equation 1.5.7 represents the neutron energy loss or gain, respectively [12].

Equation 1.5.6 and Equation 1.5.7 indicate that the incoherent scattering cross-section is directly proportional to the phonon density of states; therefore, by using the IINS technique to measure the energy distribution of neutrons, the frequency distribution spectrum is derived.

1.6 Free Recoil IINS Theory

In the metal hydride system, three different types of proton interaction could be expected. (i) Ideal gas of protons moving almost freely in the crystal. (ii) Protons trap in crystal defects without forming strong covalent bond. (iii) Protons trap in crystal

defects with strong covalent bond. Fillaux *et al*. [24] indicated that most of the protons are not covalently bonded in the crystal but are rather mobile. It is reasonable to suggest that the first and second types of interaction contribute to the free recoil signals collected by the detector. The second type of interaction, with the stuck atom gains sufficient energy from the neutron that its recoil could also appear as a free atom.

The impulse approximation is used to describe the scattering by an atom from its initial state in the bulk material to a final state as a free particle [36]. The impulse approximation assumes that the binding forces on the target particle during the collision with the incident particle are ignored. The equation is defined as below

$$\lim_{Q\to\infty} S(Q,E) = \int_{-\infty}^{\infty} n(|p|)\delta(E - E_r - \frac{\hbar Q \cdot p}{M})dp \qquad (1.6.1)$$

where Q and E represents the momentum and energy transfer of the scattering neutron, the recoil energy $E_r = \frac{\hbar^2 Q^2}{2M}$, $n(|p|)$ is the atomic momentum distribution of the scattering atom and can be expressed as

$$n(p) = \frac{1}{(2\pi\sigma_p{}^2)^{3/2}} \exp(-\frac{p^2}{2\sigma_p{}^2}) \qquad (1.6.2)$$

with σ_p as the width of the momentum distribution determined from the experimental fitting. By using the impulse approximation, the dynamic structure factor can be derived as

$$S(Q,E) = \frac{M}{\hbar Q \sigma_p (2\pi)^{1/2}} \exp(-\frac{(E - E_r)^2}{2\sigma_p{}^2 \hbar^2 Q^2 / M^2}) \qquad (1.6.3)$$

and will be latter used in the recoil subtraction method.

In this study, the intensity generated by free recoil protons are believed to have considerable effect on the measured S(Q, E), more discussion and related published research could be referred to Chapter 2.3.

CHAPTER 2: LITERATURE REVIEW OF NEUTRON SCATTERING EXPERIMENTAL RESULTS

The published research in neutron scattering is addressed in this chapter. This research includes the coherent inelastic neutron scattering and the incoherent inelastic neutron scattering which mainly focused on representative studies. This chapter concludes with related experiments in free recoil protons.

The neutron was first discovered by J. Chadwick in 1932 in the experiment of beryllium bombarded with α-particles. More detailed properties are listed in Table 3 [12]. Neutrons are scattered by nuclei, depending on whether they exchanged energy with the nuclei or not, the interaction can be further classified as elastic or inelastic scattering. The energy lost or gained by a neutron in the interaction with crystals can be viewed as due to the emission or absorption of phonons. By measuring the scattered angles and energy of the scattered neutrons, one can yield both structural and dynamic information on the scattering system through phonon spectra.

Table 3: Properties of the neutron [12].

Property	Value
Rest mass	
m_n/kg	1.6749286×10^{-27}
m_n/u(a)	1.008664904
m_nc^2/MeV(b)	939.56563
Spin, *I*	1/2
Charge number, z	0
Mean life/s	889.1

(a) On the unified atomic mass scale, relative to the mass of carbon-12 defined as 12.
(b) Energy equivalent.

The study of Miller and Brockhouse [40] employed the neutron scattering technique to investigate the lattice behavior and electronic specific heat of palladium. Their research found two anomalies in the dispersion curves for palladium, one is the slope increase of the dispersion curve at wave vector about $(2\pi/a)[0, 0.35, 0.35]$, the other is the broadness and shifting of the anomaly to a lower wave vector when temperature increased. By using the frequency data acquired from the measurement, they estimated the electronic specific heat of palladium through the comparison of with and without anharmonic corrections. The result agreed well with other calculations using rigid-band and Debye models. Brockhouse is also a Nobel Prize laureate for his pioneering achievements in the development of neutron scattering techniques in studying condensed matter.

2.1 Coherent Inelastic Neutron Scattering

Coherent Inelastic Neutron Scattering (CINS) has been employed to study phonon dispersion curves of PdD_x in single crystals, while for PdH_x the direct measurement of phonon dispersion curves is hard to extract due to the high incoherent cross session of hydrogen atoms.

Rowe and Rush *et al.* [25] are among the earliest researchers in using coherent neutron scattering to study the dispersion effect of $PdD_{0.63}$. Their research found the large dispersion in the longitudinal optics modes are dominated by deuterium motions, and indicated that the strong interactions between deuterium atoms need to consider more than just nearest neighbors. The electronic structure of the alloys was important in explaining the lattice dynamics of palladium hydride, and this was confirmed by the well matched of experimental results with the electronic band-structure calculations instead of the rigid-band model.

Glinka and Rowe *et al.* [41] used the nonstoichiometric model together with the previously derived force constant for PdD to demonstrate that the prior method in treating a nonstoichiometric system as stoichiometric is valid in deriving the Pd-D force constants; however, the D-D force constants were underestimated by more than 50 %. They also introduced the mass effects that the force constants for Pd-D were about 20% smaller than the Pd-H, and established that the effective bonding is weaker

in the deuteride system than in the hydride system.

This thesis research is only studying palladium hydrogen system through IINS technique, but these two researches in CINS provides an in depth knowledge in explaining the neutron spectra in IINS experiments.

2.2 Incoherent Inelastic Neutron Scattering

The first measurement of the dynamics of Pd-H system was occurred in 1961, but the main progress in this area developed in the 1970s and 1980s. The researches mentioned below are in chronological order. In the early neutron scattering measurements, Chowdhury and Ross [26] used the down scattering facility EDNA to investigate the localized modes associated with interstitial hydrogen in the β-phase of Pd and Pd-Ag alloys. Their research found the dependency on temperature and silver content from both the width of the fundamental peak and the first harmonic peak, the width of both peaks increase with silver content and temperature, which are attributed to local disorder and anharmonic effects.

Drexel and Murani *et al.* [27] employed the INS method to verify the isotope effect in α-phase Pd hydride. The time-of-flight measurements indicate the existence of an anharmonic potential for the hydrogen atom in α-phase Pd hydride. In triple axis measurements, they found the formation of hydrogen atom clusters at higher concentration and with insufficient annealing treatment, this cluster distorted the local

host lattice.

In the research of Rush and Rowe *et al.* [29], they observed two second excited levels $\omega_2^{(1)}$ and $\omega_2^{(2)}$ in the α-phase PdH_x, with relationships of $\omega_2^{(1)} = 2\omega_1$ and $\omega_2^{(2)} = 2\omega_1 + 19\ meV$. The derivations were based on the model of normal harmonic potential and the lowest order non-vanishing anharmonic contribution, discussed in Equation 1.2.6. The observed isotope shift for α-PdH_x was attributed to the anharmonicity, though the interaction energy between the nearest hydrogen atoms was not considered. For more complete anharmonicity parameters can be found in Table 1, in Chapter 1. This research also provided a reference example for the location of α phase Pd-H at first harmonic peak, 69.0 ± 0.5 meV for H concentration from 0.002 to 0.014. See Figure 2.1. Note that according to the fitting results in $PdH_{0.014}$ the second harmonic peak and the shift peak were located at 137 and 156 meV separately.

The behavior of optical phonons was studied by Kolesnikov *et al.* [42] using the multiconvoluton of the one phonon spectrum. In their research, the experimental generalized vibrational density of states (GVDS) was first assuming a one-phonon scattering. On the second and following steps, the difference between the calculated GVDS and the experimental one was used to replace the one-phonon spectrum. The calculated results well reproduced the experimental measurements. Figure 2.2 shows the one-phonon and multiphonon spectra for $PdH_{0.99}$.

Ross *et al.* [31] investigated the orientation-dependent anisotropy at high energy transfer ranges to 800 meV, they also found the result agree well with the first-principles calculations and use this to confirm the shape of the potential well.

Kemali *et al.* [32] took the previous study in anisotropy and anharmonicity and applied to the *Ab Initio* calculations in deriving the dynamic structure factor for IINS in single crystal palladium. The calculation was compared with experimental measurements.

Until recently, the Pd-H system studies have been focused on the H at interstitial sites of palladium, but the vibrational density of states of hydrogen trapped at dislocations have not been fully studied. Heuser *et al.* [33] used the IINS techniques to investigate the vibrational density of states of hydrogen trapped at dislocations, although it is difficult to fully eliminated the intensity caused by bulk interstitial hydrogen. Their research also presented the investigation of the local octahedral trapping environment by comparing the location and width of the first harmonic peak. The result served as the evidence of a $\alpha \rightarrow \beta$ transition from room temperature to low temperature within the distorted environment of dislocations.

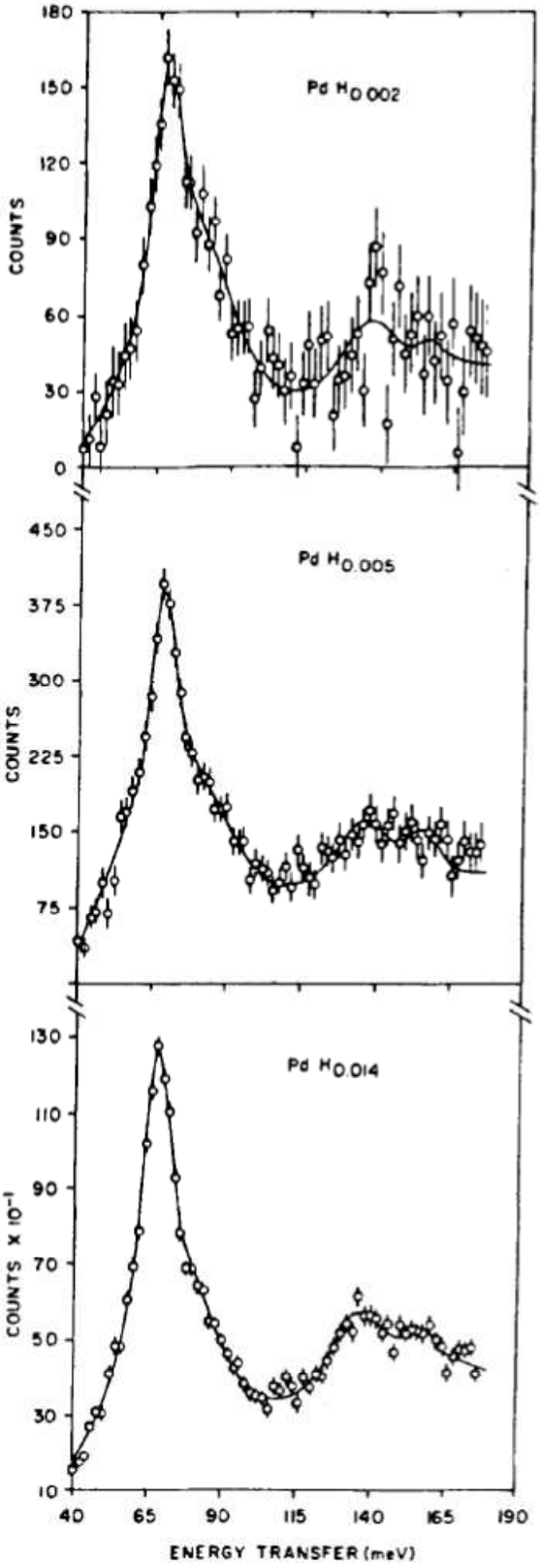

Figure 2.1: IINS spectra for α-PdH_x at 295 K. The first harmonic peak for all concentration is located at 69.0±0.5 meV. Note that a second broad max around 138 meV with a high energy shoulder. The lines are the fitting to the data [29].

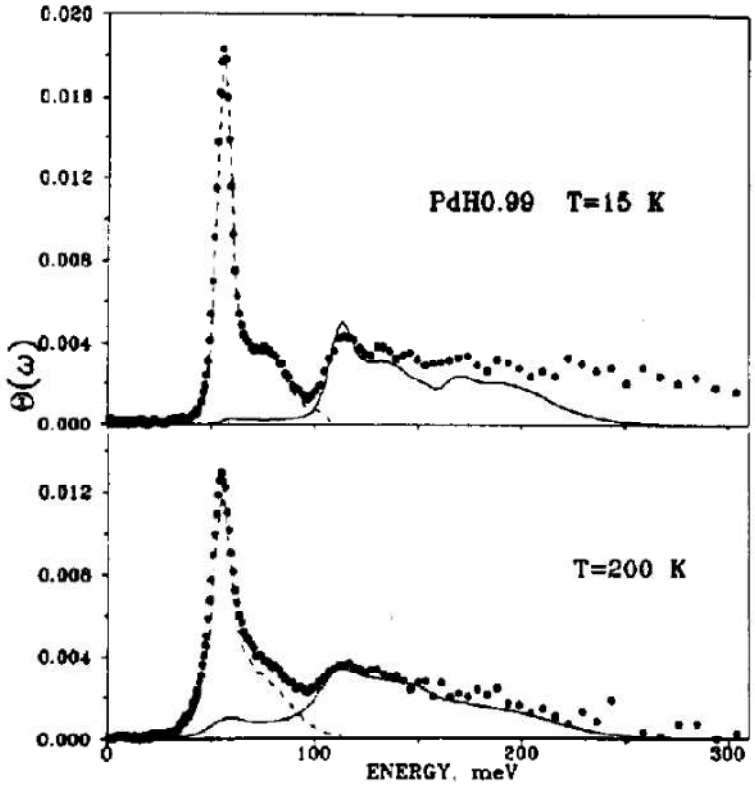

Figure 2.2: GVDS spectra for $PdH_{0.99}$. The dashed curves are for one-phonon scattering and the solid curves are for multiphonon scattering [42].

Trinkle *et al.* [34] applied the *ab initio* theory to the Pd-H system to predict the vibrational excitations for H from zero degree to room temperature. The *ab initio* calculation was compared with the IINS measurements to observe the formation and dissolution of nanoscale hydrides around dislocation cores in palladium. By separating the effects from each parameters including nonuniform hydrogen site occupancy due to strain and H-H interaction, quantum-thermal vibrational displacements for neighboring Pd and the anharmonic potential energy, the research provides an *in situ* characterization of the hydrogen environment evolution with temperature.

2.3 Free Recoil Neutron Scattering

The free recoil energy generally describes with a quadratic dispersion equation, $\Delta E = (\hbar Q)^2 / 2M$, where M is the effective mass of the recoiling particle and ΔE is the energy transfer. In the previous experiment by Fillaux *et al.* [24] revealed that the effective mass of the recoil signal equals to the mass of hydrogen atom. Although the compounds (MnO_2) Fillaux used were different from the Pd hydride system in this experiment, and the hydrogen formation mechanisms are different, yet the result presented a successful method for the derivation of the recoil mass. From the research of Fillaux *et al.* [24], the signal for free recoil protons has been observed across large energy and momentum transfer ranges from 30 to 4000 cm^{-1}. But it is the one that generated in higher energy and momentum transfer range that we are interested, since this research is focusing on the second order harmonic peak in the palladium hydride system, and this peak falls in the same range with free recoil signal. Developing an efficient method to subtract the recoil signal will help us better investigate the atomic mechanism in the Pd-H system. The detail description of the recoil subtraction method will be referred to Chapter 3.3.3.

Another recoiling molecule experiment had been conducted by Fillaux *et al.* [35] to study the dynamics of protons. By using the IINS with energy up to 1 eV and momentum transfer range from 0 to 40 $Å^{-1}$ in γ-MnO_2 at 30, 100 and 200 K, the S(Q,ω)

maps reveal a band of intensity due to recoil of free particles with effective mass of $\approx 1\text{amu}$. The intensity of free recoil protons was observed over large energy and momentum transfer range, see Figure 2.3. The high intensity band was identified through the variance of proton density, as the proton density falls, the intensities of the superimposed bands decrease, and then disappears completely when the samples have been thoroughly dehydrogenated. Based on the results, they concluded the scattering band is from some hydrogenous species and not a background arising from the matrix, and is incompatible with an isolated gas at the temperature of the sample; because the detected intensity is one order higher. Figure 2.4 provides the view of the recoil spectrum and minimizes the contribution from the vibrations of bound protons. (According to the sample preparation, there is about 0.32 wt.% H^+ in vacancies and roughly 0.05 wt.% H^+ associated to Mn^{3+} ions.) Thus the contributions for bound protons were negligible. The figure reveals two Gaussian-like curves centered at 21.4 and 510 meV. By using the recoil energy equation $E_R = \hbar\omega_R = \hbar^2 Q^2/2M$, these peaks correspond to effective masses of 27 amu (Al sample can) and 1.1 amu (H).

In the research of Olsen *et al.* [44], they studied hydrogen in high porosity carbon substrates and utilized the Q-dependence characteristic of the recoil intensity to decompose the two dimensional spectra (E v.s Q) into mobile and bond types. When the type of bond excitations represented the rotational excitations that are

translationally bound and shows no recoil broadening, the mobile excitations represented a broad peak extending to high energy region and are translationally mobile in the direction parallel to the substrate. Based on their research with an incident neutron energy of 30 meV, at the high energy region, only mobile transitions were present. Therefore by separating the two types of excitations and performing a fit to the high energy part then extending to the low energy region, the subtraction of the fitting will leave the scattering intensity from bound states. For their research, the spin character of neutron is also considered, but not in this study, where the method was used as a reference.

Schirato *et al.* [36] used the impulse approximation to describe the dynamic structure factor S(Q,ω), the equation is described in below.

$$S(Q,E) = \frac{M}{\hbar Q \sigma_P (2\pi)^{1/2}} \exp\left(-\frac{(E-E_R)^2}{2\sigma_P{}^2 \hbar^2 Q^2 / M^2}\right) \qquad (2.3.1)$$

with σ_p is the width of the momentum distribution determined; E_R the recoil energy.

Equation 2.3.1 is the same with Equation 1.6.3, but labeled separately for explanation convenience. It shows that the observed scattering will have Gaussian shape centered at the recoil energy with a width proportional to the width of the momentum distribution, which corresponds to the result found by Fillaux *et al.* [35] in Figure 2.4 and the previous research by Sokol *et al.* [43]. This equation is the cornerstone for our recoil subtraction method in Chapter 3.3.3.

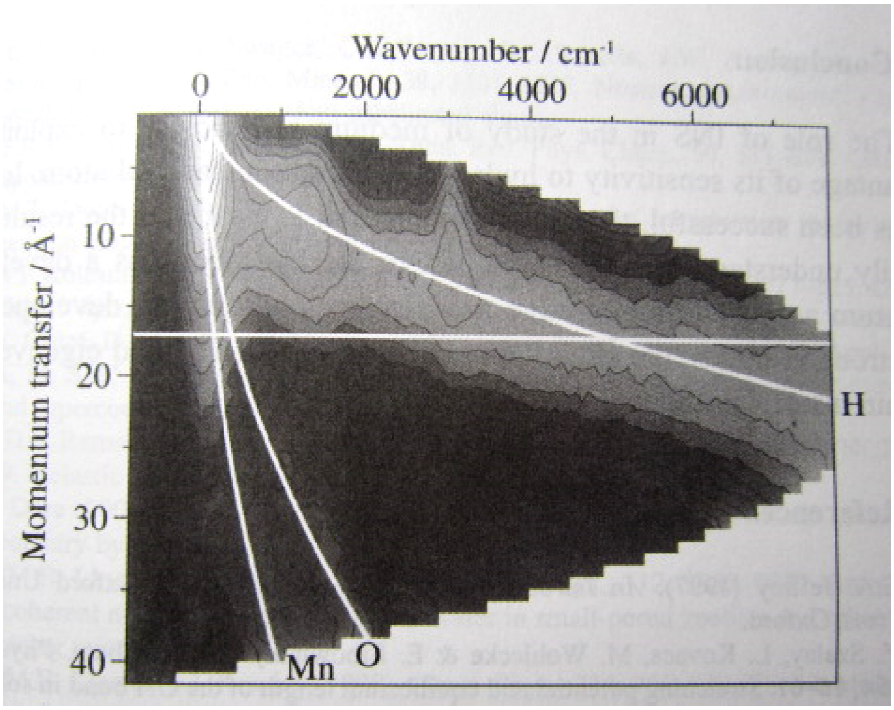

Figure 2.3: The INS spectrum (MARI, ISIS) of manganese dioxide, showing the response of a free proton curve calculated by quadratic dispersion equation and labeled with H [35].

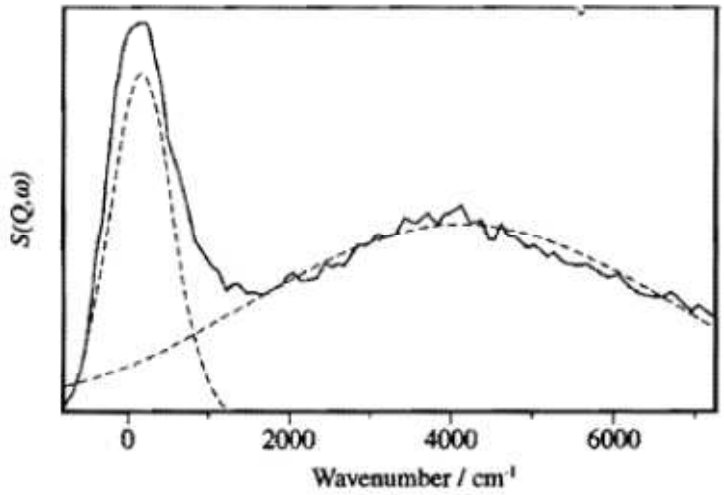

Figure 2.4: The INS spectrum of manganese dioxide, taken along the $Q = 17(1/\text{Å})$ cut, see Figure 2.3 [35].

CHAPTER 3: EXPERIMENTAL

3.1 Sample Preparation

Cold-rolled polycrystalline Pd sheet was supplied by Alpha Aesar with a purity of 99.98 % (metal basis) and thickness of 0.25 mm. These Pd sheets were cold rolled in the as-received condition and cut into 0.5 by 5 cm pieces and used in the IINS measurements. Before exposing to the hydrogen environment, the surfaces of the Pd samples were abraded with grit papers wetted with water and rinsed with methanol in order to remove the oxide layer and expedite the absorption kinetics of hydrogen gas. Then the samples were cycled twice across the Pd hydride miscibility gap at around 70 ℃ before the IINS measurement. Cycling process is known to generate significant dislocation density in Pd [4, 5] and the process was performed by filling hydrogen in the Al sample can attached to the manifold system, the schematic diagram of the manifold system is shown in Figure 3.1.

The manifold system was designed to carry the sample during the outgassed and hydrogen induction cycling process. There are three major components for the manifold systems, including a pumping section, a manifold gas-loading section and a gas line section. The pumping section consists of a Leybold Dry Oil Free HV pump system, BMH70 DRY, a converter from ISO-large flange (LF) to conflate flange (CF)

and a UHV below a sealed valve manufactured by Vacuum Generations LTD. The manifold gas-loading section, was made by stainless steel and has a total volume of 2127.9 cm^3 with an extra pre-calibrated stainless steel cylinder with known volume of 1012 cm^3 attached, and the cylinder was used to determine the volume of gas-loading section. The system was capable of achieving an ultimate pressure of 8×10^{-8} Torr.

Apart from the main manifold system components, there are peripheral equipments including two pressure gauges and an ion gauge. The pressure difference was measured by two absolute pressure gauges with different pressure ranges, MKS Baratron Type 627 B, attached to the manifold system. The measuring range of the full scale 100 Torr gauge was 0 to 100 Torr, with the increment of 0.01 Torr; for the full scale 2 Torr gauge the measuring range was 0 to 2 Torr, with the increment of 0.0001 Torr, both gauges have accuracies of 0.12 % of reading and kept at 45 ℃. The ion gauge was a Type 580 Nude Ionization Gauge Tube supplied by Varian and was controlled by a National Research Corporation Type 720 power supply.

The 2.75 inch CF using Cu gaskets were used to connect major components of the system, and the Al sample can (see Figure 3.3) which will be later mounted to the neutron scattering facilities was attached to the system by KF flange and VCR fitting. The ultra high purity hydrogen bottles were supplied by S. J. Smith.

The experiment started at a vacuum condition of 3×10^{-7} Torr or better before

introducing the hydrogen gas, with the valve 2 and 3 closed while the valve 1, 4, 5 opened, the illustration diagram are shown in Figure 3.1. Only parts of the manifold system were exposed to the hydrogen, in this case, is when valve 1, 2 and 3 were closed. The polycrystal Pd sample were isolated by closing valve 5 before conducting the cycling process of exposing to hydrogen at elevated temperature around 74 ℃ to increase the hydrogen absorption rate.

Deformation degree of the sample--- Enhancement Ratio Experiment

In this experiment, the solubility enhancement ratio (ER) was used as an indication of deformation degree of the sample, which is defined by the ratio of C_{tot} to C_b, large enhancement ratio implies densely dislocation density [7]. C_{tot} is the total hydrogen concentration absorbed by the sample; C_b is the bulk concentration. The accumulated pressure difference during the cycling processes Δp could be converted to the C_{tot} through Equation 3.1.2; while the C_b could be derived from Equation 3.1.1 by substituting the P_{H_2}, the equilibrium hydrogen pressure.

$$logC_H = \frac{1}{2} logP_{H_2} + A + \frac{B}{T} \qquad (3.1.1)$$

Where

P_{H_2} represents the equilibrium hydrogen pressure, with units of Pa;

A equals to -5.3;

B equals to 510 K, applied the Sievert's law constants for Pd [6];

T the experiment was conducted at 295 K.

For the enhancement ratio experiment, the theoretical amount of total hydrogen absorption (ΔP_{tot}) was calculated by the ideal gas law, under the assumption of reaching hydrogen concentration of 0.001[H]/[Pd], ΔP_{tot} equals to 8.423 Torr, the ideal gas law equation was shown below in Equation 3.1.2.

$$\Delta P_{tot} = \left(\frac{1}{2}\right) C_{tot} n_{Pd} \frac{T}{V} R \qquad (3.1.2)$$

Where

ΔP_{tot} represents the total amount of hydrogen absorption, with units of Torr;

C_{tot} represents the hydrogen concentration, with units of [mole of H]/[mole of Pd];

n_{Pd} represents the mole number of Pd, with units of mole;

T represents the experimental temperature, with units of K;

V represents the exposure volume to the hydrogen gas, with units of cm^3;

R represents the ideal gas constant, with units of $erg / K \cdot mole$.

In order to reach the required hydrogen concentration, 0.001[H]/[Pd], we conducted the hydrogen exposure experiment twice, first with less amount of hydrogen than the estimated value, which equals to 6 Torr of hydrogen, then exposed to 3.64 Torr of hydrogen the second time. The hydrogen pressure is controlled by the valve manually, therefore would lead to slightly different amount of exposure with the expected value. In this study the ER was measured after the experiment to recreate the deformation of the sample, slightly higher of hydrogen absorption will not affect the results of the experiment. The total hydrogen absorption (ΔP_{tot}) was 9.64 Torr, after applying the conversion equation in Equation 3.1.2, C_{tot} equals to 1.14×10^{-3} mTorr. Therefore, with the equilibrium hydrogen pressure of the experiment equals to 11.4 mTorr, and C_b

corresponds to 3.3×10^{-4} mTorr. The derived enhancement ratio is 3.5.

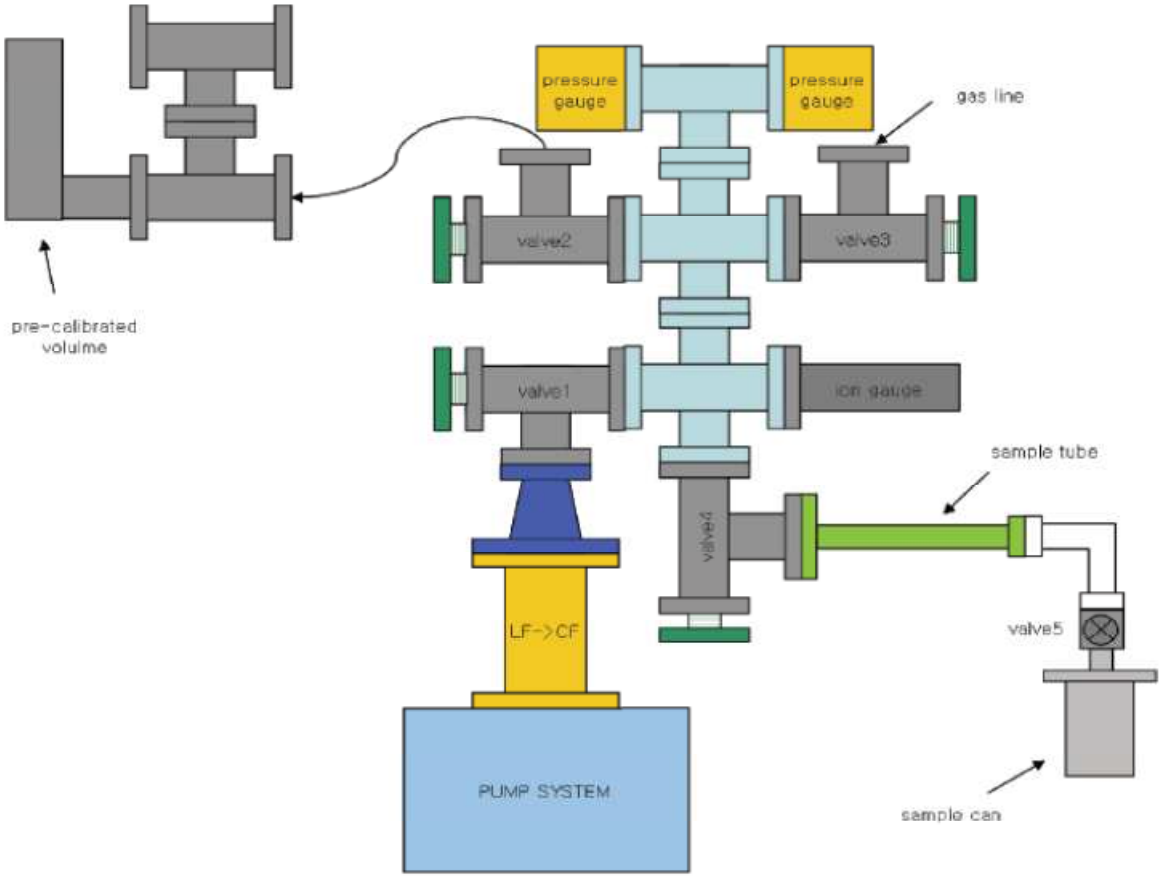

Figure 3.1: Schematic diagram of gas loading system [3].

3.2 Incoherent Inelastic Neutron Scattering Instrument and Procedures

3.2.1 Wide Angular-Range Chopper Spectrometer

One of the advantages of using IINS is it provides the information of vibrational density of states of the hydrogen trapped in Pd dislocations. The theoretical part has been discussed in Chapter 1.5. This chapter will focus on introducing the principle facts for the neutron scattering instrument being used in the experiment. The ARCS (Wide Angular-Range Chopper Spectrometer) at the SNS at ORNL, was used in this experiment to study the $PdH_{0.0011}$. Figure 3.2 shows the schematic diagram of the ARCS at SNS, ORNL [1].

The Spallation Neuton Source (SNS) operated at a frequency of 60 Hz. ARCS views a decoupled ambient poisoned water via neutron guide. The prompt radiation source is blocked by an inserted T_0 chopper. ARCS is a direct geometry time-of-flight (TOF) chopper instrument, which measures the difference of velocity or energy in a given path length by using two Fermi choppers to monochromate the incident neutron energy. The Fermi choppers rotate at speeds up to 600 Hz covering an incident energy from 15-1500 meV [1]. The phase of the chopper relative to the incident neutron pulse defines the incident energy while the final energy of neutrons after interaction is determined by the time of flight. If the total flight path distance between the source and

detector via the sample is L, then the wavelength is given by Equation 3.2.1.

$$\lambda = ht / m_n L \qquad (3.2.1)$$

with h is the Plank's constant, m_n is the mass of the neutron and t is the time of flight [9]. The conversion from the wavelength to the momentum applies the equation of momentum, p, of the neutron,

$$p = m_n v = \frac{hk}{2\pi} = \hbar k \qquad (3.2.2)$$

with $k = 2\pi / \lambda$ is the wavevector. The energy resolution based on the full width at half maximum (FWHM) of elastic scattering peaks varies from 3 to 5 % of the incident energy. A cylindrical array of 115 modules or packs of eight 1 m long ^{3}He linear position sensitive detectors is installed within the detector vacuum chamber [2], the coverage detecting angle ranges from -28 to 135 ° horizontally and -27 to 26 ° vertically. The solid angle (ΔΩ) covered by ARCS detector array is 2.5 sr. The neutron wave transfer vector (Q) is determined by the equation below

$$|Q| = \overrightarrow{k_f} - \overrightarrow{k_i} \qquad (3.2.3)$$

with $\overrightarrow{k_f}$ represents the final wave vector after interaction with neutron, $\overrightarrow{k_i}$ represents the initial wave vector.

3.2.2 Experimental Setup

Deformed polycrystal Pd samples of 174.76 g was loaded with the hydrogen concentration of 1100 appm [H]/[Pd] and placed in the Al sample can which is shown

in Figure 3.33 [3]. After the hydrogen absorption treatment, the Al sample can was isolated by the valve to minimize the disturbance of hydrogen concentration.

The incident energy of 250 meV was selected to optimize the neutron flux and cover the energy transfer range up to second order harmonic oscillation energy of hydrogen. The energy resolution improves with E, the energy transfer (ΔE) is most reliable within about 0.8 of the incident energy. A top loading Closed Cycle Refrigerators (CCR) was used for IINS measurement at 5 K and 300 K. The 5 K experiment was conducted first, followed by the 300 K. Each experiment was run for 18 hours before removing from the apparatus to outgas the sample. The outgassed procedure was conducted at 100 ℃ under vacuum for 9 hours then cooled to room temperature. The outgassed sample provides background subtraction. This direct subtraction step involves the assumption that the presence of hydrogen will not significantly change the IINS from palladium, as the concentration of hydrogen was a few atomic percent only [10]. The outgassed IINS measurement ran for 18 hours on 5 K and 300 K.

The ARCS uses the SNS data acquisition system, and the intensities measured at different angles and time-of-flight *t* will later converted to wave vector Q and energy loss E, I(Q,E). The conversion was using the binning routine since the data were collected based on the recording of detector pixels and time-of-flight of each detected

neutron on an event basis. The incoming neutron flux also corrected for different detector efficiencies [11].

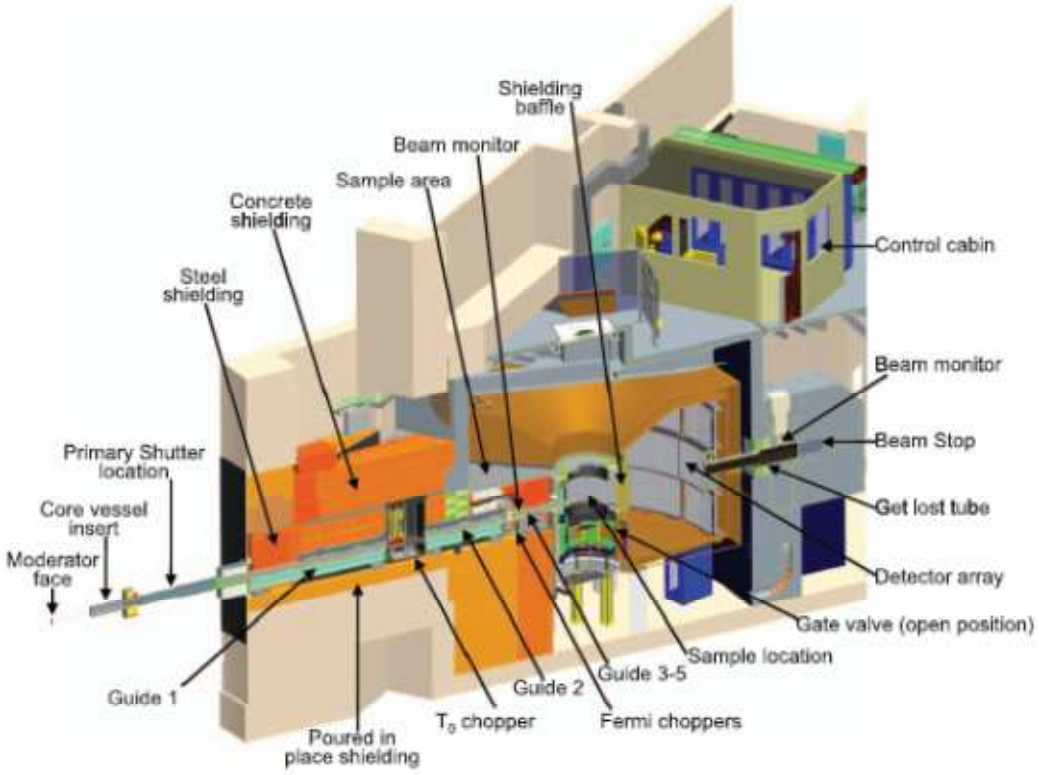

Figure 3.2: Schematic diagram of Wide Angular-Range Chopper Spectrometer [1]. Detailed description of each component is listed in Reference [1].

(a)

(b)

Figure 3.3: The picture of Al can, which served as the sample holder during hydrogen exposure experiment and attached to the ARCS facilities in IINS measurement. (a) the side view and (b) the cross section of the Al can.

CHAPTER 4: INCOHERENT INELASTIC NEUTRON SCATTERING

4.1 Introduction

This chapter presents the results of the IINS experimental measurements, including (1) the subtraction software, DAVE, and subtraction methods, which could be further categorized as the subtraction of with and without hydrogen data, the free recoil subtraction, and the background subtraction. (2) The analysis of corrected IINS spectra at 5 K and (3) the analysis of corrected IINS spectra at 300 K.

4.2 Subtraction Methods

4.2.1 DAVE (Data Analysis and Visualization Environment)

The IINS experimental data was first analyzed using software named DAVE (Data Analysis and Visualization Environment) developed by NIST. Figure 4.1 shows the snapshot of the software DAVE and one of its component called Mslice which is used for IINS data analysis. This software was developed to provide users a quick method to reduce, visualize and interpret the neutron scattering data. More detail description of the software could be referred to reference 11.

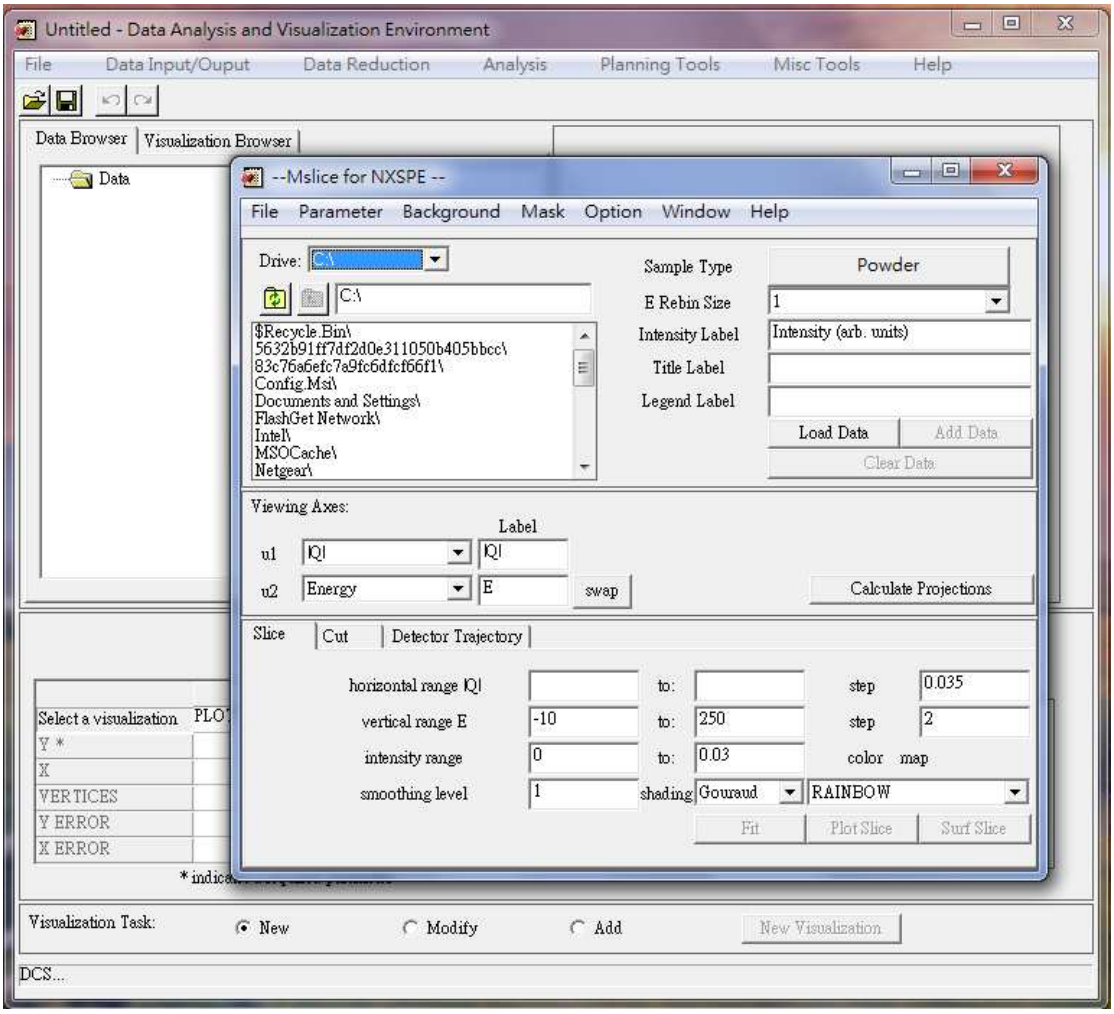

Figure 4.1: The snapshot of software DAVE and the Mslice program used for analyzing IINS neutron scattering data.

4.2.2 The Foreground and Background Subtraction

The VDOS measured at ARCS has two IINS spectra for each temperature, 5 K and 300 K in this case. The normalization process was conducted by correcting different detector efficiencies using a vanadium sample and by normalizing to total or integrated on-target current.

The two dimensional spectrum for energy transfer versus the wave vector transfer are shown in Figure 4.2 and Figure 4.3. Under the intensity scale of 0.3, the inelastic peaks are barely recognizable due to the domination of elastic peaks, also the elastic intensity are less obvious in the 300 K measurement at this intensity scale due to Debye-Waller broadening and multi-phonon events. The two dimensional spectra with intensity up to 0.03 are presented in Figure 4.4 and Figure 4.5 to show the inelastic intensity. The first and second peak along with the free recoil intensity and the acoustic mode of Pd were labeled on the figures.

Figure 4.6 and Figure 4.7 show the comparison of the IINS spectra of $PdH_{0.0011}$ and outgassed Pd at two temperatures. These are integration of two dimensional spectrum over the Q domain over constant energy, with energy step as 2 meV. The data were both normalized by scaling the energy peak at 36 meV (Al peak intensity) to 1. The net data is the subtraction of the outgassed data (background) from the with-hydrogen (foreground); it provides a direct information for the vibration of hydrogen

atoms in Pd lattice. Figure 4.8 and Figure 4.9 are the net IINS data for 5 K and 300 K respectively. These two figures show the measurement of H trapped in Pd before any subtraction. The slopping backgrounds in these two figures are assumed to be due to the proton recoil intensity. Further subtraction methods are presented later in this chapter to exclude the influence from possible variance of hydrogen intensity between the changes of temperature and the excitation of free recoil protons by incident neutron.

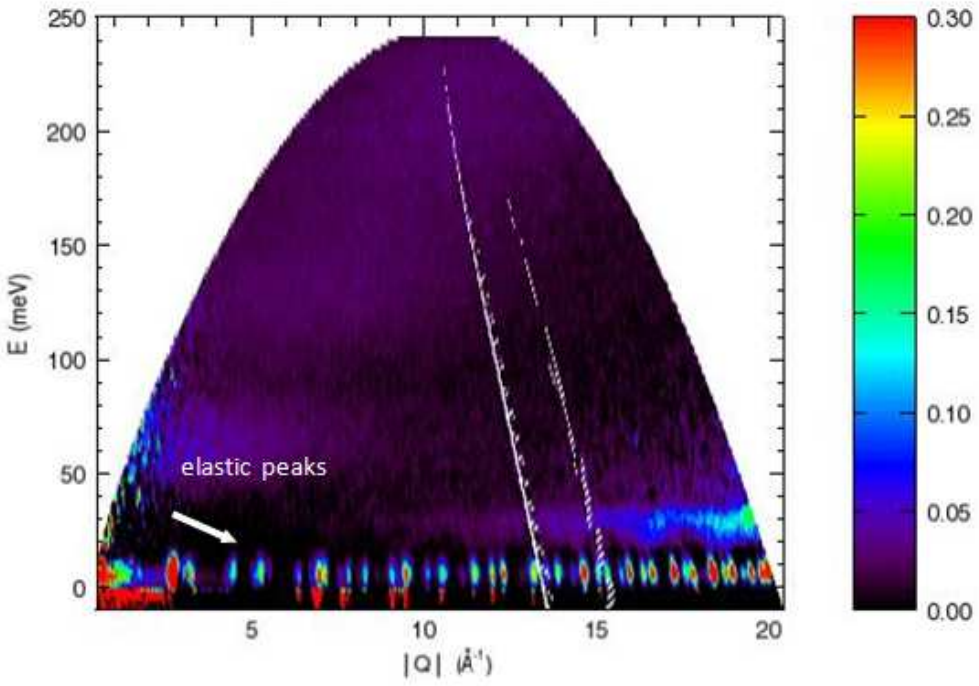

Figure 4.2: Two dimensional net spectrum in energy transfer (E) versus wave vector transfer (Q) at 5 K, with intensity up to 0.3. The white line across the spectrum is due to malfunctioning detectors.

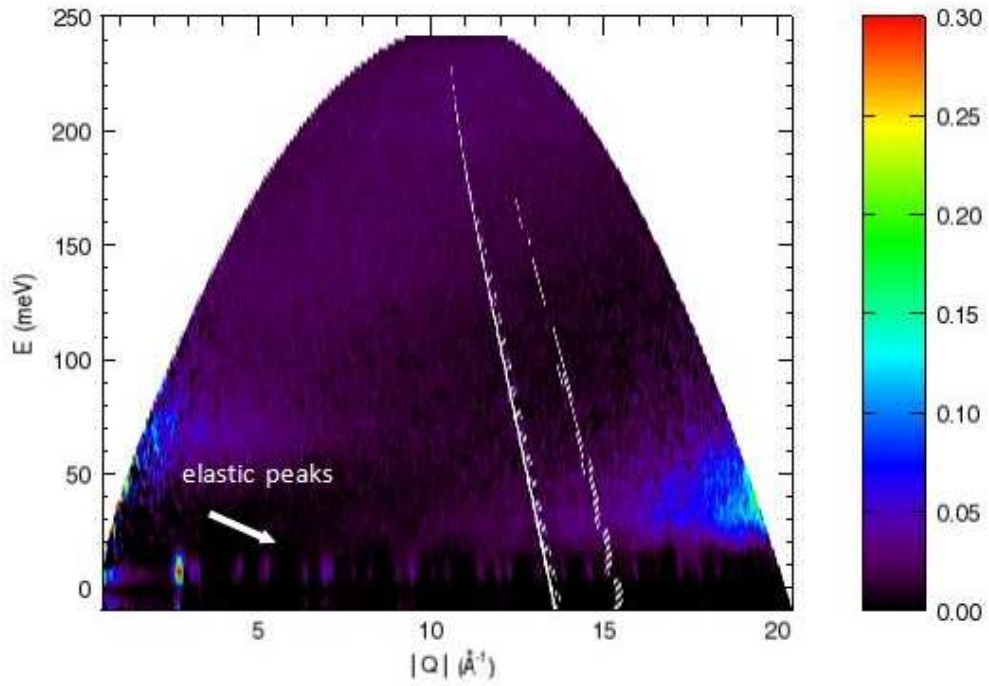

Figure 4.3: Two dimensional net spectrum in energy transfer (E) versus wave vector transfer (Q) at 300 K, with intensity up to 0.3. The white line across the spectrum is due to malfunctioning detectors.

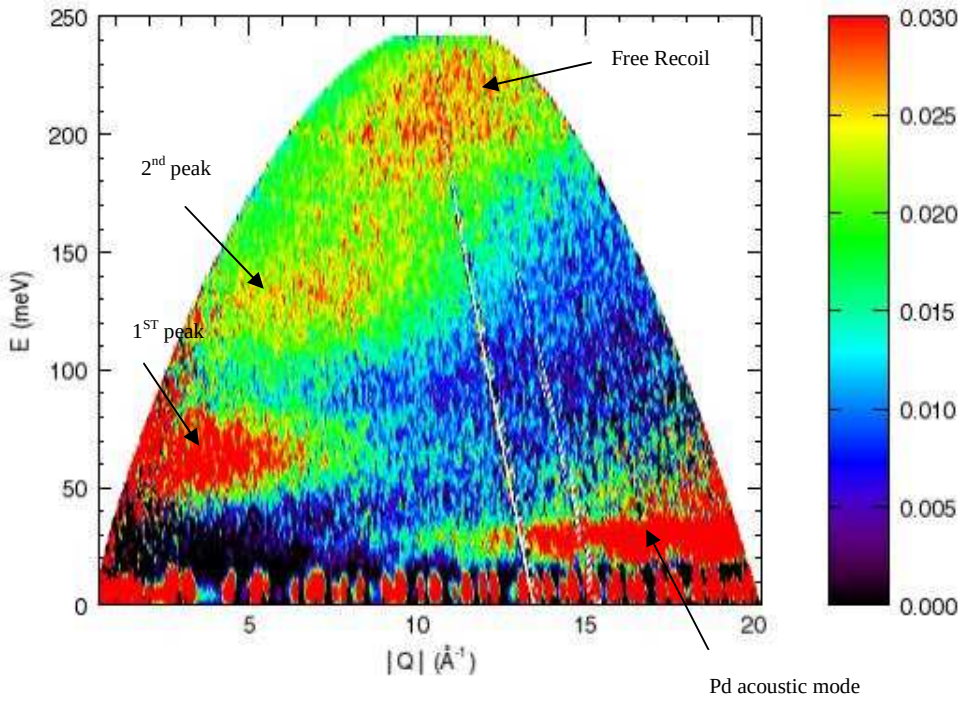

Figure 4.4: 5 K Normalized 2D net specturm in energy transfer versus neutron wave vector transfer (E v.s Q) with the intensity up to 0.03.

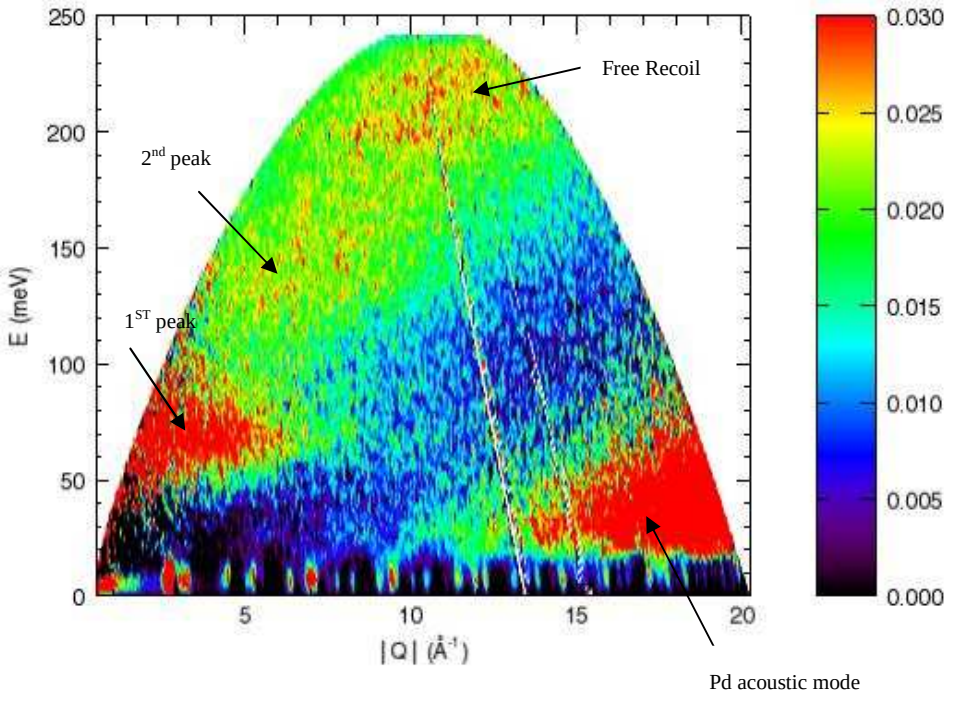

Figure 4.5: 300 K Normalized 2D net spectrum in energy transfer versus neutron wave vector transfer (E v.s Q) with the intensity up to 0.03.

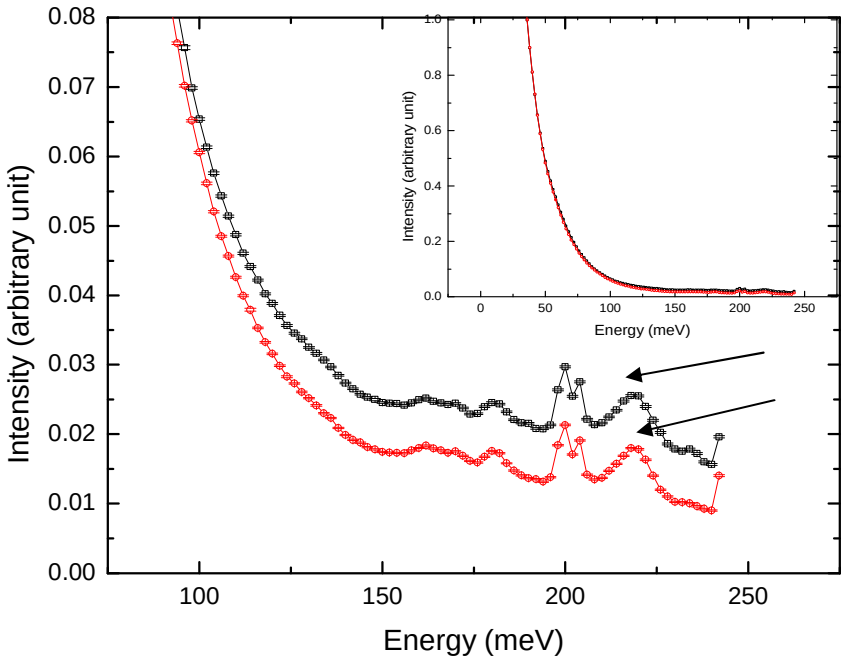

Figure 4.6: 5 K IINS spectra of $PdH_{0.0011}$ (black) and outgassed Pd (red) at two different scales, the arrow bars point to the intensity cased by background influence.

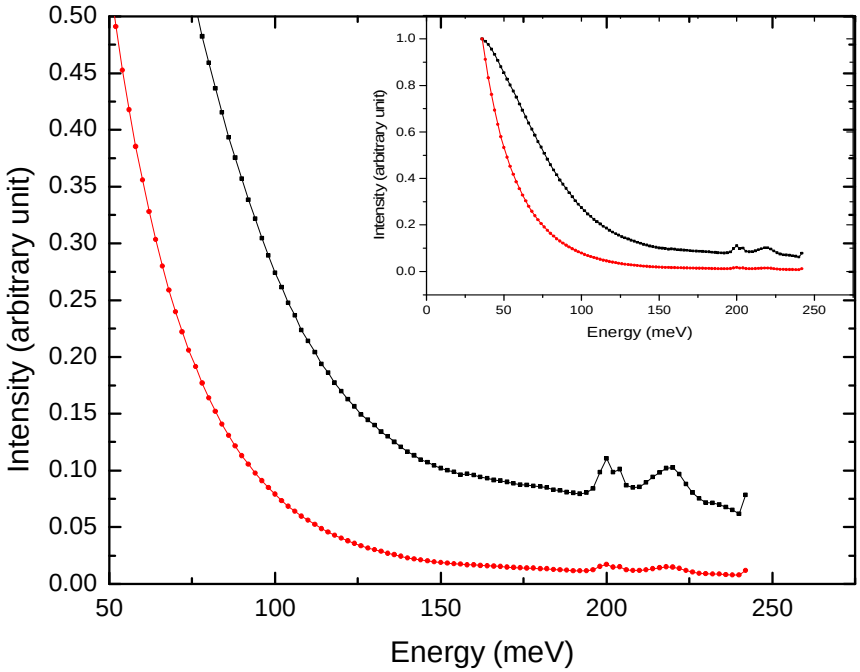

Figure 4.7: 300 K IINS spectra of $PdH_{0.0011}$ (black) and outgassed Pd (red) at two different scales.

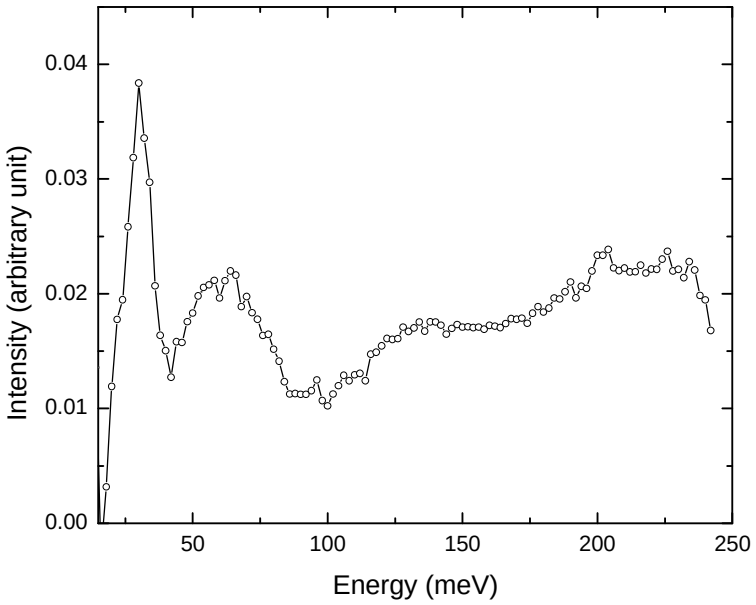

Figure 4.8: Net 5 K IINS spectrum of $_{PdH0.0011}$, the elastic peak at E= 0 meV was cut off to show the feature of inelastic peaks.

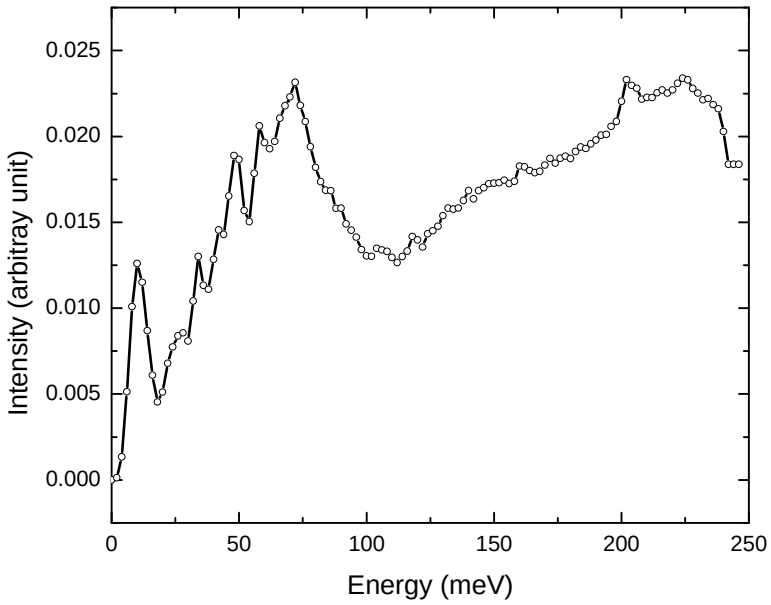

Figure 4.9: Net 300 K IINS spectrum of $_{PdH0.0011}$ at Q from [1-17] $Å^{-1}$ to exclude the high Q noise signal.

4.2.3 Free Recoil Neutron Subtraction Method

Chapter 1.6 explains the theoretical background relevant to our experimental, and the literature review of previous recoil experiments is addressed in Chapter 2.4. This subchapter presents how the free recoil neutron subtraction method works.

In general, the subtraction method is performed by fitting the data to a Gaussian peak. However, none of the previous research applied the free recoil neutron subtraction method to study the second order harmonic peaks. The purpose of this analysis technique is to utilize the two dimensional (E v.s Q) dataset to remove the proton recoiling intensity.

In order to subtract the recoil intensity, the first step is to identify where the intensity was affected the most. Based on the two dimensional plots for the 5 K and the 300 K, see Figure 4.4 and Figure 4.5, the high intensity band between 150 to 250 meV (in light green color) is due to the recoil intensity.

A similar recoiling molecule experiment conducted by Fillaux *et al* [35], which mentioned at Chapter 1.6 free recoil theory, shows a similar band across the two dimentional spectrum, and provides us a way to measure the effective mass for the recoil protons.

The method begins with the choice of wave vector transfer step (ΔQ). The ΔQ is 0.6 ($1/\text{Å}$) for both temperatures, and each region were overlapped with 0.2 ($1/\text{Å}$). For

the 5 K, 170-250 meV was chosen as the energy range and the wave vector transfer region started from 8.4-12.4 ($1/\text{Å}$) for better statistics. For the 300 K, 160-250 meV was chosen with 8-12.4 ($1/\text{Å}$) as the wave vector transfer region. Both of the data was plotted in intensity vs. energy then fitted with the Gaussian function. The fitting equation was presented at below

$$y = y_o + A \cdot \exp[-\frac{(E - E_R)^2}{2w^2}] \qquad (4.2.1)$$

with $2w = FWHM/sqrt(ln\,4)$ and

$$w = \sigma_p \hbar Q_{mean}/M \qquad (4.2.2)$$

$$A = \frac{M}{\hbar Q_{mean} \sigma_p (2\pi)^{1/2}} \qquad (4.2.3)$$

Equation 4.2.2 and 4.2.3 connect the fitting of Equation 4.2.1 with Equation 2.3.1. The only difference is replacing Q in Equation 2.3.1 with Q_{mean}, which is the average number of the fitting Q region. The replacement was done because of ΔQ is not a fix number but a region, and in order to substitute in Equation 2.3.1, the Q dependency has to be excluded before considering the influence of each pixel related Q. The representative fitting plots for two temperatures are shown in Appendix A along with the fitting results for each Q region. The important average fitting parameters are listed in Table 4.

The effective mass *M* was derived from the recoil energy equation $E_R = \hbar\omega_R = \hbar^2 Q^2/2M$, and the number of σ_p is derived by substituting the derived *M*. The first

average number was calculated by excluding the edge dataset and the data with reduced chi-square number smaller than 50%. The statistics were calculated based on the dataset left and using the 90% confidence level for 5 K, 95% confidence level for 300 K to exclude far off data and achieve the final average number. The difference in the confidence level is mainly because of the different divergence degree for two temperatures; 300 K dataset has larger divergence and has fewer data after the first step exclusion, the confidence level was chosen in order to maintain enough statistic data base.

Table 4: The average fitting parameters for 5 K and 300 K.

Temperature (K)	w (meV)	E_R(meV)	AQ_{mean}	M (amu)	σ_p’
5	20.74	208.40	0.0826	1.10	1.97
300	23.62	207.00	0.0872	1.12	2.28

The Q_{mean} represents the medium wave vector transfer in the chosen region, and the $\sigma_p' = \sigma_p * \hbar/M$ in Equation 2.3.1. The number was round up to the second decimal point.

With the fitting parameters, the net data was exported to MATLAB to conduct the recoil subtraction based on each pixel. The code was attached in the Appendix B. The derived recoil intensity was calculated for each pixel in 2-D plot,

$$I_R^{ij} = A \cdot Q_{mean} \left(\frac{1}{Q^{ij}}\right) \exp\left[\frac{-(E^{ij} - E_R)^2}{2(\sigma_p' Q^{ij})^2}\right] \qquad (4.2.4)$$

The derivation of Equation 4.2.4 is based on the dynamic structure factor in Equation 2.3.1 which was used to fit the recoil intensity. The parameter of $\sigma_p' = \sigma_p * \hbar/M$ in

Equation 2.3.1, with σ_p from the Gaussian fitting and M derived from the recoil energy equation $E_R = \hbar\omega_R = \hbar^2 Q^2/2M$. The Q_{mean} was added to exclude the dependence of wave vector transfer in the fitting process before considered the influence by each wave vector transfer in each pixel.

Recoil Subtraction Code in MATLAB

In order to demonstrate the validity of our coding, the net data calculated by MATLAB was first compared with the one directly exported from DAVE/Mslice; a software developed by NIST to analyze the IINS data, to show the consistency. The results are shown in Figure 4.10 to 4.12. In these figures one could see the curves matched very well, although the region below 50 meV has slightly larger difference, this difference is believed to be due to the binning procedure in Mslice program, which leads to smaller intensity difference after integration and normalization. Besides this small difference at lower energy region, the results were consistent in general and severed as convincing evidence that the MATLAB code we are using in this study is reliable.

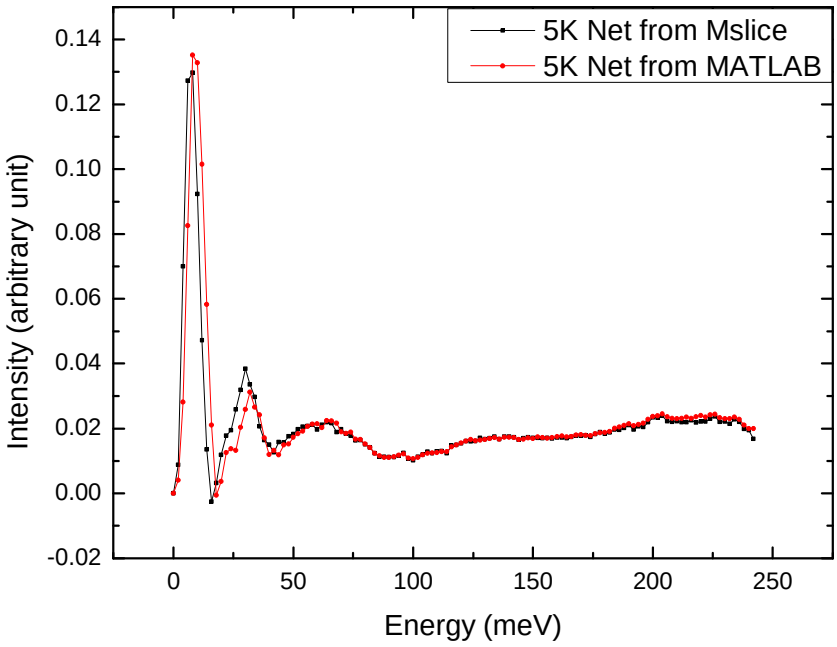

Figure 4.10: The comparison of the 5 K net data exported from Mslice and the one generated from MATLAB code.

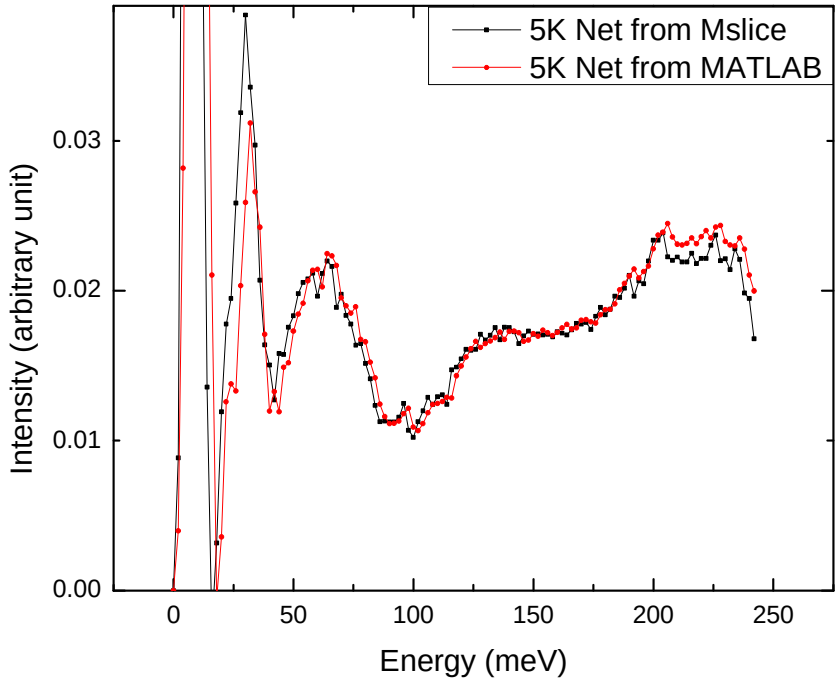

Figure 4.11: A refined scale of Figure 4.10 to present the detail of the two curves.

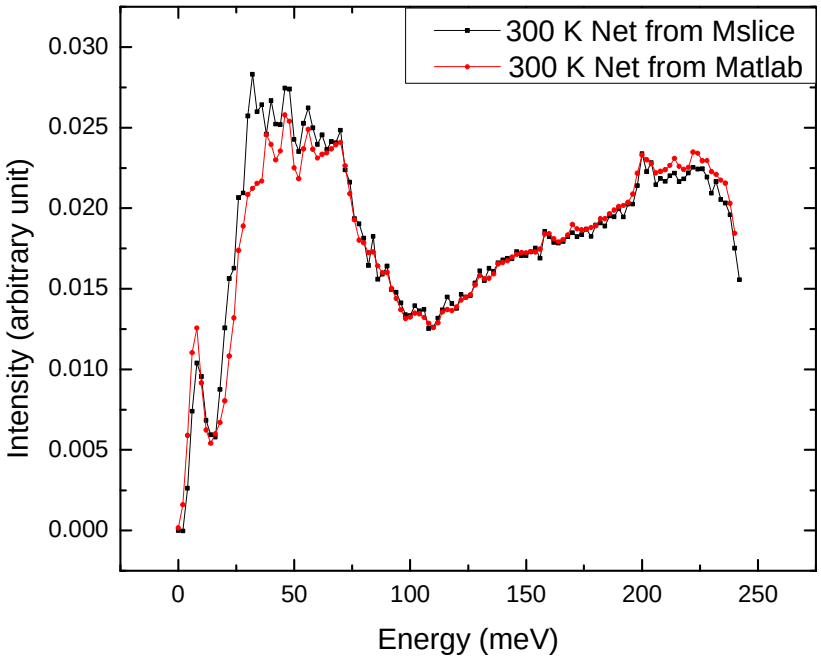

Figure 4.12: The comparison of the 300 K net data exported from Mslice and MATLAB.

By using the fitting parameters in Table 4, the 5 K and 300 K net data and the one with recoil signal subtraction are showed in Figure 4.13 to 4.15. From Figure 14 and Figure 15, the recoil intensity exist mainly above 150 meV, which is reasonable according to our free recoil theory in Chapter 1.6, with ΔE proportional to Q^2. From these two figures, the intensity difference between net data and with recoil signal subtraction is significant. However, the recoil subtraction mainly works on the higher energy transfer region, and could not exclude the slopping background at 1st harmonic peaks. The 2nd harmonic peak for 5 K data after subtraction still presents a certain degree of sloping background; while the 300 K has almost no such phenomena. Additional

background subtraction would be performed to eliminate the influence of slopping background. The representative background subtraction (dash line A, B, C, D) are shown in Figure 4.14 and Figure 4.15, which has Q range as 0-20 $Å^{-1}$. But in order to exclude the acoustic mode of Pd shown in Figure 4.4 and Figure 4.5, in the further research, the first harmonic peak Q range was limited to 1-10 $Å^{-1}$.

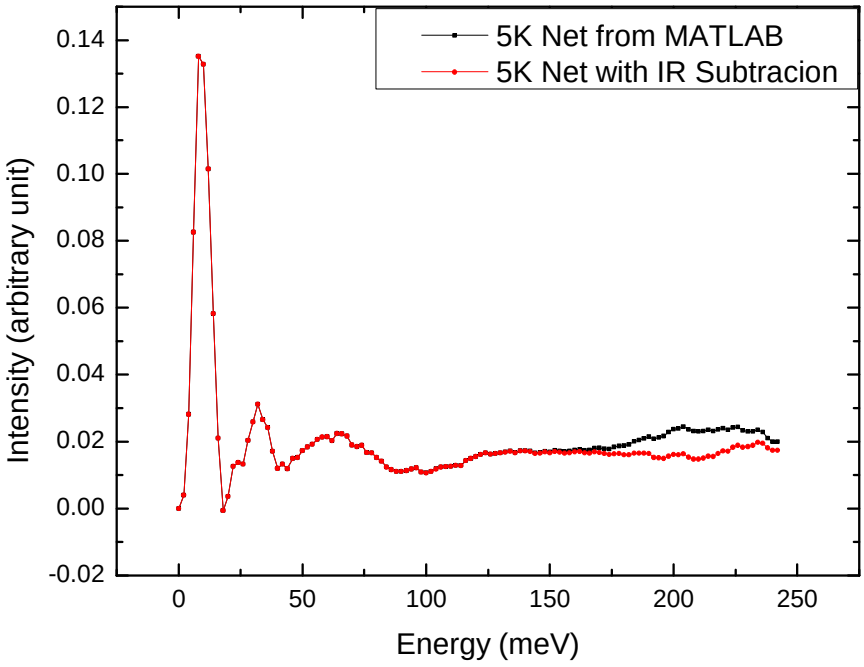

Figure 4.13: The 5 K net data and the same data with the recoil intensity subtraction, the IR Subtraction stands for recoil intensity subtraction.

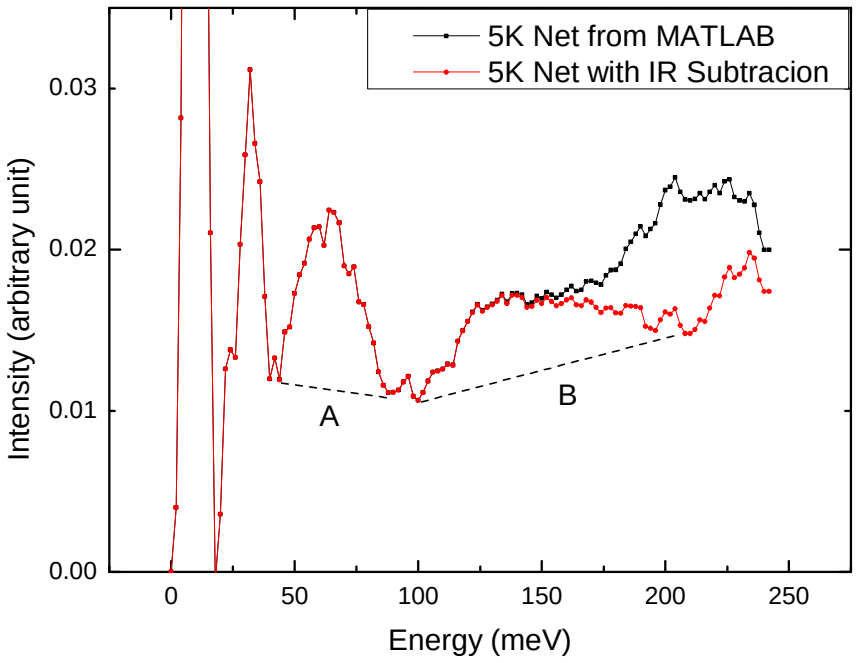

Figure 4.14: A refined scale of Figure 4.13. The recoil signal subtraction started from 150 meV and showed an obvious peak before the sloping background subtraction, the IR Subtraction stands for recoil intensity subtraction, dash line A and B are the background subtraction intensity. With Q range is 0-20 $Å^{-1}$.

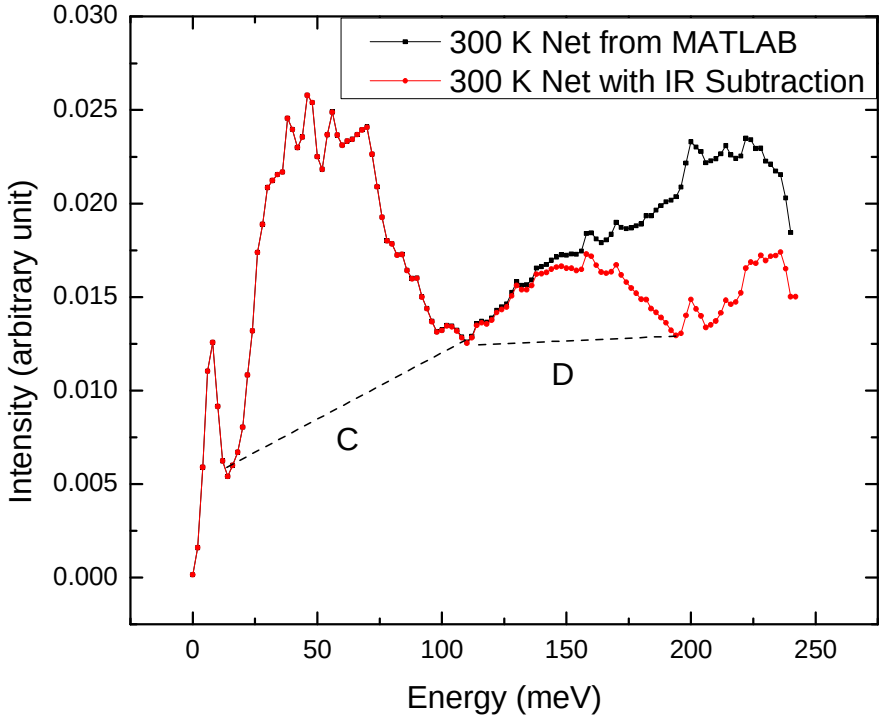

Figure 4.15: The 300 K net data and the same data with the recoil intensity subtraction, the IR Subtraction stands for recoil intensity subtraction, dash line C and D are the background subtraction intensity. With Q range is 0-20 $Å^{-1}$.

4.2.4 Background Subtraction

The main purpose of linear background subtraction is to exclude the signals due to background, although the mechanism is not fully studied yet, one possible explanation is that the assumption of the insertion hydrogen atoms will not interfere with the palladium atom is not completely correct. Nevertheless, the base line for linear background subtractions is presented in Figure 4.16 to 19, this are the one that being used and lead to final results.

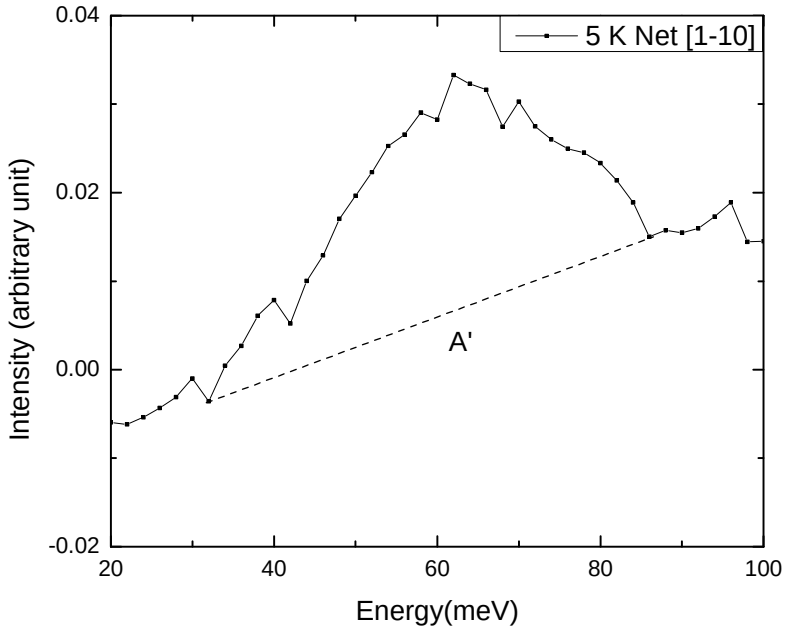

Figure 4.16: The base line of first harmonic peak in background subtraction method at 5 K Net data with wave vector transfer ranges from 1 to 10 $Å^{-1}$. The dash line A' corresponding to A in Figure 4.14 but with a refined Q region.

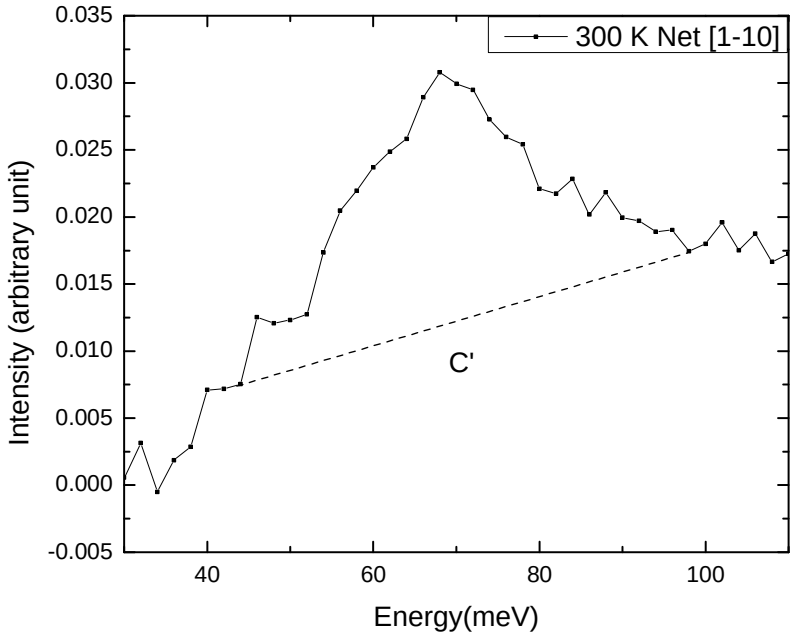

Figure 4.17: The base line of first harmonic peak in background subtraction method at 300 K Net data with wave vector transfer ranges from 1 to 10 $Å^{-1}$. The dash line C' corresponding to C in Figure 4.15 but with a refined Q region.

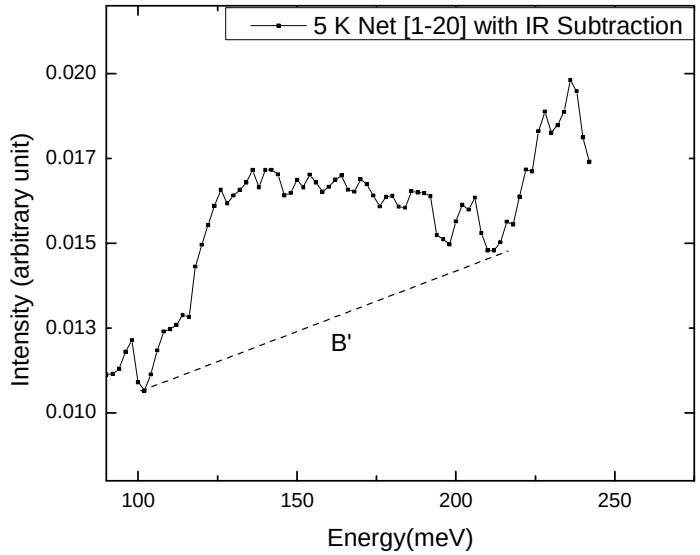

Figure 4.18: The base line of higher energy peak with recoil subtraction in background subtraction method at 5 K net data with wave vector transfer ranges from 1 to 20 $Å^{-1}$, IR Subtraction means the recoil intensity subtraction. The dash line B' corresponding to B in Figure 4.14 but with a refined Q region.

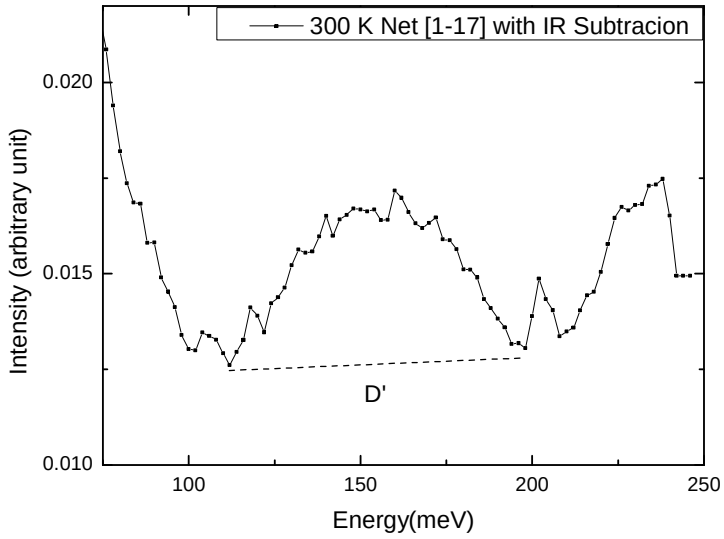

Figure 4.19: The base line of higher energy peak with recoil subtraction in background subtraction method at 300 K Net data with wave vector transfer ranges from 1 to 17 $Å^{-1}$, IR Subtraction means the recoil intensity subtraction. The dash line D' corresponding to D in Figure 4.15 but with a refined Q region.

The background subtractions for first and second harmonic peak at two temperatures are presented separately due to the different Q range chosen. The dash line (A' , B', C', D') in Figure 4.16-19 are similar illustration just like the line in Figure 4.14 and 4.15, but with a different Q range for the primary peak to exclude the Pd acoustic mode. The primary peak was limited to 1-10 $Å^{-1}$ for both temperatures, while the 2nd peak has 1-20 $Å^{-1}$ for 5 K, 1-17 $Å^{-1}$ for 300 K measurements. The final results after background subtraction could be referred to Chapter 4.3 and 4.4. One thing worth points out is that, in Figure 4.18 and Figure 4.19 the peak after 200 meV is attributed to the extra recoil intensity that were not fully excluded, this corresponds to the high intensity region above 200 meV in Figure 4.20 and Figure 4.23.

4.3 Analysis of Corrected IINS Spectra at 5 K

The two dimensional plot after recoil subtraction is presented in Figure 4.20, this should be compared with the net data plot in Figure 4.4, which is without recoil subtraction. From the comparison of these two figures, the most obvious difference is the decreasing of intensity at the supposed region for free recoil signal.

The results of IINS Net data with recoil and background subtraction is presented here along with the Gaussian fitting curves. See Figure 4.21 and Figure 4.22. The fitting results were shown in Table 5 at Chapter 5.1. The primary peak and the higher

energy peak are presented in two figures because of the different Q range chosen. The primary peak was limited at the momentum transfer range (Q) of 1-10 $Å^{-1}$, while the higher energy peak was from 1-20 $Å^{-1}$. The different Q range does not affect the position of the higher energy peak, but by limiting the Q region chosen, the unwanted high intensity bulb due to Pd acoustic mode is avoided. The bulb region in 2-D spectrum, see Figure 4.4, represents the acoustic mode of Pd due to the presence of hydrogen interacts with Pd, and the subtraction of without hydrogen measurement from with hydrogen will not eliminate this interaction intensity.

The comparison of FANS [3] and ARCS data at low temperature are also presented in Figure 4.22. The main purpose of comparing these two curves is to see if there is any correlation of β phase at low temperature. More discussion could be referred to Chapter 5.

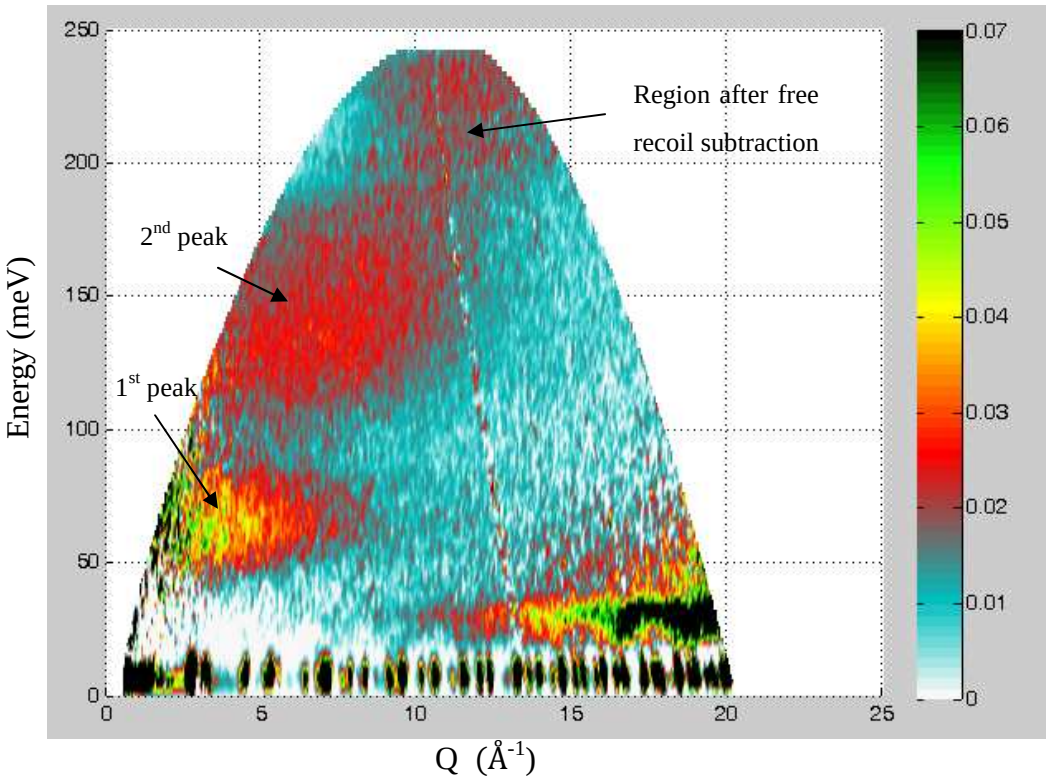

Figure 4.20: Two dimensional IINS net spectrum with recoil subtraction at 5K.

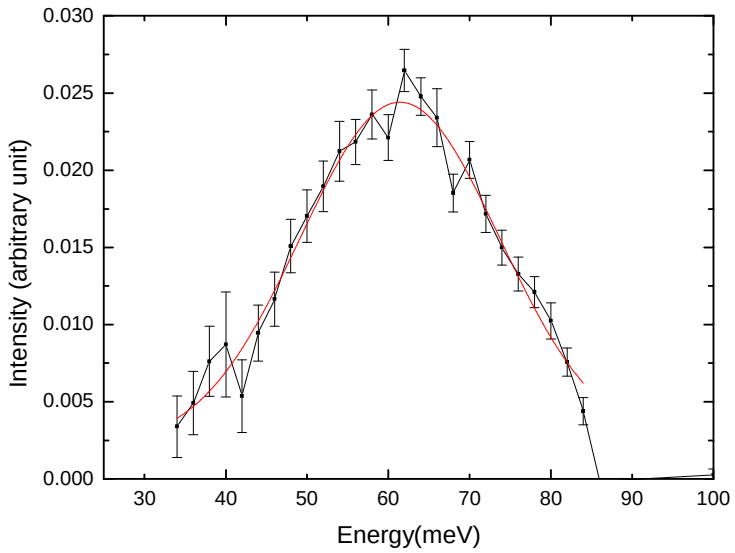

Figure 4.21: 5 K net IINS spectrum at first harmonic peak with background subtraction, the Q range is 1-10 $Å^{-1}$, the smooth curve is the Gaussian fitting with energy peak at 61.4 meV and the fitting results are listed in Table 5, chapter 5.1.

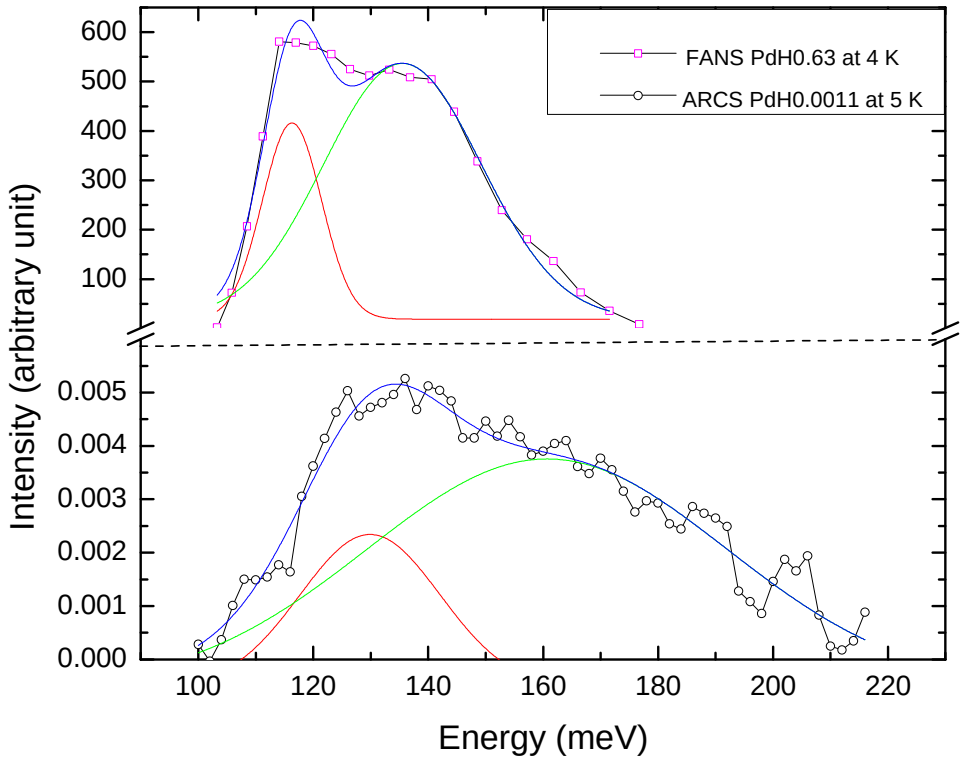

Figure 4.22: The comparison of ARCS and FANS higher energy peak data at low temperature, the smooth curve is the two-Gaussian fitting. (Below)- 5 K net ARCS IINS spectrum at higher energy peak with recoil and background subtraction, the Q range is 1-20 $Å^{-1}$, with energy peak at 129.8 and 160 meV. (Top) - 4 K net FANS IINS spectrum at higher energy peak without recoil subtraction, the energy peak is at 116.3 and 135.5 meV. The fitting results are listed in Table 5, chapter 5.1.

4.4 Analysis of Corrected IINS Spectra at 300 K

The 300 K 2-D net spectrum after recoil subtraction is presented in Figure 4.23. Comparing with the net IINS spectrum in Figure 4.5, the free recoil intensity decreased in Figure 4.23 after recoil subtraction and instead the intensity at second energy peak is more defined.

For the data at 300 K, same method is applied. The first harmonic peak was limited at the momentum transfer range (Q) of 1-10 $Å^{-1}$, while the higher energy peak was from 1-17 $Å^{-1}$, these two peaks are shown in Figure 4.24 and 4.25.

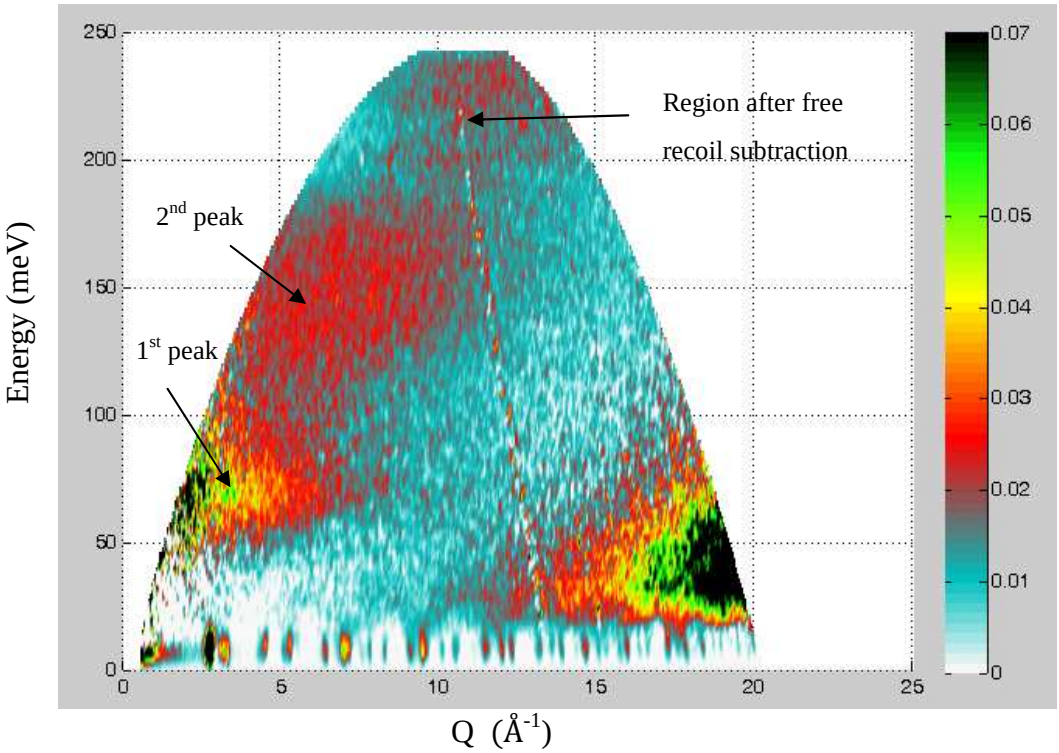

Figure 4.23: Two dimensional IINS net spectrum with recoil subtraction at 300 K.

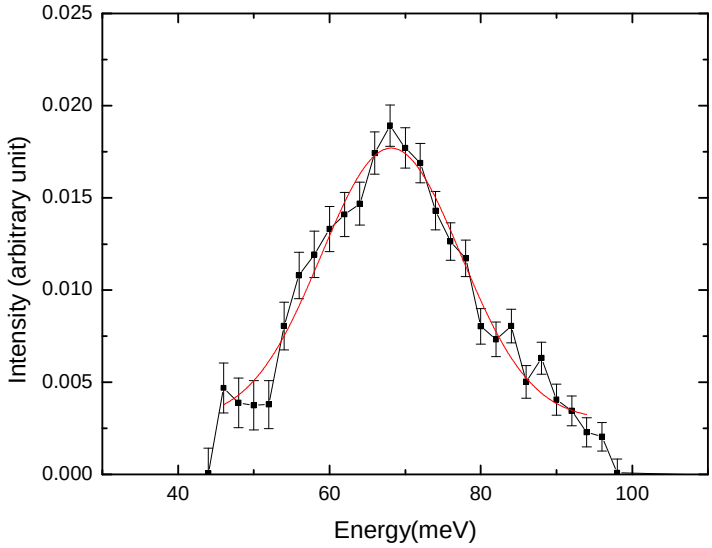

Figure 4.24: 300 K net IINS spectrum at first harmonic peak with recoil and background subtraction, the smooth curve is the two-Gaussian fitting with energy peak at 68.2 meV and the fitting results are listed in Table 5, chapter 5.1.

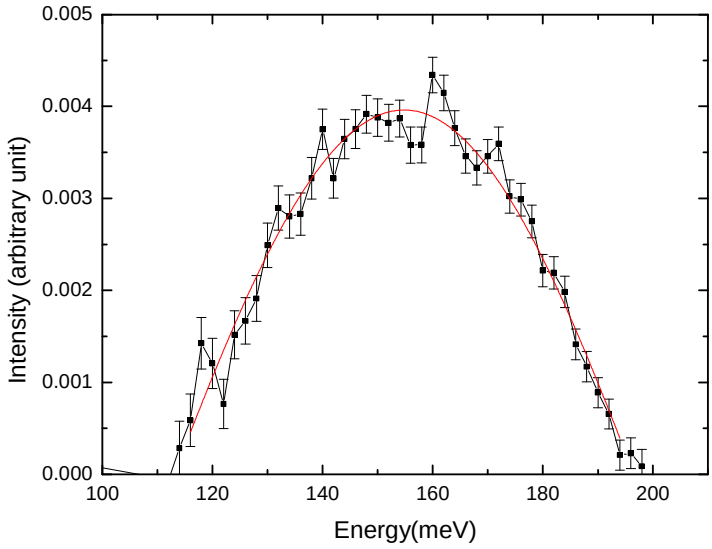

Figure 4.25: 300 K net IINS spectrum at higher energy peak with recoil and background subtraction, the smooth curve is the two-Gaussian fitting with energy peak at 154.8 meV and the fitting results are listed in Table 5, chapter 5.1.

CHAPTER 5: DISCUSSION of RESULTS

This chapter includes the Gaussian fitting results for two temperatures, and compares the peak location using the previous published data with anharmonicity theory. The general fitting results are discussed in the first section, the analysis for the primary/first harmonic peak are discussed in the second section, the second harmonic peak at 300 K are addressed in the third section, the multiple phonons at 5 K are explained in the forth section, the 2-D IINS spectra with fitting results of mass and energy of recoil particle are explained in the fifth section and concluded with other features of the measurement.

Fitting Results for Two Temperature

The two temperatures fitting results of net $PdH_{0.0011}$ with recoil and background subtraction is recorded in Table 5, the individual VDOS spectrum and the Gaussian fitting can be found in Figure 4.21-22 and Figure 4.24-25 at Chapter 4.3 and 4.4 for 5 K and 300 K separately. The relation between first and second order peak is also shown in Table 5. If the energy of second peak is twice the energy of first peak then the atom vibrations is pure harmonic. The extra energy difference is attributed to the anharmonic phenomenon in potential energy; in this case the positive anharmonicy

parameter indicates a well-like shape for the local potential energy. The experimental data is compared with the published data to verify the peak location and to prove the approach of taking recoil subtraction can identify the peak position more accurately. For $PdH_{0.0008}$, only the primary peak was measured in the original experiment, the second peak was calculated based on the published anharmonicity parameter; the β phase of $PdH_{0.6\text{-}0.7}$ at 80 K was used for the comparison of 5 K measurement and the α phase of $PdH_{0.014}$ at 295 K was used for the comparison of 300 K measurement.

Table 5: The Gaussian fitting results for net data with recoil and background subtraction, and the published data with anharmonicity parameter calculations.

Sample	Temp. (K)	1st peak (meV)	w (meV)	2nd peak (meV)	w (meV)	3rd peak (meV)	w (meV)	Anharmonicity parameter 2β (meV)	Reference
$PdH_{0.0011}$	5	61.4±0.3	39.5	129.8±1.6	27.2	160.0±7.3	89.8	7.0**	This work
$PdH_{0.0008}$	4	59.0±5.8	---	127.7*	---	---	---	9.7#1	[33]
$PdH_{0.63}$	4	58.6±4.0	---	116.3±0.4	---	135.5±1.4	---	19.2	This work & [3]
$PdH_{0.99}$	15	56.0	---	113.0	---	134.0	---	21	[42]
$PdH_{0.0011}$	300	68.2±0.4	53.7	154.8±0.4	103.9	---	---	18.4	This work
$PdH_{0.0008}$	295	66.0	---	151.0*	---	---	---	19#2	[33]
$PdH_{0.014}$	295	69.0	---	137.0	---	156.0	---	19	[29]

Each peak is in±1σ,

*: Indicates the peak location was calculated based on the published 1st peak location.

**: The anharmonicity parameter term is for the dilute phase, the correct term should be multiphonon effects for hydride.

#1: The anharmonicity parameter is based on the β phase of $PdH_{0.6\text{-}0.7}$ at 80 K.

#2: The anharmonicity parameter is based on the α phase of $PdH_{0.014}$ at 295 K.

First Peak Comparison

The terminology needs some clarification before discussion. Primary peak is used to address the 1st peak at 5 K; while the first harmonic peak is used to addressed the 1st peak at 300 K. The difference in terminology is because the term harmonic is limited to dilute phase, and at 5 K, is not.

The primary peak position at 5 K is 61.4 meV, which is higher than the expected value of 59.0 meV for $PdH_{0.0008}$ β phase at 4 K; while the first harmonic peak at 300 K is located at 68.2 meV, which is 2 meV higher than the $PdH_{0.0008}$ measurement, but comparing with other published data, it matches well with 69.0 meV for the $PdH_{0.014}$ α phase at room temperature, see Table 1. The peak energy at 66 meV is attributed to hydrogen-induced dilatation of the interstitial site in the elastic part of the dislocation strain field [33]; however, it is chosen to perform the anharmonicity calculation for consistency. Figure 5.1 shows the comparison of primary peak for $PdH_{0.0008}$ and $PdH_{0.0011}$ at low temperature, both data have been normalized to the total area below the curve. The similar feature of high energy shoulder is generally attributed to the longitudinal-optic modes of hydrogen atoms [25]. Also, the measurement of $PdH_{0.0011}$ shows a relatively symmetric shape compared with the other two data. It is difficult to determine which main reason leads to the shift of primary peak at 5 K, one possible explanation is that the higher incident neutron energy (250 meV in this experiment

compared with the 130 meV in $PdH_{0.0008}$ measurement) leads to a loss in resolution at lower energy region.

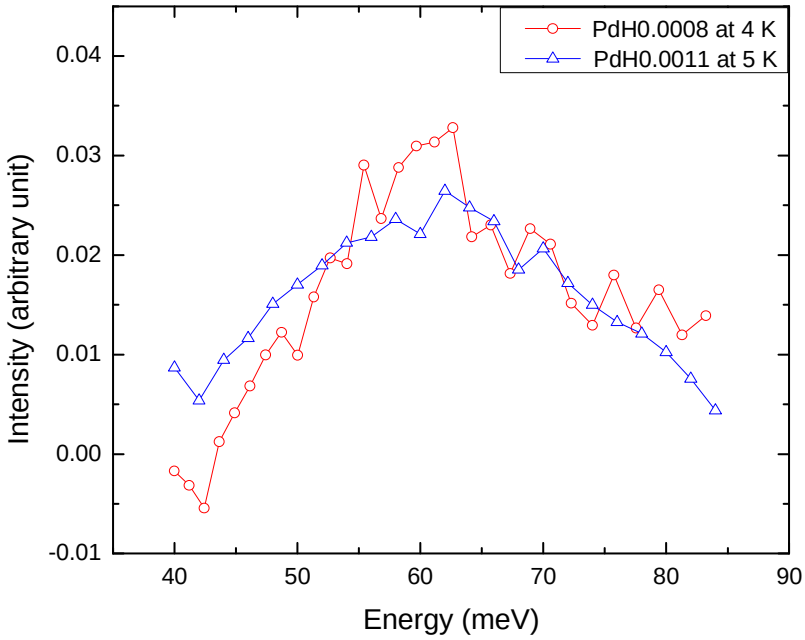

Figure 5.1: The comparison of primary peak for $PdH_{0.0008}$ and $PdH_{0.0011}$ at low temperature, the $PdH_{0.0011}$ has Q range from1-10 $Å^{-1}$. $PdH_{0.0008}$ is measured by Hyunsu Ju, more experimental detail can be found in ref. [3, 33].

The comparison of first harmonic peak for $PdH_{0.0008}$ and $PdH_{0.0011}$ at room temperature is shown at Figure 5.2. A less defined high energy shoulder also presents at the room temperature data. For the 2^{nd} peak at 300 K, see Figure 4.25, it presents a symmetric shape, which is one of the main features that expected to be seen in the IINS higher energy peak, for the harmonic peak should have the shape of symmetry if the noise signal from the background and the environment are excluded. The symmetric shape at 300 K demonstrates this assumption.

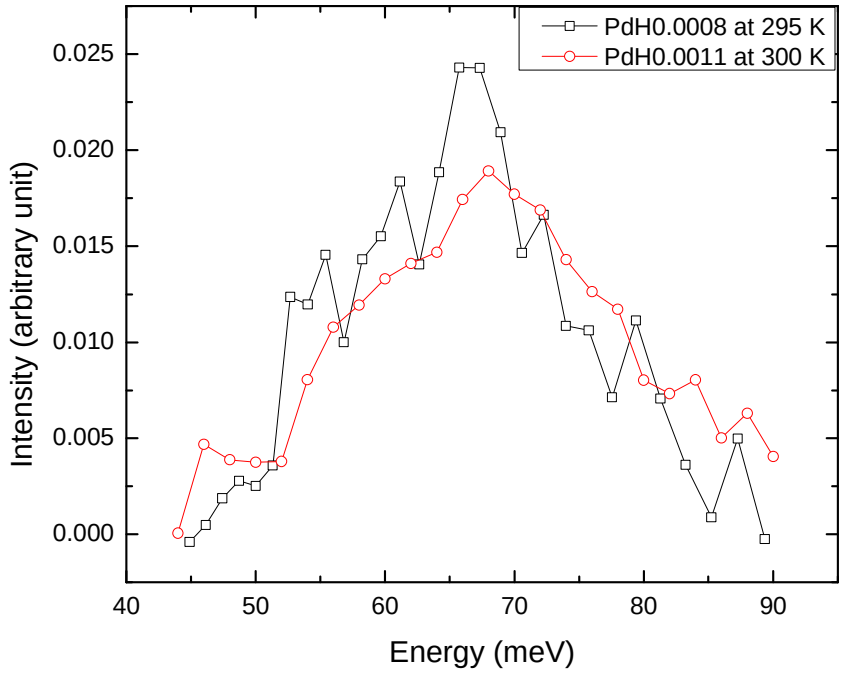

Figure 5.2: The comparison of first harmonic peak for $PdH_{0.63}$, $PdH_{0.0008}$ and $PdH_{0.0011}$ at room temperature. $PdH_{0.0008}$ and $PdH_{0.63}$ are measured by Hyunsu Ju, more experimental detail can be found in ref. [3, 33].

Second Harmonic Peak at 300 K

The term second harmonic peak is used to address the 2nd peak at 300 K. For 5 K, the correct terminology is multiphonon peaks in this research. Based on the anharmonicity calculation, the expected 2nd peak position and experimental data are listed in Table 5. The experimental data shows good correlation with the expected value; with the 2nd peak difference within 4 meV for $PdH_{0.0011}$ and $PdH_{0.0008}$.

The 300 K $PdH_{0.0011}$ measurement is compared with the α phase of $PdH_{0.0008}$

using the anharmonicity parameter derived from $PdH_{0.014}$ at 295 K. Although the measurement was smeared and the peak at 137 meV is unresolved, the anharmonicity parameter from this research is 18.4 meV, which is close to the expected value of 19 meV.

Multiphonon peak at 5 K

The 2nd peak at 5 K has an extra coupling energy peak at 160 meV; which listed as 3rd peak, and this indicates that the higher energy peak at 5 K are not due to a second harmonic, but the result of multiphonon events. Kolesnikov [42] have found a similar shape for higher energy peaks in $PdH_{0.99}$ at 200 K, see Figure 2.2 and bottom curve of Figure 4.22.

The peak location in Kolesnikov' s research is located at 55, 113 and 134 meV for 1st and 2nd and 3rd peak; which are listed in Table 5, the derived anharmonicity parameters equals to 21 meV, which is far from the expected value of 9.7 or 7.0 meV, but close to the 19.2 meV in the $PdH_{0.63}$ 4 K measurement. Not only are the peak locations similar, the shape of multiphonon peaks also are similar.

Comparing the 5 K measurement with the $PdH_{0.63}$ data at 4 K, if there is a one to one corresponding relation, we can assume there is a hardening effect on the 5 K spectrum, leading to a shift to higher energy. The energy difference can also be attributed to the perturbation of the environment compared with trapped hydrogen at 5

K. This will need further confirmation through running a simulation test.

The 2-D Spectra and Mass of Recoil Particle

For the 2-D IINS spectra, the peak intensity difference between with and without recoil subtraction for the original free recoil area and the 2^{nd} energy peak is significant. This could be seen in Figure 4.4 and Figure 4.20 for 5 K, and Figure 4.5 and Figure 4.23 for 300 K. Besides, the free recoil fitting results in Table 4 shows the mass of the recoil particle equals to 1.10 and 1.12 amu for 5 and 300 K respectively, which is close to the true value of hydrogen mass 1.007825 amu, the error is about 9 %. The recoil energy is centered at 208 and 207 meV individually. The intensity shift of the free recoil area and the derived fitting mass indicates that the free recoil signal is from the hydrogen atom. Although further research would be needed to identify if the recoil hydrogen atom is weakly bond in the Pd lattice or has escaped the trapping site and interacts freely with the incident neutrons.

Other Features of the Measurements

In this study, the intensity of each peak is incomparable due to the limitation of integrating over different Q region. However, there are some features of the first harmonic peak that can be more thoroughly addressed. In Figure 5.1, the width for

$PdH_{0.0011}$ is significantly broader than the width of $PdH_{0.0008}$, the loss of degeneracy is account for the broadness due to the distorted dislocation environments and can be further explained why the 5 K experimental data in Table 5 does not match with the one derived by anharmonicity theory. The shifting of first harmonic peak from room temperature to 5 K upon cooling is explained in a previous study by Heuser *et al.*[33] through the theory of phase transformation from α to β phase in the cooling process.

CHAPTER 6: CONCLUSION

The vibrational density of states of hydrogen trapped at dislocations of Pd was measured at 5 and 300 K using ARCS at ORNL, with incident neutron energy of 250 meV over a Q range of 0-20 $Å^{-1}$. The primary objective of this measurement is to study the high energy range by developing a recoil subtraction method to exclude the influence from the free recoil signals and to better locate the peak location. The anharmonicity theory is used in the comparison of the experimental measurement and the calculated data. The conclusion of this study and suggestions for future work is presented below.

(1) The phase transformation of α to β phase was observed in the IINS experiment when cooled from room temperature to 5 K. The phase transformation was confirmed by the correlation between the characteristic peak position and width of our $PdH_{0.0011}$ 5 K measurement (61.4 meV) to the known $PdH_{0.0008}$ β phase at 4 K (59 meV); and our $PdH_{0.0011}$ 300 K measurement (68.2 meV) to the known $PdH_{0.0014}$ α phase at 295 K (69 meV). The correlative peak features indicate a similar environment for H atoms trapped at Pd dislocations. The shifting of our 5 K measurement was attributed to the poor resolution from incident neutron with higher energy.

(2) The comparison of 2-D IINS spectra at free recoil region before and after the free recoil subtraction provides solid evidence for the validity of our recoil subtraction

method. The most evident difference is the decrease of the intensity at the free recoil region compared with the 2nd energy peak area. The feature is shown in both of 5 K and 300 K measurements. The mass of the recoil particle is 1.10 and 1.12 for 5 and 300 K respectively, which shows a 9 % difference. The recoil energy is 208 and 207 meV for two temperatures. The recoil subtraction method was derived from dynamic structure factor $S(Q,E)$ and successfully excluded the recoil signals at higher energy region.

(3) The anharmonicity parameters listed in Table 1 were applied to calculate the expected peak position beyond first harmonic peaks, the results matches well on 300 K measurements.

(4) The higher energy peak at 5 K was identified as a multiphonon peak. The multiphonon VDOS has been simulated in the research of Kolesnikov [42], which has similar feature with the $PdH_{0.63}$ at 4 K measurement. By comparing the the 5 K and $PdH_{0.63}$ data, this work concluded that the 5 K measurement shows a hardening effet in the spectrum and leads to a shift to higher energy. It is worth pointing out that the published anharmonicity parameters used for comparison in this research are based on other experimental measurements at somewhat different experimental setting and higher temperature. Experiments at low temperature should be reproduced at ARCS to further confirm the accuracy of anharmonicity parameters, and conducting a

simulation test to identify the hardening effects.

(5) The influence of choosing various Q range at first energy peak is also considered in this study. The effect of choosing different Q range was in general smoothed by the integration and normalization between the conversion processes from a two dimensional plot to the VDOS spectrum and was believed not to affect the analysis of VDOS spectrum.

In this study, two temperatures of $PdH_{0.0011}$ experiments have been conducted to characterize the primary/first harmonic peak and higher order energy peaks through IINS. Although this research is just the beginning in studying higher order harmonic peaks, the recoil subtraction method developed in this study could be applied to future studies to subtract free recoil signals.

Bibliography

[1] D. L. Abernathy, M. B. Stone, M. J. Loguillo, M. S. Lucas, O. Delaire, X. Tang, J. Y. Y. Lin and B. Fultz, "Design and operation of the wide angular-range chopper spectrometer ARCS at the Spallation Neutron Source," *Rev. Sci. Instrum.,* vol. 83, 2012.

[2] R. A. Riedel, R. G. Cooper, L. L. Funk and L. G. Clonts, "Design and performance of vacuum capable detector electronics for linear position sensitive neutron detectors," *Nuclear Instruments and Methods in Physics Research, Section A: Accelerators, Spectrometers, Detectors and Associated Equipment,* vol. 664, pp. 366-369, 2012.

[3] H. Ju, "Interaction of Trapped Hydrogen with Dislocations at Low-Temperature in Deformed Pd," 2010.

[4] B. J. Heuser, J. S. King, G. C. Summerfield, F. Boué and J. E. Epperson, "Sans measurement of deuterium trapping at dislocations and grain boundaries in palladium," *Acta Metallurgica Et Materialia,* vol. 39, pp. 2815-2824, 1991.

[5] B. J. Heuser and J. S. King, "SANS measurements of deuterium-dislocation trapping in deformed single crystal Pd," *J. Alloys Compounds,* vol. 261, pp. 225-230, 1997.

[6] E. Fromm, H. Jehn, Solubility of hydrogen in the elements, Bulletin of Alloy Diagrams 5 (1984) 324-326.

[7] K. Sköld and G. Nelin, "Diffusion of hydrogen in the α-phase of Pd-H studied by small energy transfer neutron scattering," *Journal of Physics and Chemistry of Solids,* vol. 28, pp. 2369-2380, 1967.

[8] T. B. Flanagan, J. F. Lynch, J. D. Clewley and B. von Turkovich, "Hydrogen solubility as a probe for monitoring recovery in palladium," *Scripta Metallurgica,* vol. 9, pp. 1063-1068, 1975.

[9] M. T. Hutchings, *Introduction to the Characterization of Residual Stress by Neutron Diffraction*, 1 edition ed. CRC Press, 2005.

[10] K. Sköld and G. Nelin, "Diffusion of hydrogen in the α-phase of Pd-H studied by small energy transfer neutron scattering," *Journal of Physics and Chemistry of Solids,* vol. 28, pp. 2369-2380, 1967.

[11] DAVE: A comprehensive software suite for the reduction, visualization, and analysis of low energy neutron spectroscopic data, R.T. Azuah, L.R. Kneller, Y. Qiu, P.L.W. Tregenna-Piggott, C.M. Brown, J.R.D. Copley, and R.M. Dimeo, J. Res. Natl. Inst. Stan. Technol. 114, 341 (2009).

[12] Y. Fukai, *The metal-hydrogen system*, in Berlin: Springer-Verlag, 1993, .

[13] P. C. H. Mitchell, *Vibrational Spectroscopy with Neutrons*, in Singapore: World Scientific, 2005, .

[14] L. Koester, "Neutron scattering lengths and fundamental neutron interactions," vol. 88, 1977.

[15] J. P. Hirth and B. Carnahan, "Hydrogen adsorption at dislocations and cracks in Fe," *Acta Metallurgica*, vol. 26, pp. 1795-1803, 1978.

[16] J. P. Hirth and J. Lothe, *Theory of Dislocations*, Second Edition ed. John Wiley & Sons.

[17] M. Maxelon, A. Pundt, W. Pyckhout-Hintzen, J. Barker and R. Kirchheim, "Interaction of hydrogen and deuterium with dislocations in palladium as observed by small angle neutron scattering," *Acta Materialia*, vol. 49, pp. 2625-2634, 2001.

[18] R. Kirchheim, "Interaction of hydrogen with dislocations in palladium—II. Interpretation of activity results by a fermi-dirac distribution," *Acta Metallurgica*, vol. 29, pp. 845-853, 5, 1981.

[19] D. Wang, T. B. Flanagan and T. Kuji, "Hysteresis scans for Pd-H and Pd-alloy-H systems," *Physical Chemistry Chemical Physics*, vol. 4, pp. 4244-4254, 2002.

[20] H. C. Jamieson, G. C. Weatherly and F. D. Manchester, "The $\beta \rightarrow \alpha$ phase transformation in palladium-hydrogen alloys," *Journal of the Less Common Metals*, vol. 50, pp. 85-102, 11, 1976.

[21] A. K. Ghatak and L. S. Kothari, *An Introduction to Lattice Dynamics* Addison-Wesley Publishing Company, 1972.

[22] G. E. Bacon, *Neutron Diffraction* Oxford: Clarendon Press, 1962.

[23] G. L. Squires, *Introduction to the Theory of Thermal Neutron Scattering* Cambridge: Cambridge University Press, 1978.

[24] F. Fillaux, H. Ouboumour, J. Tomkinson and L. T. Yu, "An inelastic neutron scattering study of the proton dynamics in γ-MnO_2," *Chem. Phys.*, vol. 149, pp. 459-469, 1991.

[25] J. M. Rowe, J. J. Rush, H. G. Smith, M. Mostoller and H. E. Flotow, "Lattice dynamics of a single crystal of $PdD_{0.63}$," *Physical Review Letters*, vol. 33, pp. 1297-1300., 1974.

[26] M. R. Chowdhury and D. Ross, "Neutron-Scattering Study of Vibrational Modes of Hydrogen in Beta-Phases of Pd-H, Pd-10Ag-H and Pd-20Ag-H," *Solid State Commun.*, vol. 13, pp. 229-234, 1973.

[27] W. Drexel, A. Murani, D. Tocchetti, W. Kley, I. Sosnowska and D. Ross, "Motions of Hydrogen Impurities in Alpha-Palladium-Hydride," *Journal of Physics and Chemistry of Solids*, vol. 37, pp. 1135-1139, 1976.

[28] A. Rahman, K. Sköld, C. Pelizzari, S. K. Sinha and H. Flotow, "Phonon spectra of nonstoichiometric palladium hydrides," *Physical Review B,* vol. 14, pp. 3630-3634, 1976.

[29] J. J. Rush, J. M. Rowe and D. Richter, "Direct determination of the anharmonic vibrational potential for H in Pd," *Zeitschrift Für Physik B Condensed Matter,* vol. 55, pp. 283-286, 1984.

[30] J. J. Rush, J. M. Rowe and D. Richter, "Dynamics of dilute H in β-phase palladium deuteride: A novel mass defect," *Physical Review B,* vol. 31, pp. 6102-6103, 1985.

[31] D. K. Ross, V. E. Antonov, E. L. Bokhenkov, A. I. Kolesnikov, E. G. Ponyatovsky and J. Tomkinson, "Strong anisotropy in the inelastic neutron scattering from PdH at high energy transfer," *Physical Review B - Condensed Matter and Materials Physics,* vol. 58, pp. 2591-2595, 1998.

[32] M. Kemali, J. E. Totolici, D. K. Ross and I. Morrison, "Inelastic Neutron Scattering Measurements and Ab Initio Calculations of Hydrogen in Single-Crystal Palladium," *Phys. Rev. Lett.,* vol. 84, pp. 1531-1534, 2000.

[33] B. J. Heuser, T. J. Udovic and H. Ju, "Vibrational density of states measurement of hydrogen trapped at dislocations in deformed PdH0.0008," *Physical Review B - Condensed Matter and Materials Physics,* vol. 78, 2008.

[34] D. R. Trinkle, H. Ju, B. J. Heuser and T. J. Udovic, "Nanoscale hydride formation at dislocations in palladium: Ab initio theory and inelastic neutron scattering measurements,"*Physical Review B - Condensed Matter and Materials Physics,* vol. 83, 2011.

[35] F. Fillaux, S. M. Bennington, J. Tomkinson and L. T. Yu, "Inelastic neutron-scattering study of free proton dynamics in γ-MnO 2," *Chem. Phys.,* vol. 209, pp. 111-125, 1996.

[36] B. S. Schirato, K. W. Herwig, P. E. Sokol and J. W. White, "Deep inelastic neutron scattering from chemisorbed hydrogen in potassium intercalated graphite," *Chemical Physics Letters,* vol. 165, pp. 453-456, 1990.

[37] D. N. Beshers, "On the distribution of impurity atoms in the stress field of a dislocation," *Acta Metallurgica,* vol. 6, pp. 521-523, 8, 1958.

[38] F. A. Lewis, *The Palladium Hydrogen System.* London: Academic Press, 1967.

[39] Y. Fukai, *The metal-hydrogen system,* in Berlin: Springer-Verlag, 2005 .

[40] A. P. Miller and B. N. Brockhouse, "Anomalous behavior of the lattice vibrations and the electronic specific heat of palladium," *Phys. Rev. Lett.,* vol. 20, pp. 798-801, 1968.

[41] C. J. Glinka, J. M. Rowe, J. J. Rush, A. Rahman, S. K. Sinha and H. E. Flotow, "Inelastic-neutron-scattering line shapes in PdD0.63," *Physical Review B,* vol. 17, pp. 488-493, 1978.

[42] A. I. Kolesnikov, I. Natkaniec, V. E. Antonov, I. T. Belash, V. K. Fedotov, J. Krawczyk, J. Mayer and E. G. Ponyatovsky, "Neutron spectroscopy of MnH0.86, NiH1.05, PdH0.99 and harmonic behaviour of their optical phonons," *Physica B: Physics of Condensed Matter,* vol. 174, pp. 257-261, 1991.

[43] P. E. Sokol, K. Sköld, D. L. Price and R. Kleb, "High-momentum-transfer inelastic neutron scatterins from liquid helium-3," *Phys. Rev. Lett.*, vol. 54, pp. 909-912, 1985.

[44] R. J. Olsen, M. Beckner, M. B. Stone, P. Pfeifer, C. Wexler and H. Taub, "Quantum excitation spectrum of hydrogen adsorbed in nanoporous carbons observed by inelastic neutron scattering," *Carbon,* 2013.

Appendix A

Figure A.1: The Gaussian fitting of 5 K Net data at high energy region, with Q step as 0.6 Å^{-1}, in a increment of 0.2 Å^{-1}. The fitting range starts from 8.4 to 12.4.

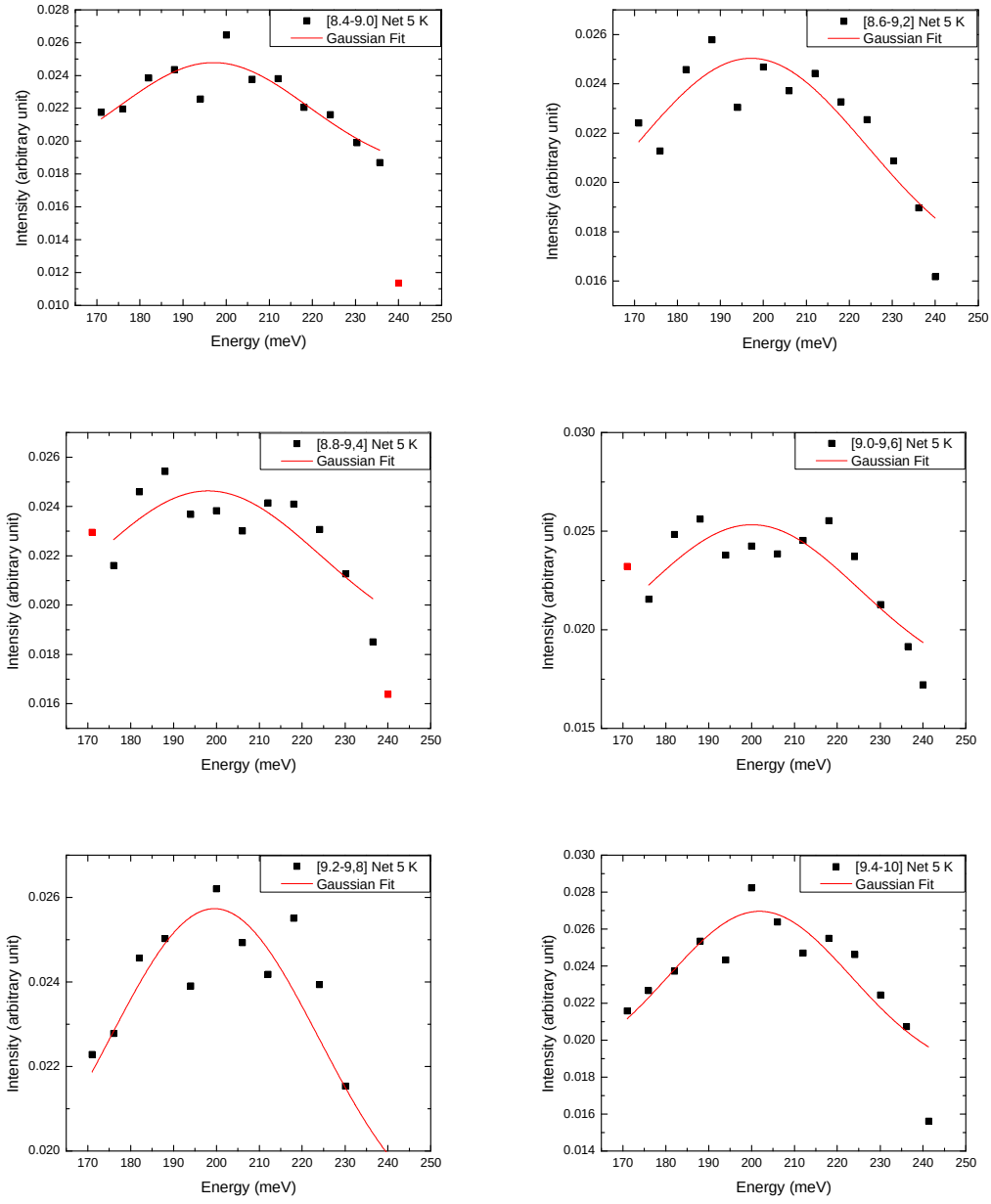

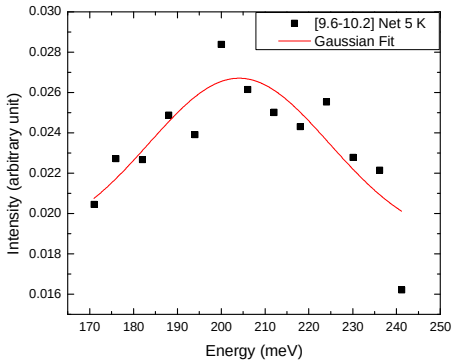
[9.6-10.2] Net 5 K
Gaussian Fit
Intensity (arbitrary unit)
Energy (meV)

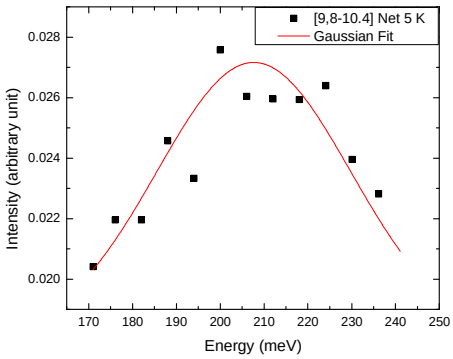
[9,8-10.4] Net 5 K
Gaussian Fit
Intensity (arbitrary unit)
Energy (meV)

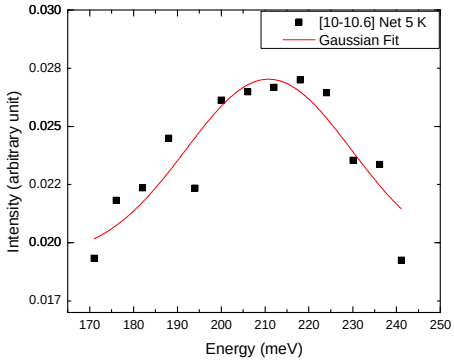
[10-10.6] Net 5 K
Gaussian Fit
Intensity (arbitrary unit)
Energy (meV)

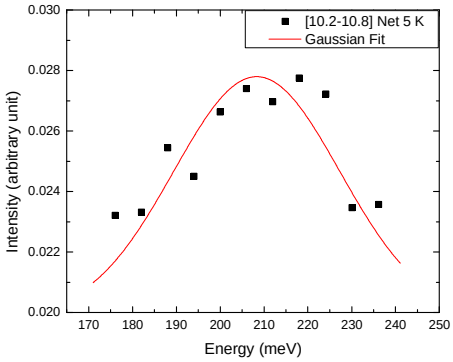
[10.2-10.8] Net 5 K
Gaussian Fit
Intensity (arbitrary unit)
Energy (meV)

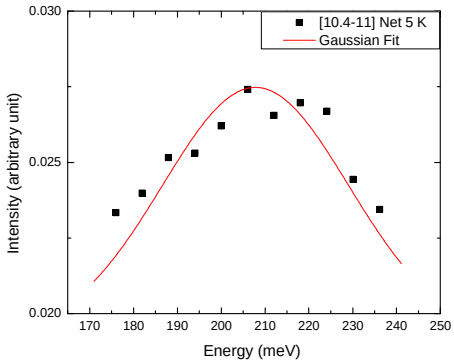
[10.4-11] Net 5 K
Gaussian Fit
Intensity (arbitrary unit)
Energy (meV)

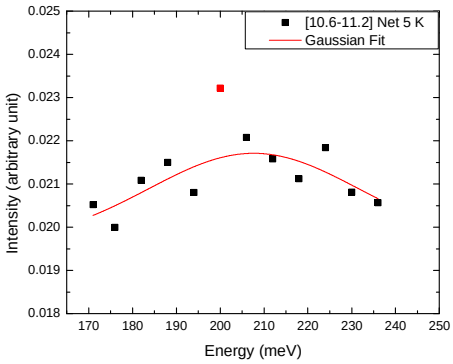
[10.6-11.2] Net 5 K
Gaussian Fit
Intensity (arbitrary unit)
Energy (meV)

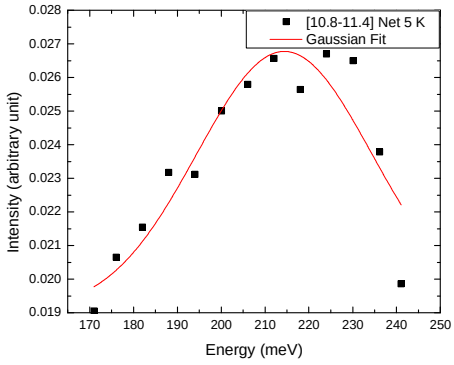
[10.8-11.4] Net 5 K
Gaussian Fit
Intensity (arbitrary unit)
Energy (meV)

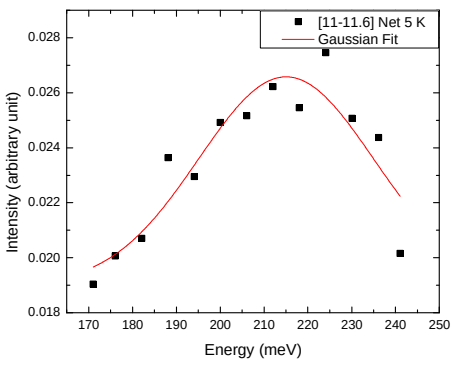
[11-11.6] Net 5 K
Gaussian Fit
Intensity (arbitrary unit)
Energy (meV)

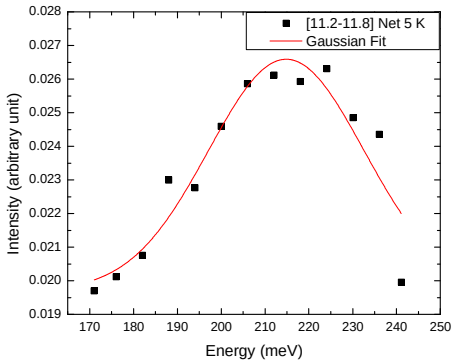
[11.2-11.8] Net 5 K
Gaussian Fit
Intensity (arbitrary unit)
Energy (meV)

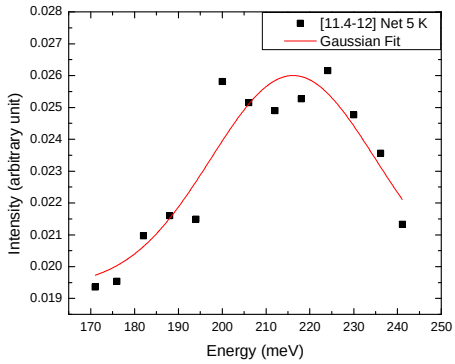
[11.4-12] Net 5 K
Gaussian Fit
Intensity (arbitrary unit)
Energy (meV)

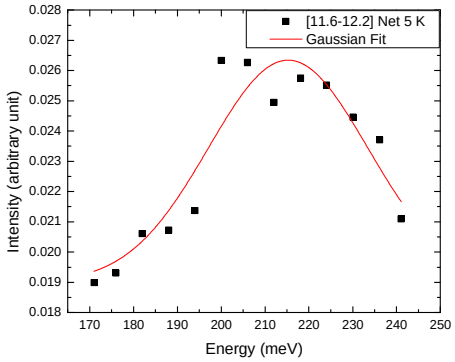
[11.6-12.2] Net 5 K
Gaussian Fit
Intensity (arbitrary unit)
Energy (meV)

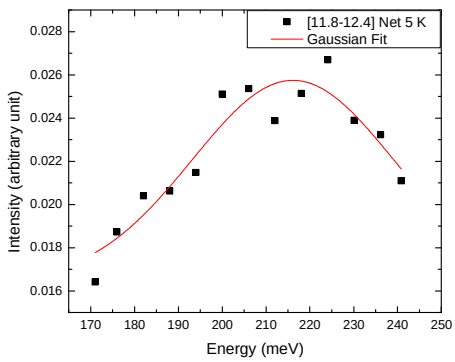
[11.8-12.4] Net 5 K
Gaussian Fit
Intensity (arbitrary unit)
Energy (meV)

Figure A.2: The Gaussian fitting of 300 K Net data at high energy region, with Q step as 0.6 Å^{-1}, in a increment of 0.2 Å^{-1}. The fitting range starts from 8.0 to 12.4.

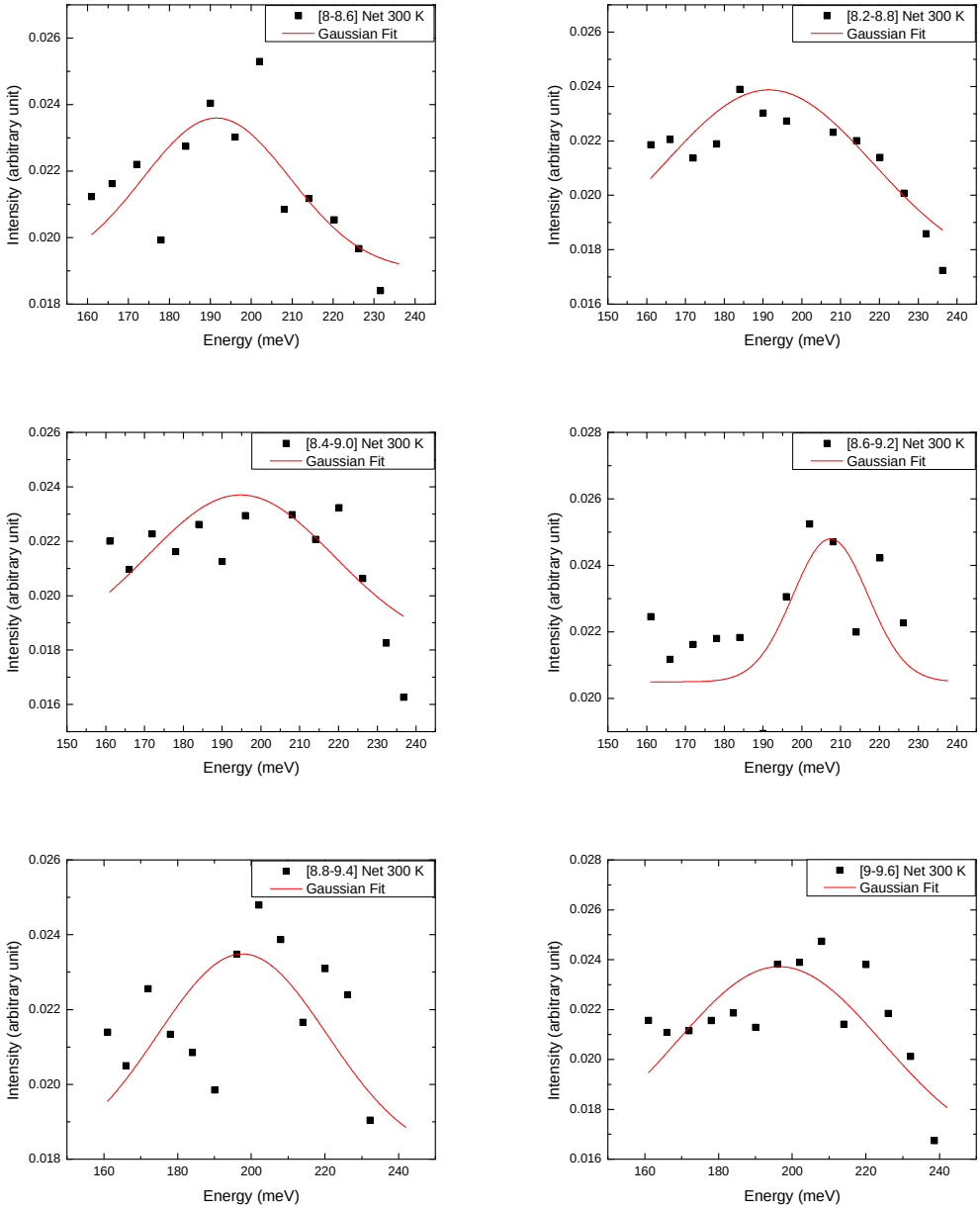

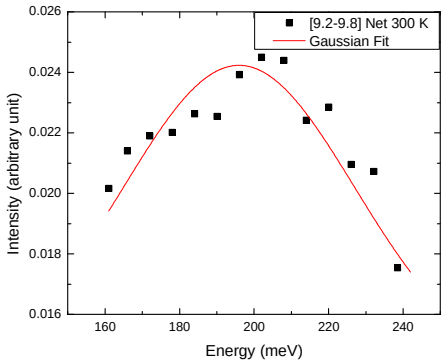
[9.2-9.8] Net 300 K
Gaussian Fit
Intensity (arbitrary unit)
Energy (meV)

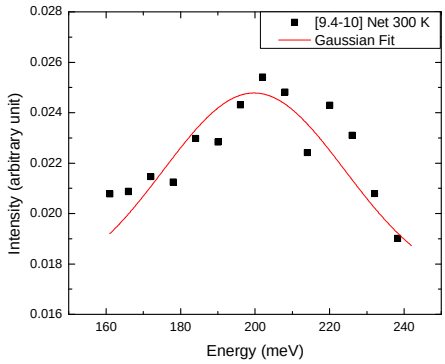
[9.4-10] Net 300 K
Gaussian Fit
Intensity (arbitrary unit)
Energy (meV)

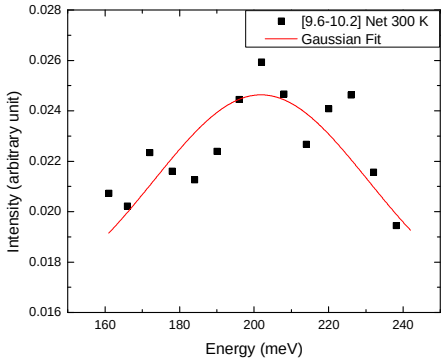
[9.6-10.2] Net 300 K
Gaussian Fit
Intensity (arbitrary unit)
Energy (meV)

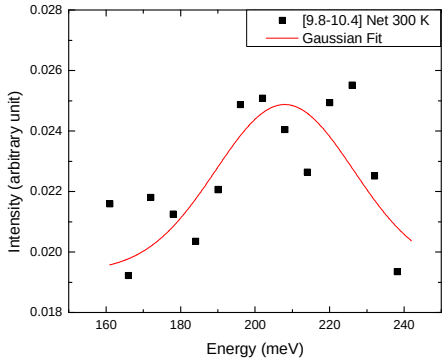
[9.8-10.4] Net 300 K
Gaussian Fit
Intensity (arbitrary unit)
Energy (meV)

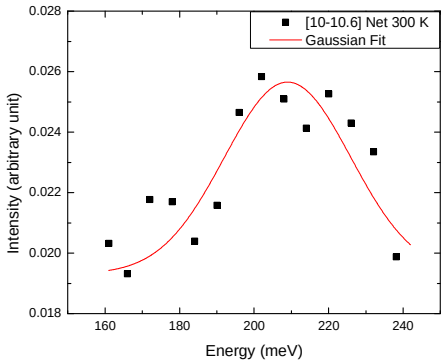
[10-10.6] Net 300 K
Gaussian Fit
Intensity (arbitrary unit)
Energy (meV)

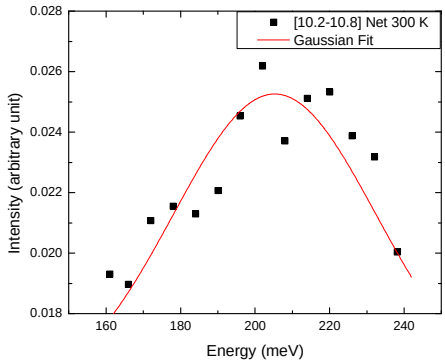
[10.2-10.8] Net 300 K
Gaussian Fit
Intensity (arbitrary unit)
Energy (meV)

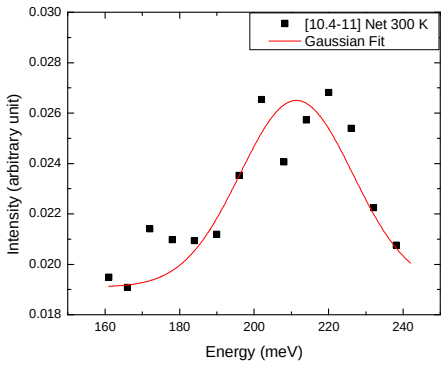
[10.4-11] Net 300 K
Gaussian Fit
Intensity (arbitrary unit)
Energy (meV)

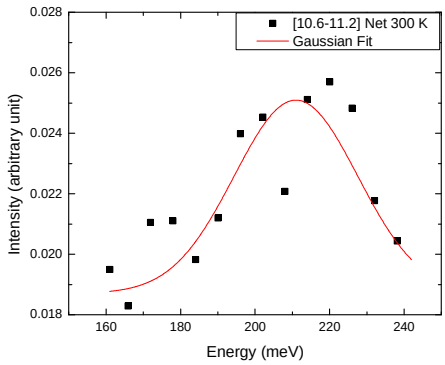
[10.6-11.2] Net 300 K
Gaussian Fit
Intensity (arbitrary unit)
Energy (meV)

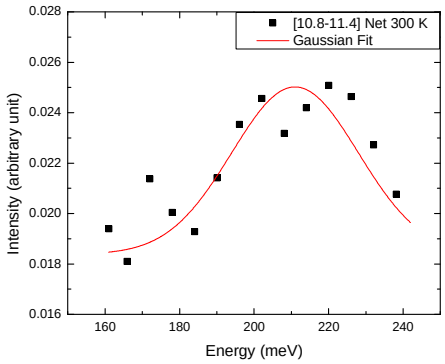
[10.8-11.4] Net 300 K
Gaussian Fit
Intensity (arbitrary unit)
Energy (meV)

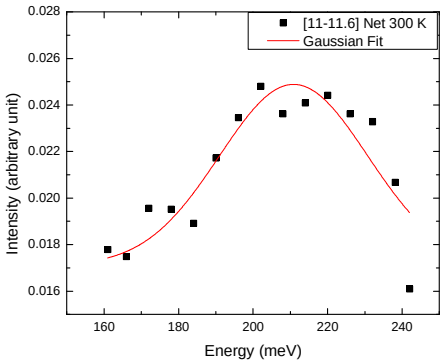
[11-11.6] Net 300 K
Gaussian Fit
Intensity (arbitrary unit)
Energy (meV)

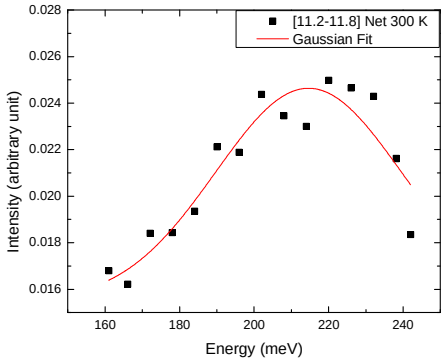
[11.2-11.8] Net 300 K
Gaussian Fit
Intensity (arbitrary unit)
Energy (meV)

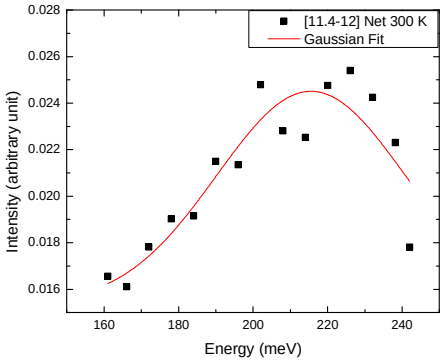
[11.4-12] Net 300 K
Gaussian Fit
Intensity (arbitrary unit)
Energy (meV)

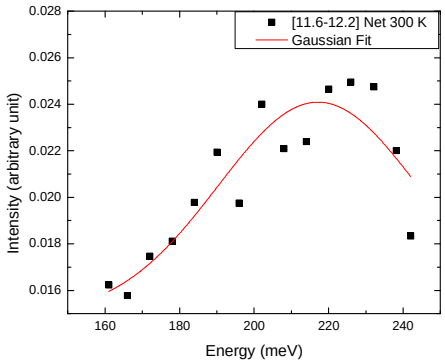
[11.6-12.2] Net 300 K
Gaussian Fit
Intensity (arbitrary unit)
Energy (meV)

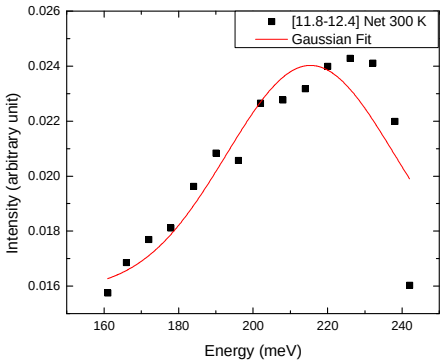
[11.8-12.4] Net 300 K
Gaussian Fit
Intensity (arbitrary unit)
Energy (meV)

Table A.1: The Gaussian fitting results for the 5 K Net data at higher energy region.

Q Range, E Step=6 meV	w	E_R	A	y0	Re-qui square	Qmean	A*(Qmean)	M (Kg)
8.4-9,6	21.95774	197.0512	0.00679	0.018	0.7244	8.7	5.91E-02	1.33E-27
8.6-9.2	26.95727	197.145	0.00904	0.016	0.71946	8.9	8.05E-02	1.39E-27
8.8-9.4	26.19237	198.0621	0.00634	0.018	0.5166	9.1	5.77E-02	1.45E-27
9-9.6	25.1341	200	0.00833	0.017	0.63725	9.3	7.75E-02	1.50E-27
9.2-9.8	24.25247	199.539	0.00774	0.018	0.74785	9.5	7.35E-02	1.57E-27
9.4-10	21.3646	201.8871	0.00897	0.018	0.68894	9.7	8.70E-02	1.62E-27
9.6-10.2	20.57477	204.07352	0.00821	0.0185	0.61146	9.9	8.13E-02	1.67E-27
9.8-10.4	22.10165	207.66037	0.00916	0.018	0.63391	10.1	9.25E-02	1.70E-27
10-10.6,6	18.881	210.809	0.0077	0.01933	0.773	10.3	7.93E-02	1.75E-27
10.2-10.8,6	18.9513	208.3292	0.00796	0.01984	0.7216	10.5	8.36E-02	1.84E-27
10.4-11	21.22645	207.8242	0.00823	0.01925	0.7588	10.7	8.81E-02	1.91E-27
10.6-11.2	23.9714	207.64	0.00209	0.01963	0.4307	10.9	2.28E-02	1.99E-27
10.8-11.4	19.95	214.3925	0.0077	0.01903	0.824	11.1	8.55E-02	1.99E-27
11-11.6	19.9554	215.333	0.00758	0.019	0.79942	11.3	8.57E-02	2.06E-27
11.2-11.8	17.71714	214.839	0.0069	0.0197	0.8683	11.5	7.94E-02	2.14E-27
11.4-12	18.7542	216.167	0.00664	0.01936	0.86131	11.7	7.77E-02	2.20E-27
11.6-12.2	18.15255	215.2623	0.00736	0.01899	0.8513	11.9	8.76E-02	2.28E-27
11.8-12.4	22.9519	216.13475	0.00932	0.01643	0.86826	12.1	1.13E-01	2.35E-27
Mean	21.34435	207.42155	0.00786	0.01853	0.73421	10.36667	0.08111	1.80E-27
Standard deviation	2.98483	6.91242	8.42E-04	0.00105	0.10239	0.9759	8.19E-03	2.82E-28
2 times of standard deviation	5.96966	13.82484	1.68E-03	0.0021	0.20478	1.9518	0.01638	5.64E-28
Upper limit	27.31401	221.24639	0.009543456	0.02063	0.93899	12.31847	0.09749	2.36902E-27
Lower limit	15.37469	193.59671	0.006176544	0.01643	0.52943	8.41487	0.06473	1.24042E-27
the # of data get excluded							1	0
90% confidence level	4.909611	11.36992583	0.00138452	0.001727	0.168416662	1.605213604	0.013471359	4.64099E-28
Upper limit	26.25396	218.7914758	0.00924452	0.020257	0.902626662	11.9718836	0.094581359	2.26882E-27
Lower limit	16.43474	196.0516242	0.00647548	0.016803	0.565793338	8.761456396	0.067638641	1.34062E-27
the # of data get excluded	1		1				0	1
the new mean	20.73859	208.4045	0.00793	0.01875	0.74382	10.4667	0.08258	1.83E-27

Table A.2: The Gaussian fitting results for the 300 K Net data at higher energy region.

Q Range, E Step=6 meV	w	E_R	A	y0	Re-qui square	Qmean	A*(Qmean)	M (Kg)
8-8.6	18	191.5149	0.0046	0.019	0.38329	8.3	0.03818	1.24843E-27
8.2-8.8	26.5031	191.503	0.00688	0.017	0.63257	8.5	0.05848	1.3094E-27
8.4-9	24.0877	194.752	0.0057	0.018	0.38077	8.7	0.04959	1.34886E-27
8.6-9.2	9.66586	207.3686	0.0043	0.0205	0.23348	8.9	0.03827	1.32571E-27
8.8-9.4	23.00898	197.608	0.00549	0.018	0.32531	9.1	0.049959	1.45442E-27
9-9.6	28.04597	196.506	0.00772	0.016	0.49422	9.3	0.071796	1.52757E-27
9.2-9.8	30.99717	195.963	0.01023	0.014	0.71726	9.5	0.097185	1.5984E-27
9.4-10	24.353	199.7311	0.0078	0.017	0.56042	9.7	0.07566	1.63497E-27
9.6-10.2	28.76965	201.85	0.00864	0.016	0.52774	9.9	0.085536	1.68521E-27
9.8-10.4	18.5	207.942	0.00552	0.01935	0.42505	10.1	0.055752	1.7026E-27
10-10.6	17	208.9945	0.00634	0.01931	0.62328	10.3	0.065302	1.76178E-27
10.2-10.8	27.18324	205.262	0.01011	0.01515	0.62053	10.5	0.106155	1.86415E-27
10.4-11	15.11699	211.3613	0.0074	0.0191	0.59802	10.7	0.07918	1.87998E-27
10.6-11.2	16.60287	210.9705	0.00639	0.01871	0.50328	10.9	0.069651	1.95453E-27
10.8-11.4	17	210.9879	0.00664	0.01838	0.49372	11.1	0.073704	2.02675E-27
11-11.6	19.8711	210.869	0.00779	0.01709	0.76634	11.3	0.088027	2.10163E-27
11.2-11.8	24.93429	214.645	0.00916	0.01548	0.84551	11.5	0.10534	2.13839E-27
11.4-12	25.26984	215.5385	0.00916	0.01535	0.7791	11.7	0.107172	2.20424E-27
11.6-12.2	26.84623	217.1417	0.00916	0.01493	0.75894	11.9	0.109004	2.2634E-27
11.8-12.4	22.4856	215.3957	0.00819	0.01584	0.74339	12.1	0.099099	2.35909E-27
Mean	23.62	206.9858	0.00825	0.1659	0.66108	10.5333	0.08722	1.87E-27
Standard deviation	5.1941	8.15915	0.00135	0.00174	0.10972	1.01205	0.01778	2.84E-28
2 times of standard deviation	10.3882	16.3183	0.0027	0.00348	0.21944	2.0241	0.03556	5.68386E-28
Upper limit	34.0082	223.3041	0.01095	0.16938	0.88052	12.5574	0.12278	2.43473E-27
Lower limit	13.2318	190.6675	0.00555	0.16242	0.44164	8.5092	0.05166	1.29795E-27

Appendix B

```
% File Reader Delimiter and Number of Header Lines
DELIMITER = ' ';
HEADERLINES = 0;
filename='Net 300K [1.17].iexy';
% Import Data from IEXY file into importData
importData = importdata(filename, DELIMITER, HEADERLINES);
% Create New Array Called Data and Copy Only Positive Intensities into
% Data
data=zeros(length(importData),4);
last=1;

% Copy Important Data from importData Matrix into data Matrix
for i=1:length(importData)
    % if importData(i,1) is valid( take the negative into account)
    if importData(i,1) ~= -1.000e+20
        for j=1:4
            data(last,j)=importData(i,j);
        end
        last=last+1;
    end
end
% Trim Leftover Zeroes from Preallocation of Data Matrix
data=data(1:last-1,1:4);

% Check What the Data Looks Like
% display(data);

% Creat a matrix called Irecoil
Irecoil=zeros(length(data),4);
% Define the constant in the recoil intensity formula
A=0.08722;
SquareSigmaP=5.53389;
Er=206.9858;

last2=1;
```

```
% Calculate the Recoil Intensity then stored in the Irecoil matrix
% With SquareSignaP not taking into account of the Q, BUT times the Q^2
% based on each dataset
for i=1:length(data)

Irecoil(last2,1)=(A/data(i,3))*expm(-1*(data(i,4)-Er)^2/(2*SquareSigmaP*data(i,3)*d
ata(i,3)));
    last2=last2+1;
end

% Stored the Error, Q and E info into the Irecoil matrix with the first
% column as the recoil Intensity
last3=1;
for i=1:length(data)
    k=2:4;
    Irecoil(last3,k)=data(i,k);
    last3=last3+1;
end

%Check what the Irecoil looks like
%display(Irecoil)

% Create a matrix for storing the net data
NetData=zeros(length(data),4);

last4=1;
% Calculate the Net data
for i=1:length(data)
    NetData(last4,1)=data(i,1)-Irecoil(i,1);
    last4=last4+1;
end

% stored the Error, Q and E info into the Irecoil matrix with the first
% column as the Net Intensity
last5=1;
for i=1:length(data)
    l=2:4;
    NetData(last5,l)=data(i,l);
```

```
    last5=last5+1;
end

% Export the final NetData file and paste it on Excel, the net data already
% subtract the reoil intensity out of it.
display(NetData)

%Before operating this part of the code, the NetData have to be realligned
%based on Energy, saved the file and run this part of the code

%File Reader Delimiter and Number of Header Lines
DELIMITER = ' ';
HEADERLINES = 0;
filename='0214NetDataSortByE-net.mat';
%Import Data from IEXY file into importData
NetDataSortByE = importdata(filename, DELIMITER, HEADERLINES);

display(NetDataSortByE(329,4))

%Garbage collection
clear('last','last2','last3','last4','last5','NetData','Irecoil','data','importData');

%Set Initial values for the for loop
Intensity=0;
Error=0;
last6=1;
averageMatrix=zeros(length(NetDataSortByE),2);

%Creat a for loop to summarize the intensity and error at one energy
for i=1:length(NetDataSortByE)-1
    if isequal(NetDataSortByE(i,4),NetDataSortByE(i+1,4))
        Intensity=Intensity+NetDataSortByE(i,1);
        Error=Error+NetDataSortByE(i,2);
        last6=last6+1;
    else
        %add the last intensity belongs to the same E on top of the
        %Intensity
        Intensity=Intensity+NetDataSortByE(i,1);
```

```
        Error=Error+NetDataSortByE(i,2);
        averageMatrix(k,1)=Intensity/(last6);
        averageMatrix(k,2)=Error/(last6);
        %Reset counter
        Intensity=0;
        Error=0;
        k=k+1;
        last6=0;
    end
end


display(averageMatrix)
```

Appendix C

The influence of the Q range on the results of first harmonic peak is considered here. The Q region for higher energy peak is relatively restrained; therefore, the first harmonic peak was chosen to demonstrate the influence of different Q range. The results should be explained with Figure 4.2 and Figure 4.3, since the VDOS spectrum is the integration of the two dimensional plot. Figure C.1 show the VDOS spectra at 5 K starting with the same Q but with incremental range. Figure C.4 to 6 show the same VDOS spectra at 300 K. From the comparison, the peak location does not shift with extended range, but the peak width became broader due to the inclusion of extra lower energy intensity data. Figure and Figure present the comparison of VDOS spectra end with the same Q number to identify the influence caused by starting with different Q point. The comparison indicates that the peak location stays constant with various starting point, but with sharper slope increase due to the inclusion of the low energy low Q data, which is most likely to be affected by poor resolution. However, in the analysis for first harmonic peak, 1-10 $Å^{-1}$ was chosen as the Q range to include the possible data that contributed to the intensity of first harmonic peak. The error bars are not presented due to the relatively small scale to the measured intensity.

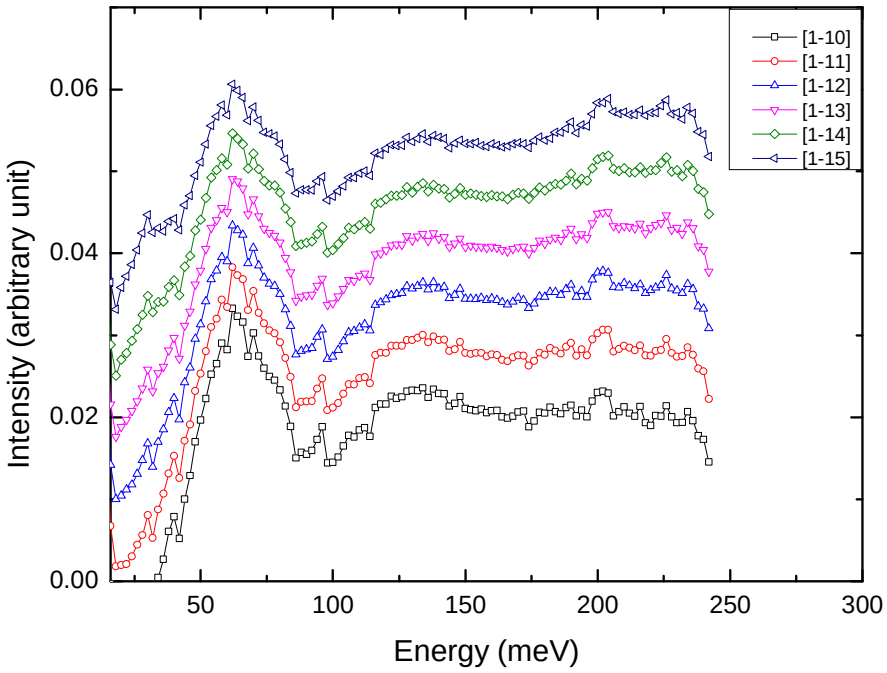

Figure C.1: IINS 5K Net data with various Q range starting from Q=1 $Å^{-1}$.

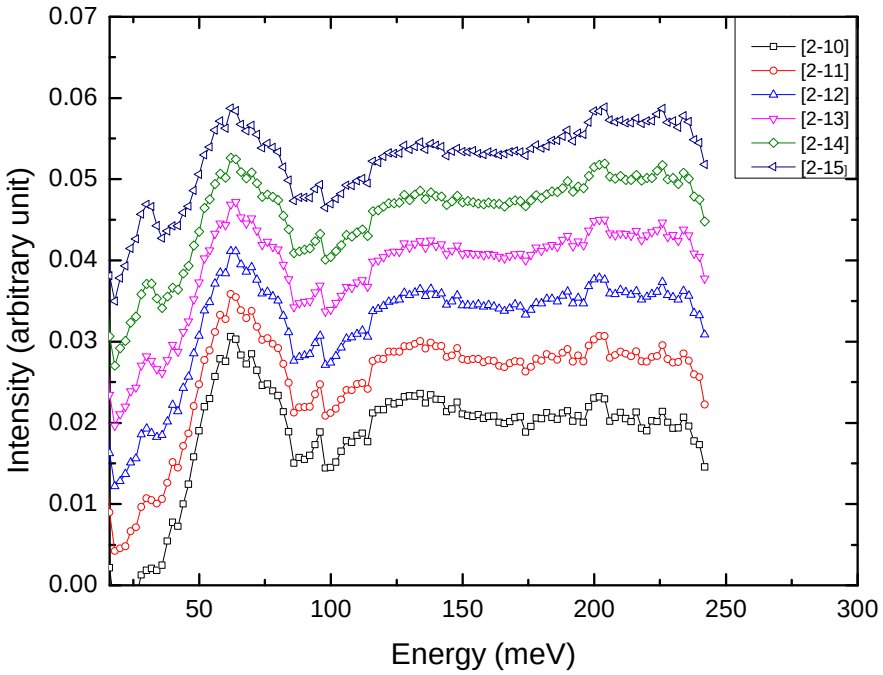

Figure C.2: IINS 5K Net data with various Q range starting from Q=2 $Å^{-1}$.

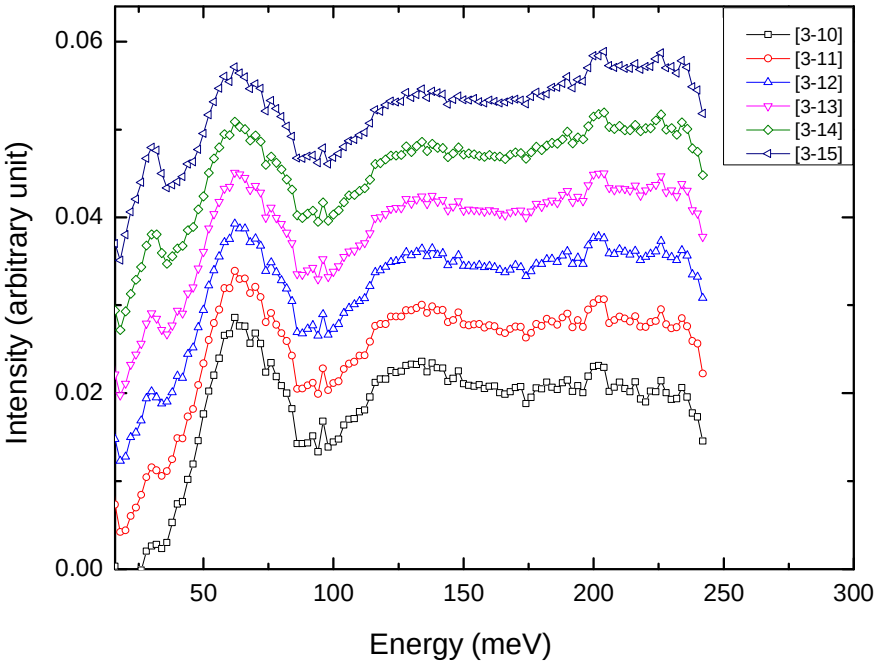

Figure C.3: IINS 5K Net data with various Q range starting from Q=3 $Å^{-1}$.

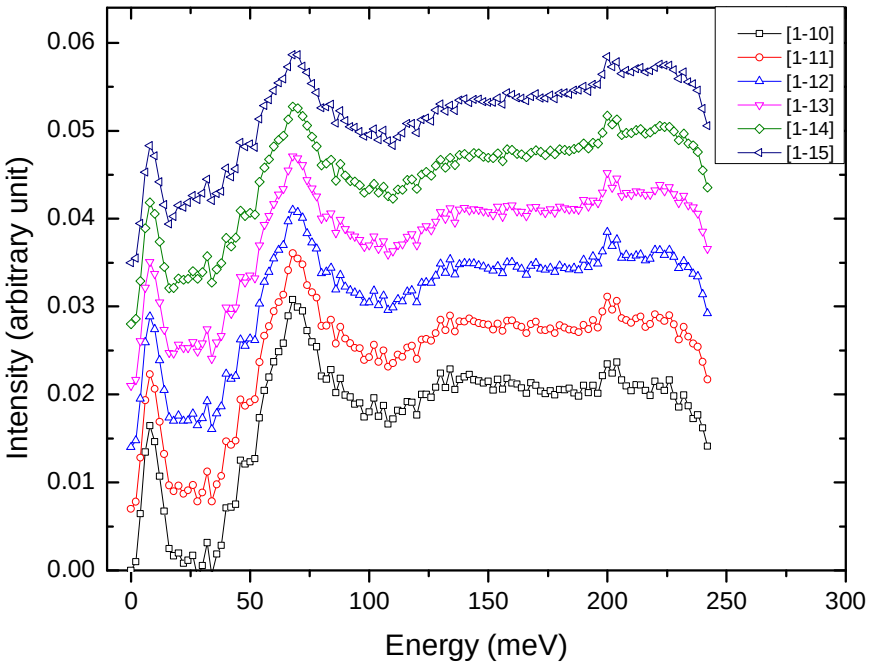

Figure C.4: IINS 300K Net data with various Q range starting from Q=1 $Å^{-1}$.

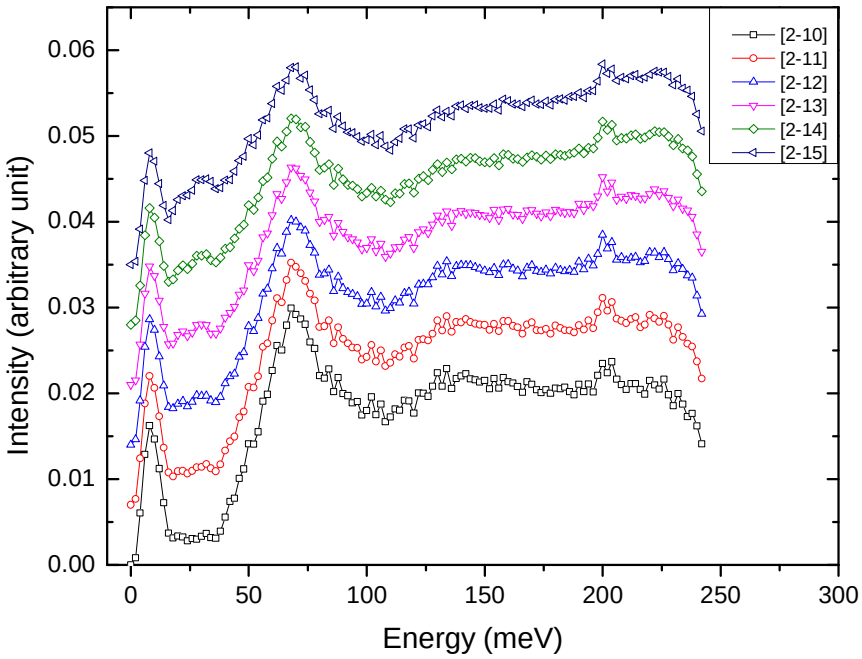

Figure C.5: IINS 300K Net data with various Q range starting from Q=2 $Å^{-1}$.

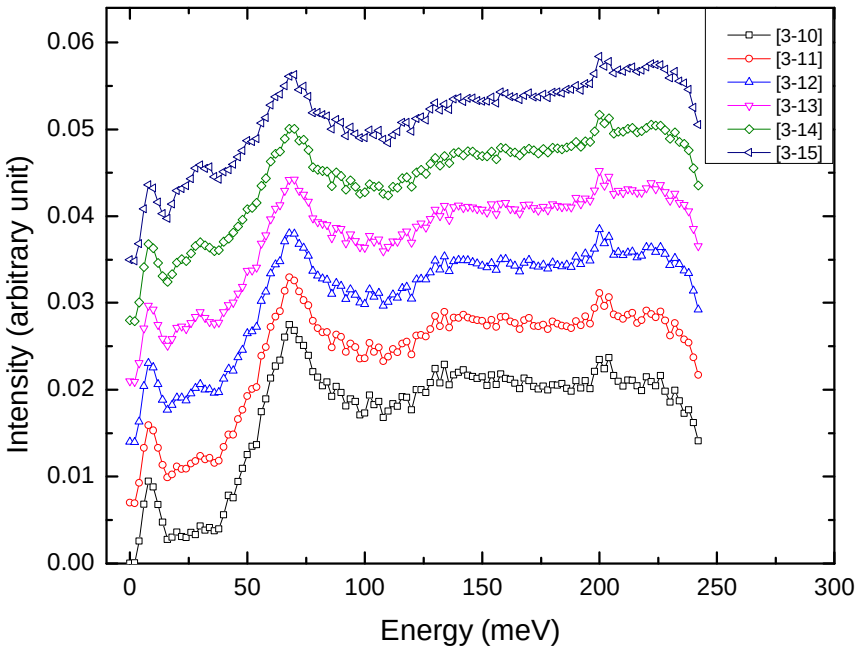

Figure C.6: IINS 300K Net data with various Q range starting from Q=3 $Å^{-1}$.

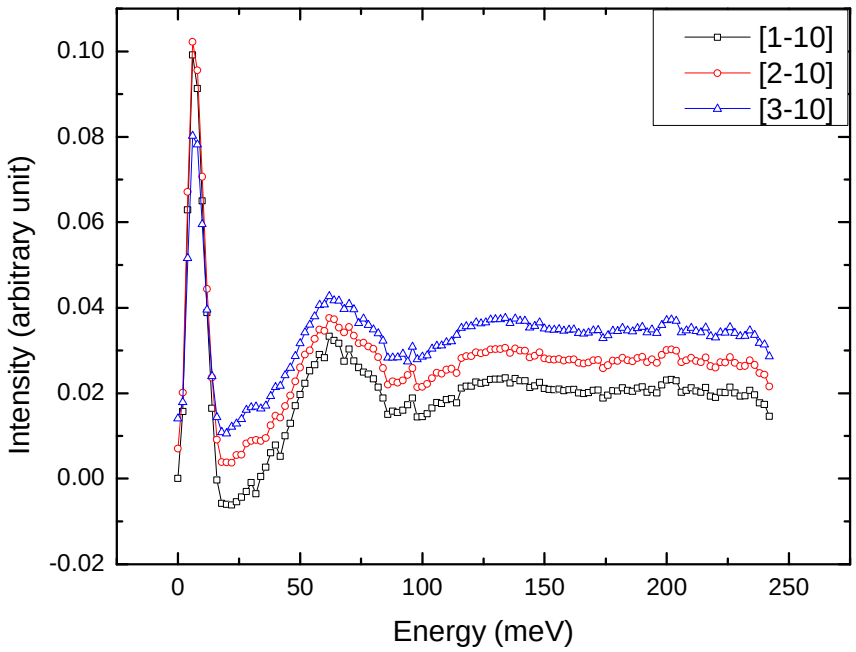
[1-10]
[2-10]
[3-10]
Intensity (arbitrary unit)
Energy (meV)
0.10
0.08
0.06
0.04
0.02
0.00
-0.02
0
50
100
150
200
250

(a)

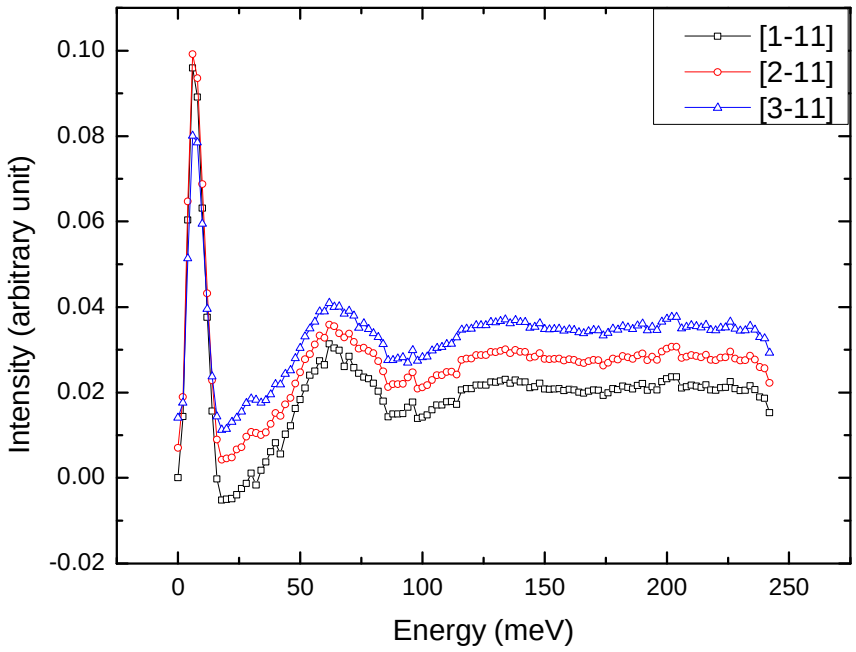
[1-11]
[2-11]
[3-11]
Intensity (arbitrary unit)
Energy (meV)
0.10
0.08
0.06
0.04
0.02
0.00
-0.02
0
50
100
150
200
250

(b)

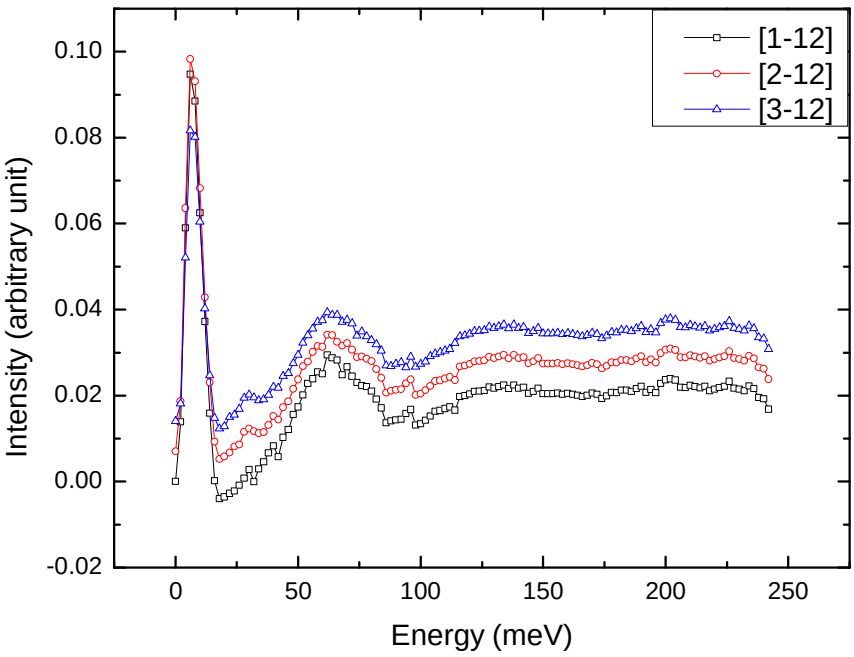
[1-12]
[2-12]
[3-12]
Intensity (arbitrary unit)
Energy (meV)
0.10
0.08
0.06
0.04
0.02
0.00
-0.02
0
50
100
150
200
250

(c)

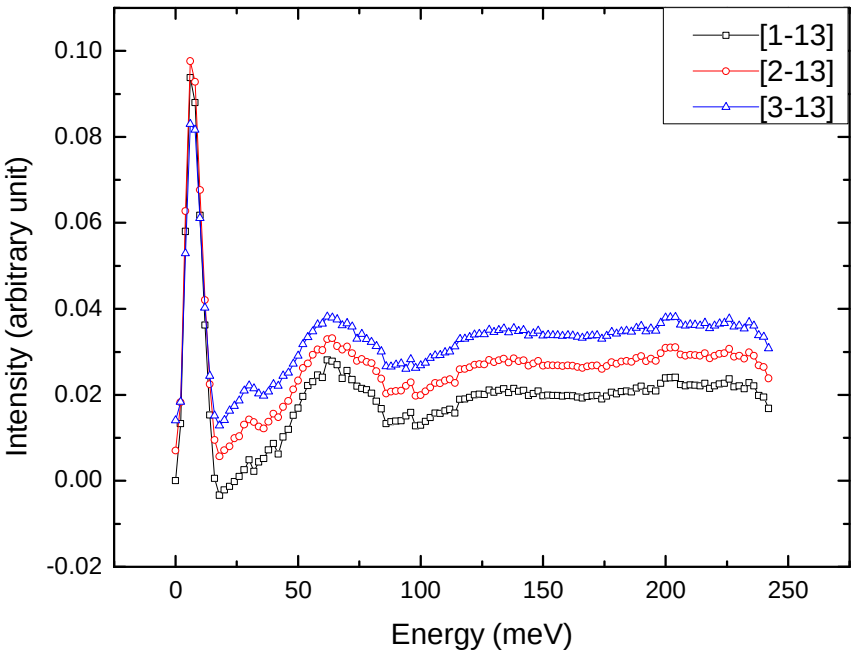
[1-13]
[2-13]
[3-13]
Intensity (arbitrary unit)
Energy (meV)
0.10
0.08
0.06
0.04
0.02
0.00
-0.02
0
50
100
150
200
250

(d)

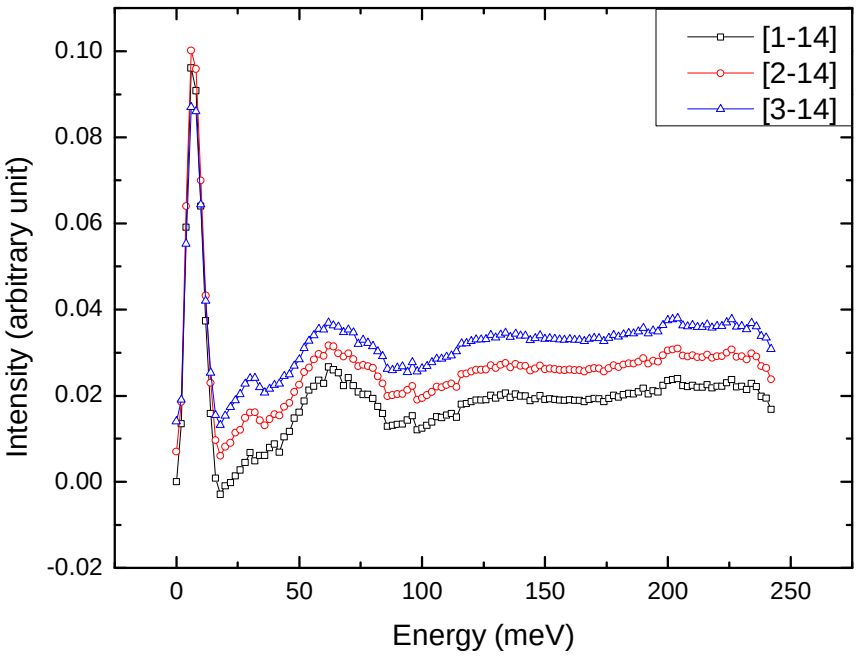

(e)

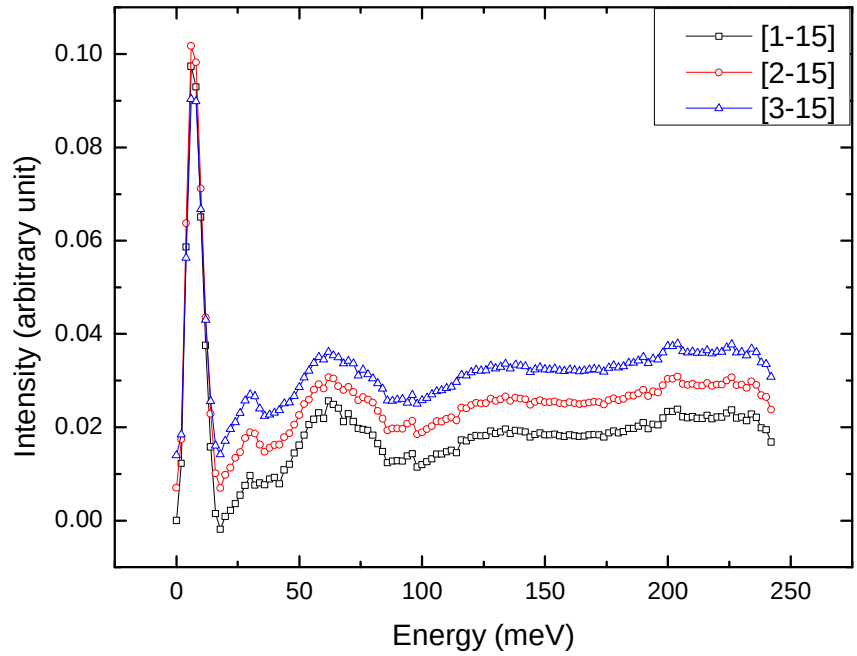

(f)

Figure C.7 (a)-(f): Comparison of IINS 5K Net data with various Q range.

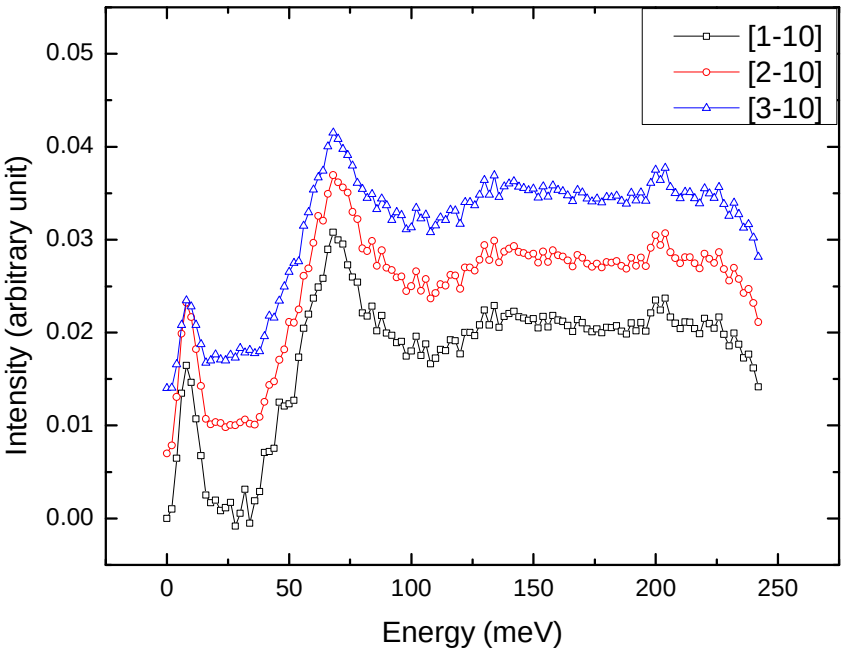
[1-10]
[2-10]
[3-10]
Intensity (arbitrary unit)
Energy (meV)
0.00
0.01
0.02
0.03
0.04
0.05
0
50
100
150
200
250

(a)

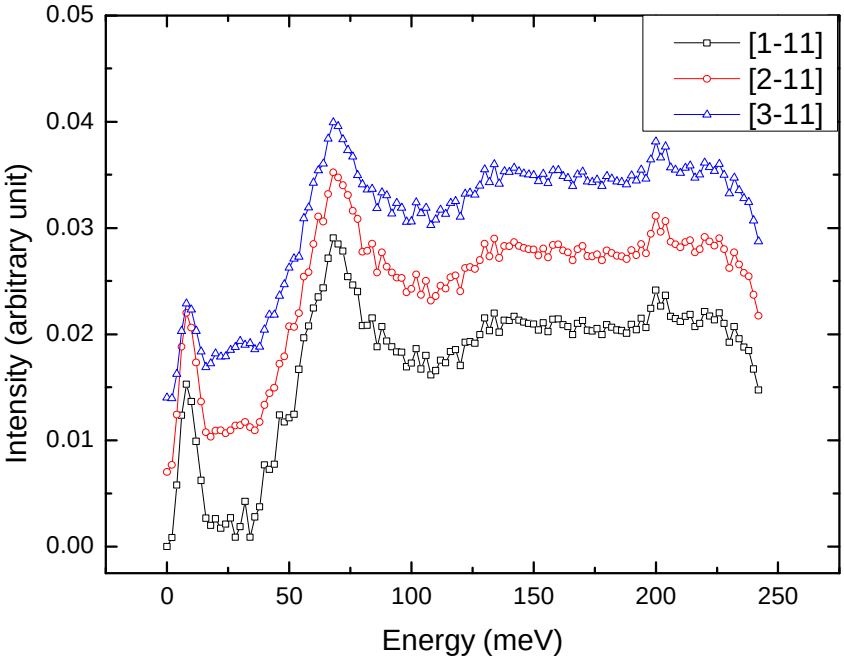
[1-11]
[2-11]
[3-11]
Intensity (arbitrary unit)
Energy (meV)
0.00
0.01
0.02
0.03
0.04
0.05
0
50
100
150
200
250

(b)

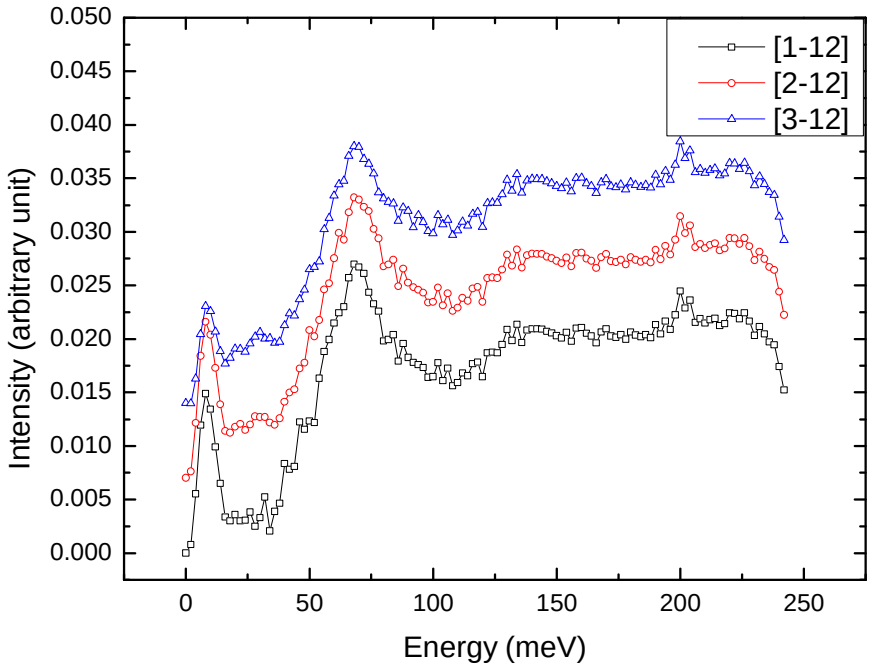
0.050
0.045
0.040
0.035
0.030
0.025
0.020
0.015
0.010
0.005
0.000
Intensity (arbitrary unit)
0
50
100
150
200
250
Energy (meV)
[1-12]
[2-12]
[3-12]

(c)

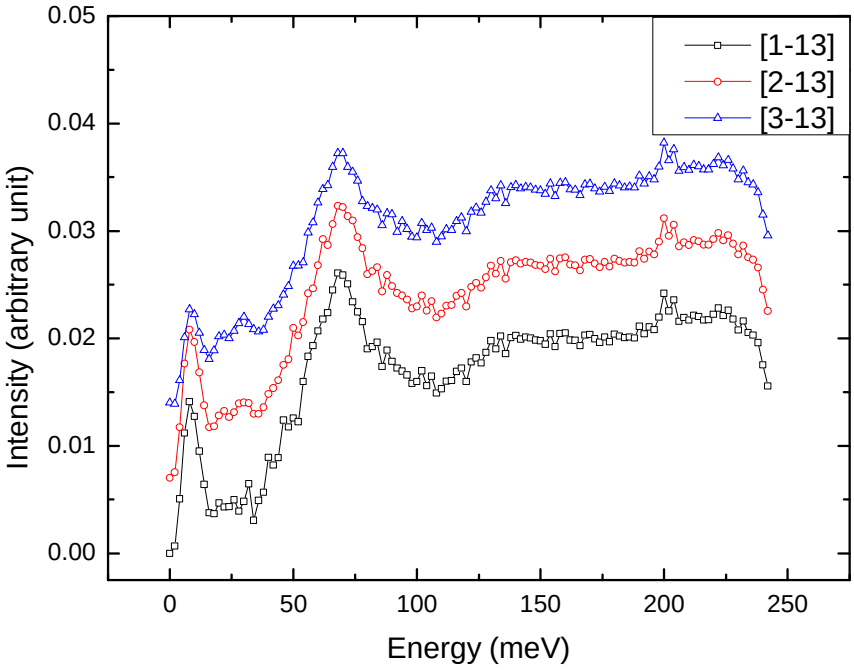
0.05
0.04
0.03
0.02
0.01
0.00
Intensity (arbitrary unit)
0
50
100
150
200
250
Energy (meV)
[1-13]
[2-13]
[3-13]

(d)

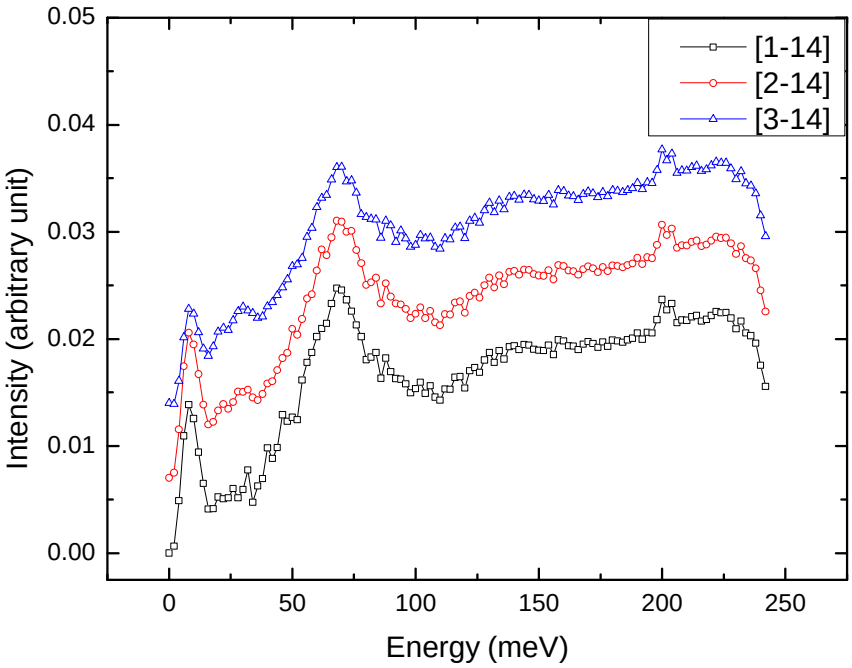

(e)

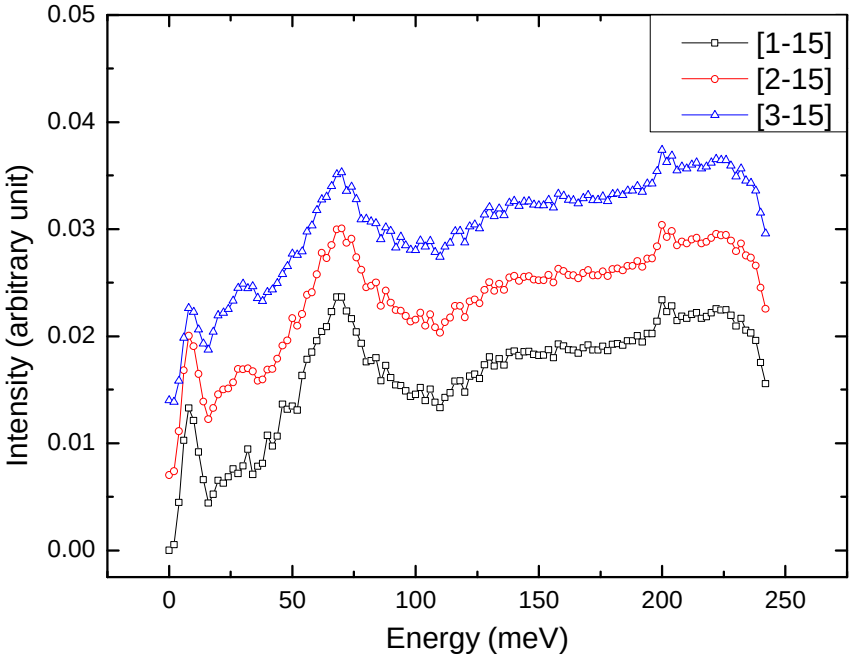

(f)

Figure C.8 (a)-(f): Comparison of IINS 300K Net data with various Q range.